ADVANCED ENERGY MATERIALS
www.advenergymat.de

Controllable Cathode–Electrolyte Interface of $Li[Ni_{0.8}Co_{0.1}Mn_{0.1}]O_2$ for Lithium Ion Batteries: A Review

*Hirbod Maleki Kheimeh Sari and Xifei Li**

As a high-capacity layered cathode material, $Li[Ni_{0.8}Co_{0.1}Mn_{0.1}]O_2$ (NCM811) has been one of the most felicitous candidates for utilization in the next generation of high-energy lithium ion batteries (LIBs). Notwithstanding its superiority, there are some issues concerning its cyclability, rate capability, and thermal stability that need to be settled prior to its further practical application. It is believed that upon cycling, chemical, mechanical, and electrochemical stability of the cathode–electrolyte interface plays a key role in resolving these issues. Therefore, all the extensive efforts directed so far toward the optimization of NCM811 electrochemical performance are by some means in connection with the cathode–electrolyte interface. Herein, unique structural and electrochemical characteristics of NCM811 together with in-depth understanding of its underlying bulk/surface degradation mechanism through cycling are reviewed. More importantly, for the first time, all compatible approaches thus far adopted to perfect the performance of NCM811 are exclusively and scrupulously addressed. Lastly, the most reasonable resolutions to accomplish a robust cathode–electrolyte interface, and consequently impeccable NCM811, along with proposed future research directions are presented.

1. Introduction

So far, lithium ion batteries (LIBs) are the most iconic, promising, and life-changing energy storage media due to the higher volumetric/gravimetric density, longer productive life-cycle, lower self-discharge rate, and maintenance cost as well as more environmentally benignity compared to their other commercial counterparts.[1–3] Owing to their indisputable impact on our daily life, e.g., from portable electronic devices (directly) such as smart phones to the air we breathe (indirectly), their development has become the number one priority in the field of energy storage. Despite the significant developments of anode materials (e.g., high capacity Si/graphite composite),[4–7] cathode materials as one of the principal components of LIBs (along with electrolyte and anode material) still face many challenges. As a result, the performance of LIBs strongly depends on the cathode materials.

Generally, three groups of cathode materials regarding their structures, i.e., spinel, olivine, and layered, have been used in LIBs, such as conventional $LiMn_2O_4$ (≈120 mAh g^{-1}), $LiFePO_4$ (≈160 mAh g^{-1}), and $LiCoO_2$ (≈140 mAh g^{-1}) positive electrodes with limited capacities, respectively.[8–16] Recently, new generation of the layered cathode materials, such as $Li[Ni_xCo_yAl_z]O_2$ (NCA) and $Li[Ni_xCo_yMn_z]O_2$ (NCM), has been broadly developed and commercialized primarily regarding their higher energy density and rate capability.[17,18] For example, leading companies such as Tesla and Boeing have employed LIBs with nickel-rich $Li[Ni_{0.8}Co_{0.15}Al_{0.05}]O_2$ as well as $Li[Ni_{1/3}Co_{1/3}Mn_{1/3}]O_2$ cathodes in their products.[19–21] Although the energy density of Ni-rich NCA is much higher than its conventional or lower Ni-containing counterparts, its discharge capacity should be restricted to 50–80% of its nominal value by controlling the depth of discharge to insure the structural and thermal stability of the electrode.[22,23] Meanwhile, fast-growing electric vehicles (EVs) and energy industries require LIBs with higher practical power/energy densities.

The average specific cell energy target for EV application is around 300 Wh kg^{-1} for 2025.[24] However, the actual value of energy density in electrode level is always smaller than the theoretical one in cell level owing to the presence of inactive materials inside the cell (i.e., collector, binder, electrolyte, conductive additives, separator and packaging materials) as well as inability in fully utilization of active materials. Hence, at the cathode active material level, a target value of almost 750 Wh kg^{-1} (≈202 mAh g^{-1} at the cutoff voltage of 3.7 V) is necessitated.[24,25] This target is possible to achieve with adjustment in some key parameters, such as Ni concentration in the cathode active material (0.33–0.90 mol%), anode material (graphite vs Si–C anode with a capacity of 1000 mAh g^{-1}), cell upper cutoff voltage (4.2 V vs 4.4 V), and electrode density (15 mg cm^{-2}, 35% porosity, vs 25 mg cm^{-2}, 20% porosity). Considering these parameters along with other modification

Dr. H. Maleki Kheimeh Sari, Prof. X. Li
Institute of Advanced Electrochemical Energy & School of Materials Science and Engineering
Xi'an University of Technology
Xi'an 710048, Shaanxi, China
E-mail: xfli2011@hotmail.com
Dr. H. Maleki Kheimeh Sari, Prof. X. Li
Shaanxi International Joint Research Center of Surface Technology for Energy Storage Materials
Xi'an 710048, Shaanxi, China
The ORCID identification number(s) for the author(s) of this article can be found under https://doi.org/10.1002/aenm.201901597.

DOI: 10.1002/aenm.201901597

methods, Ni-rich NCMs and particularly NCM811 (theoretical capacity of 278 mAh g^{-1}) is capable to reach or approach the energy density and specific energy of 700 Wh L^{-1} and 300 Wh kg^{-1}, respectively, at the cell level.[20,24,26]

Compared to NCA (80% Ni), NCM811 possesses the advantages of lower capital and production cost (simple co-precipitation method without extra heat treatment process), higher energy density and better thermal stability (**Figure 1**a),[24,27] which makes it the most potential candidate for new-generation of commercialized LIBs.[28] Nevertheless, several concerns, such as unsatisfactory cyclability, rate capability and thermal stability, have to be resolved to make it a feasible and practical choice for commercialization.[27]

To date, many researchers have investigated the origins of these pitfalls in NCM811. In summary, structural defects such as cation disordering as well as oxygen and lithium vacancies (schematically shown in Figure 1b–g) and further phase transformation and surface reconstruction, narrow electrochemical stability window of the electrolyte solvents, high reactivity of Ni^{4+} and oxidation/decomposition of the electrolyte accompanying oxygen and gas evolution which trigger safety hazard, interfacial side reactions and transition metal (TM) dissolution, anisotropic volume changes and microcrack generation through cycling, and moisture/air-reactive lithium residues on the surface are responsible for these shortcomings.[26,29–47] Notably, all of these issues either are initiated at cathode–electrolyte interface or somehow compromise the stability of this region which further deteriorate the electrochemical performance of the cell. Therefore, designing a stable and robust cathode–electrolyte interface is a determining factor which regulates the overall efficiency of the cell.

As one of the most propitious Ni-rich cathode materials, NCM811 possesses unique structure, chemistry and electrochemical characteristics. Up to the present, several review articles have addressed the recent progress of Ni-rich layered cathode materials in general, which mostly contain general information about a wide range of materials.[19,20,24,25,37,48–53] However, herein we exclusively and comprehensively focus on NCM811 and establish an understanding of its chemistry and structural properties along with its bulk structure and surface degradation mechanisms through cycling. Furthermore, we thoroughly explore the most reliable strategies studied thus far, i.e., surface-, structural-, and electrolyte modifications, for obtaining the most stable interface and consequently maximizing the long-term electrochemical efficiency. Finally, by summarizing challenges and outlining the proposed solutions we provide new insights toward designing an excellent cathode–electrolyte interface of NCM811 as a potential cathode material for the next-generation LIBs.

2. Chemical/Structural Properties and Instability

A deep understanding of chemistry and structure of NCM811 as a promising representative of Ni-rich cathode materials is a premise to realize the formation and evolution of cathode–electrolyte interphase layer. Additionally, it provides new insights about the origin of degradation which is of pivotal importance in order to design better electrode materials with less defects.

Hirbod Maleki Kheimeh Sari is currently a Ph.D. candidate in the Institute of Advanced Electrochemical Energy at Xi'an University of Technology. He received his Master's degree from the College of Mechanical Engineering, Malaysia University of Technology in 2014. His research interests primarily focus on the design and synthesis of novel nanomaterials for energy storage, especially cathode materials for lithium/sodium ion batteries.

Xifei Li is currently a full professor at Xi'an University of Technology. Prof. Li's research group is currently working on interface design of the anodes and the cathodes with various structures for high-performance energy storage devices.

Although high Ni content in NCM811 results in a high specific capacity, it induces some deficiencies, such as interfacial side reaction, anisotropic volume change, surface reconstruction and low thermal stability. Thus, the surface/interfacial structure and chemistry contribute substantially to the electrochemical properties of this cathode material.[54–57]

2.1. Bulk Structural Degradation

2.1.1. TM Oxidation States and Cation Mixing

It is believed that the redox reactions and consequent reversible capacity of NCM811 are primarily due to the electronic structure of active elements in the TM layers.[58–60] Indeed, chemical bonding between TMs and oxygen, which depends on TMs oxidation state, is a significant factor in determining the electrochemical activity and stability of cathode materials, thereby signifying the role of oxidation state of TMs in characterizing the cathode material. Oxidation state of Ni ions is an essential criterion for the electrochemical activity, stability and overall physicochemical properties of NCM cathode materials. According to the local magnetic moments and projected density of states (PDOS), Ni appears in three different oxidation states in NCM811 (i.e., Ni^{2+}, Ni^{3+}, and Ni^{4+}). Ni^{2+}/Ni^{3+} and Ni^{3+}/Ni^{4+} redox couples are primarily responsible for the material capacity. Ni^{2+} is favorable because of its ionic Ni–O synergy and

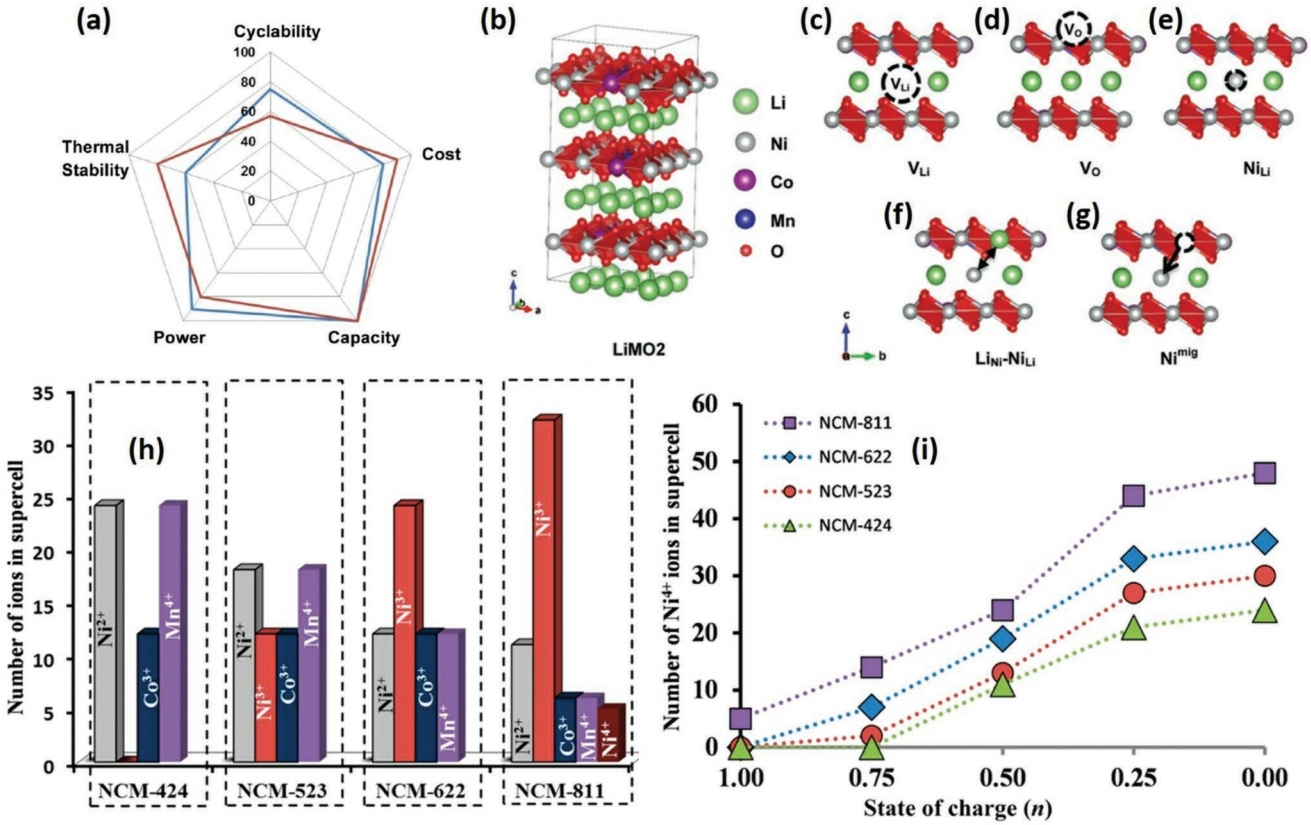

Figure 1. a) Comparison between the performance of NCM811 (red line) and 80% Ni-containing NCA (blue line). Reproduced with permission.[24] Copyright 2016, American Chemical Society. b) Atomic configuration for the layered NCM cathode material, and the schematic illustration of structural defects, such as c) Li vacancy (V_{Li}), d) Oxygen vacancy (V_O), e) Excess Ni (Ni_{Li}), f) Li/Ni exchange (Li_{Ni}–Ni_{Li}), and g) Ni migration (Ni^{mig}). Reproduced with permission.[47] Copyright 2017, Royal Society of Chemistry. h) A comparison between TM oxidation states and i) Number of Ni^{4+} ions as a function of SOC in different NCM cathode materials ($Li_n[Ni_xCo_yMn_z]O_2$). Reproduced with permission.[61] Copyright 2017, American Chemical Society.

two redox-active electrons. On the other hand, Ni^{4+} raises some issues, such as increasing Ni–O covalency, and reducing to Ni^{2+} through side reactions with electrolyte compounds because of its low-lying LUMO (lowest unoccupied molecular orbital). Ni^{3+} oxide can indeed readily lose oxygen due to its lower bond energy.[61] Nonetheless, both trivalent and tetravalent Ni are beneficial for amelioration of electrical conductivity.

A comparison between different NCM materials in terms of TMs oxidation states shows that the concentration of Ni^{3+} and Ni^{2+} ions increases and decreases, respectively, from NCM424 to NCM811 (Figure 1h). It is noticeable that the increase in number of Ni^{4+} ions as a function of state of charge (SOC) is more intense in NCM811 (Figure 1i).[61] Manganese appears in form of Mg^{4+}, which is an inactive Jahn-Teller ion, in the layered structure of NCM811. It does not change its oxidation state during cycling and does not engage in electrochemical reactions, thereby playing an important role in stabilizing the cathode structure. Co oxidation state is also constant in different NCMs, but according to Sun et al.[35] who analyzed TM oxidation states based on TM–O bond distance, there are two different oxidation states for Co (2+ and 3+). Nonetheless, many experimental studies refute the latter estimation and confirm the presence of only Co^{3+} in different NCMs.[27,61–67] It is presumed that the utilization of magnetic moments and PDOS approach is more reliable, because the presence of different type of TM–O bonds in NCMs would make the reflection of exact oxidation states based on bond distances less accurate. Nevertheless, it is confirmed by all researchers that the only oxidation state for Co in NCM811 is Co^{3+}.

Dixit et al.[61] applied density functional theory (DFT) to analyze the electronic structure, chemical bonding, structural details and oxidation states of TMs in NCM811 at different delithiation states. Thorough investigation of the electronic structure reveals an increase in the Ni-character of the oxygen-2p bands, along with Ni–O covalency, with Li deintercalation (cyan box in **Figure 2**a–d). Subsequently, more covalent M–O results in instability and more oxygen loss.[68] Indeed, as delithiation continues from $n = 1$ to $n = 0.25$ (in $Li_n[Ni_{0.8}Co_{0.1}Mn_{0.1}]O_2$), Ni^{3+}-e_g and Ni^{2+}-e_g bands lower than the Fermi states level diminish, and ultimately disappear at $n = 0.0$. Hence, the contribution of unoccupied Ni states escalates as the Li content decreases, confirming the Ni oxidation during Li deintercalation (Figure 2a–d). According to the chemical bonding descriptors (Figure 2e), COHP and ICOHP (integrated crystal orbital Hamilton populations), MO (molecular orbital) diagram (Figure 2f), and average Bader charges on oxygen atoms (Figure 2g) Ni–O covalency becomes more pronounced as the nickel oxidation state changes from Ni^{2+}–O to Ni^{4+}–O and

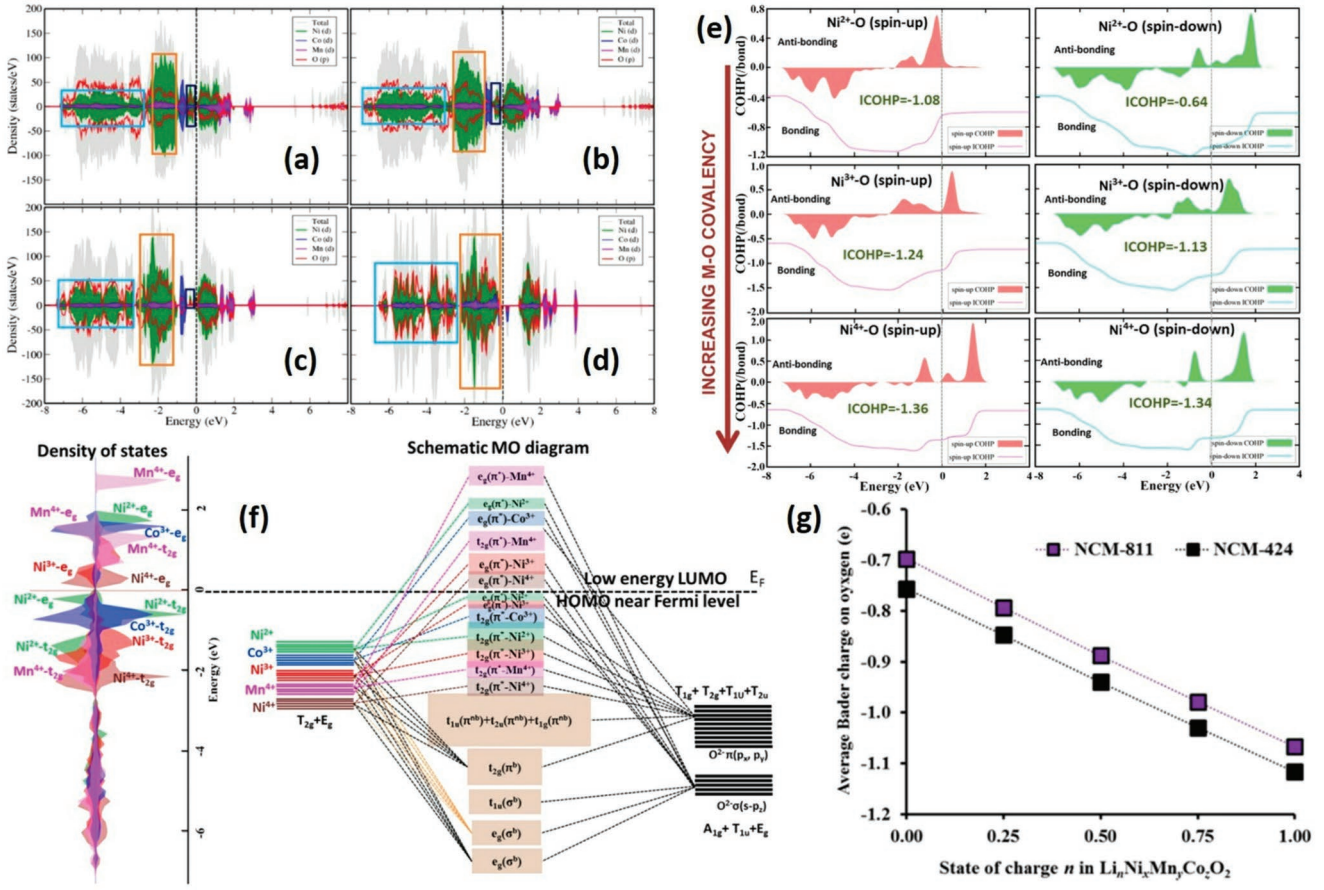

Figure 2. Density of states for $Li_n[Ni_{0.8}Co_{0.1}Mn_{0.1}]O_2$ when n is equal to a) 0.75, b) 0.50, c) 0.25, and d) 0.00. Orange, dark blue, and cyan boxes display the Ni-t_{2g} band, Ni-e_g band, and TM character in hybridized TM—O bonding states, respectively; dashed line represents the Fermi level. e) Chemical bonding descriptors, COHP and integrated COHP (ICOHP) for the pristine $Li[Ni_{0.8}Co_{0.1}Mn_{0.1}]O_2$. f) MO diagram of $Li[Ni_{0.8}Co_{0.1}Mn_{0.1}]O_2$ according to PDOS and COHP. g) Average Bader charges on oxygen atoms in NCM811 and NCM424 as a function of SOC. Reproduced with permission.[61] Copyright 2017, American Chemical Society.

Li deintercalation proceeds.[61] High covalency results in delocalized electron across the M–O bonds and further leads to extraction of bonding electrons during electrochemical oxidation, thereby weakening or breaking the M–O bonds. It has been experimentally proved that Ni^{4+}–O bonds are unstable and tend to reduce to more stable form of Ni^{2+} with attendant release of oxygen in partially delithiated states to keep the overall charge in balance.[27,61,64,69–71] This instability is primarily due to the low-lying LUMO of Ni^{4+}-e_g and its covalent character which makes it to readily receipt electrons from oxygen or electrolyte compounds at the solid electrolyte interphase (SEI).

General structure of the layered NCM materials (**Figure 3**a),[20] and in particular NCM811 (Figure 3b,c),[61] is in form of R$\bar{3}$m in which octahedral 3a sites (TMs) and octahedral 3b sites (lithium) are completely separated in its perfect state. However, cation disordering between these two sites can compromise the structural stability of these cathode materials.[37,72,73] The ionic radius of Ni^{2+} (0.69 Å) is approximately similar to that of Li^+ (0.76 Å); thus, divalent nickel ions readily occupy Li slabs, leading to cation mixing (CM). This cation migration can occur during synthesis or cycling process and eventually results in poor thermal stability and rate capability. Because of the nonuniform cation mixing, phase transformation occurs from layered (R$\bar{3}$m space group) to disordered spinel (Fd$\bar{3}$m space group) and finally rock-salt (Fm$\bar{3}$m space group) structure (Figure 3d) which deteriorate lithium diffusivity due to the diminished gaps between the slabs and obstructive TMs in Li layers. The level of transformation primarily depends on the upper cutoff voltages; generally, voltages higher than 4 V versus Li^+/Li result in higher degree of cathode degradation.[55,73,74] In fact, cation mixing is a mechanism which prevents structural collapse by utilizing the pillar effect of TMs in highly delithiated states. However, the nickel ion is not stable during cycling and tends to change its valence state through repeated oxidation and reduction. Indeed, It has been reported that other than nickel, disputable amount of Mn and Co also migrate to the lithium slabs.[20,55,75,76] The activation energy barrier of manganese migration is higher than that of cobalt and nickel due to stability of Mn^{4+} at octahedral sites. Hence, Mn is considered as the element responsible for structural and thermal stability of NCM materials.[38,64,77]

Lin et al.[32] studied the structural and chemical evolution of the layered NCM811 at atomic scale in detail. They revealed the formation of consecutive structural transformation along with

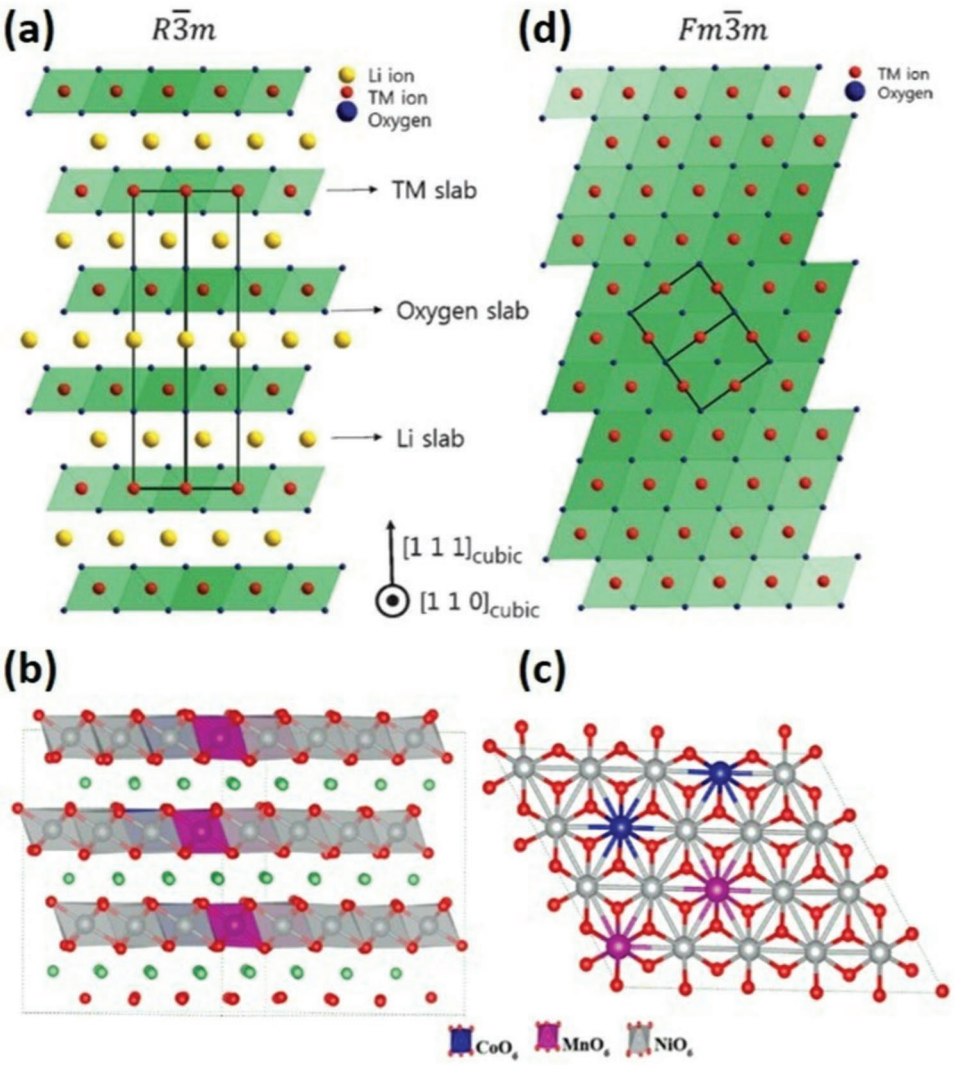

Figure 3. a) General structure ($R\bar{3}m$) of the layered NCM materials. Reproduced with permission.[20] Copyright 2015, Wiley. b) Layered structure of NCM811, in which green and red colors represent Li and oxygen atoms, respectively, and c) the most preferred cation configuration in NCM811. Reproduced with permission.[61] Copyright 2017, American Chemical Society. d) Cation-mixed phase with rock-salt structure ($Fm\bar{3}m$). Reproduced with permission.[20] Copyright 2015, Wiley.

nickel concentration gradient from bulk to the surface of the cathode particles over cycling. **Figure 4**a–c shows the atomic resolution STEM-HAADF images of continuous structural-changes from balk to the surface and their relevant structural pattern for NCM811 after 100 cycles, respectively. The structure transforms gradually from a well-layered in the balk to disordered layered, defect rock-salt, and eventually rock-salt phase near the surface in which the Li^+ diffusion paths have been entirely blocked by TM cations. Therefore, finding a method to avoid cation migration is of great significance for achieving an excellent electrochemical performance.[32] Figure 4d,e indicates that Ni concentration and quantitative Ni/(Co+Mn) atomic ratio progressively decline from balk toward the surface of the NCM811 particles through cycling, implying that nickel ions continuously move from the inner layers to the surface and presumably dissolve into electrolyte. Such progressive decline of nickel concentration together with irreversible nickel redox result in structural evolution.[32] Moreover, oxygen evolution can provoke cation mixing. According to the electron energy loss spectroscopy (EELS) results for cycled NCM811, the oxygen K-edge pre-peak intensity declines steadily toward the surface which is indicative of oxygen redox and subsequently oxygen loss. Such evolution results in oxygen vacancy as well as reduction of TM cations, and further induces TM ions to migrate into Li slabs by declining the diffusion barriers, thereby assisting the progress of cation mixing and facilitating the structural reconstruction.[32,78]

Cation mixing can also be triggered by heating temperature, which is connected to the oxygen evolution.[38] Bak et al.[38] studied the thermal stability of NCM cathode materials at their charged state via integrated TR-XRD and MS technique. As shown in **Figure 5**a, NCM811 encounters the first and

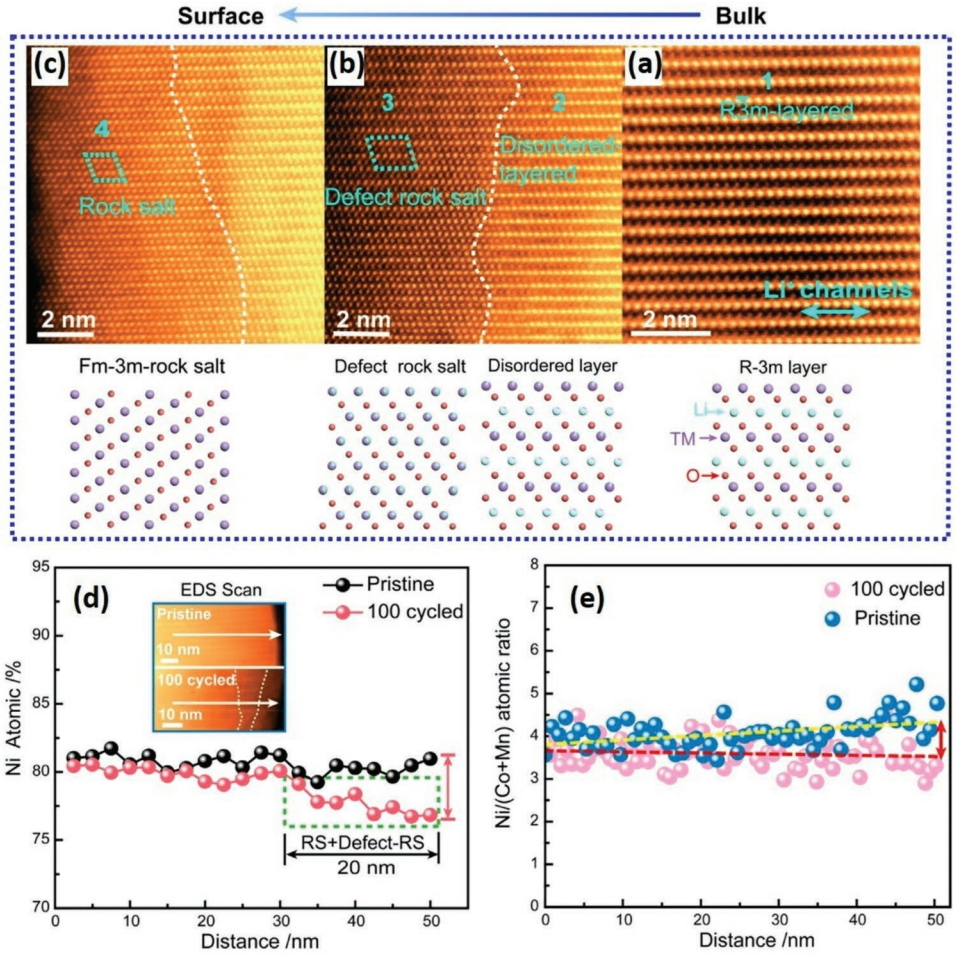

Figure 4. a–c) The atomic resolution STEM-HAADF images of continuous structural-changes from balk to the surface and their relevant structural pattern for NCM811 after 100th cycle at a cutoff voltage of 4.5 V; dashed lines with white color refer to the formation of surface reconstruction at different stages. d) Quantitative atomic ratio of nickel and e) quantitative atomic ratio of Ni/(Co+Mn) for pristine and 100 times cycled samples, scanned from the bulk to surface along Li-ion diffusion paths, as shown in the inset (d). Reproduced with permission.[32] Copyright 2018, Elsevier.

second phase transition from layered to S1 ($LiMn_2O_4$-type spinel) and further to S2 (M_3O_4-type spinel) at 135 and 155 °C, respectively, in the confined temperature range of almost 20 °C. Subsequently, the final phase transition from disordered spinel to rock-salt is completed at 365 °C. The primary difference between S1 and S2 is about lattice parameters and cation configuration in 8a tetrahedral sites.[64] Simultaneous MS (mass spectroscopy) profiles for the oxygen reveals that oxygen evolution peaks are tightly corresponded with the phase transitions in different temperatures. In case of NCM811, the peak of oxygen release starts at around 130 °C and reaches its highest level at ≈150 °C which is closely aligned with the first and second phase transition in Figure 5a.

The migration path of TM cations and phase transition in the course of thermal decomposition in NCM materials is schematically shown in Figure 5b. In initial state, TM cations and lithium ions occupy different layers of octahedral sites. During first transition, some of the Ni cations (denoted as "A") leave their original location and migrate to lithium octahedral sites (denoted as "B") through the most energetically favorable path, which is across the closest tetrahedral site.[77] This phase transition will be completed by the migration of Li^+ from its original location to adjacent tetrahedral sites, which results in oxygen evolution by reduction of Ni cations in highly delithiated states. In fact, when NCM811 is charged to 4.3 V, most of Ni cations will be oxidized to Ni^{4+} and again reduced to their more stable form of Ni^{2+} through heating, which is accompanied by oxygen loss. Therefore, the amount of Ni^{4+} cation in the structure at highly delithiated states plays an important role in thermal stability of NCM811 cathode material.[38]

2.1.2. Mechanical Integrity and Crack Generation (Lattice-Change)

It is believed that anisotropic change of lattice parameters in nickel-rich cathode materials, particularly NCM811, through cycling is the main reason for structural degradation and further capacity fading.[36,38,56,60,61,79–85] Ni-rich cathode materials upon charging and discharging suffer from mechanical stress and strain inside the particles and at the interfaces between the primary crystallites induced by anisotropic volume changes and continuous phase transitions which result in intergranular

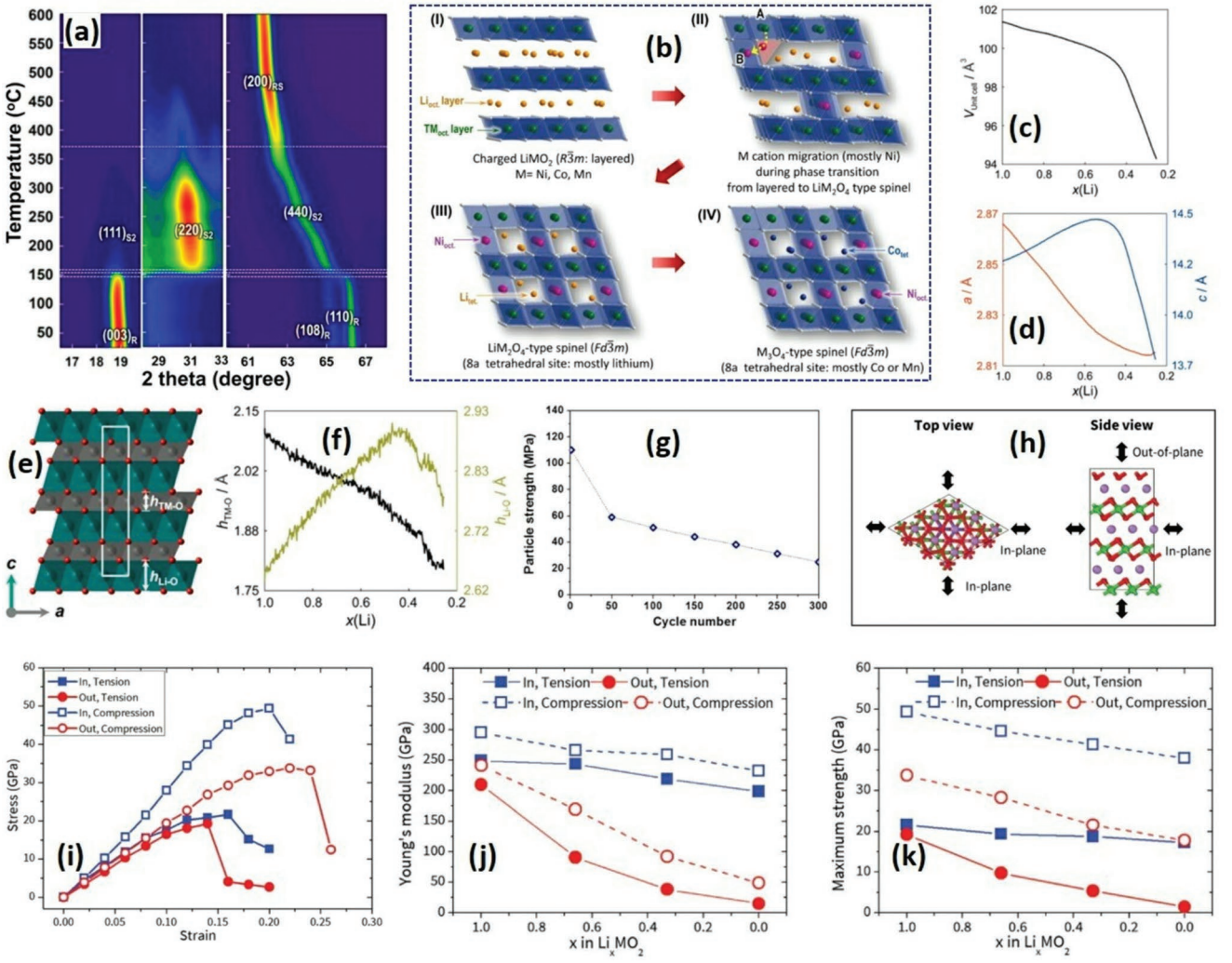

Figure 5. a) TR-XRD patterns in form of contour plots for NCM811. b) Schematic illustration of the migration paths of TM cations and phase transition in the course of thermal decomposition in layered NCM electrode materials. Reproduced with permission.[38] Copyright 2014, American Chemical Society. c) Volume change in the unit cell and d) change of lattice parameters *a* and *c*, as a function of Li content in NCM811. e) The structure of $Li[Ni_{0.8}Co_{0.1}Mn_{0.1}]O_2$ with specified TM–O layers in gray, Li interlayers in green and their corresponding slab heights (i.e., h_{TM-O} and h_{Li-O}, respectively); the white rectangle indicates the unit cell. f) h_{Li-O} and h_{TM-O} as a function of the Li content. Reproduced with permission.[60] Copyright 2017, American Chemical Society. g) Particle strength of the NCM811 full-cell as a function of cycle number. Reproduced with permission.[83] Copyright 2016, Elsevier. h) Out-of-plane and in-plane directions of applied compressive and tensile deformations. i) Stress–strain curves for $Li[Ni_{0.8}Co_{0.1}Mn_{0.1}]O_2$ under both compressive and tensile deformations for in-plane and out-of-plane directions. j) Young's modulus, and k) Maximum strength of $Li[Ni_{0.8}Co_{0.1}Mn_{0.1}]O_2$ as a function of lithium content under different deformation states; In and Out refer to in- and out-of-plane directions, respectively. Reproduced with permission.[31] Copyright 2018, Royal Society of Chemistry.

fracture, microcrack formation, disintegration of the particles, pulverization, and eventually loss of electrical contact and formation of reactive surfaces which accelerates undesired electrolyte side reaction along the grain boundaries.[36,83,86–88] According to Kondrakov et al.[36] even a slight anisotropic change of volume in $Li[Ni_{0.8}Co_{0.1}Mn_{0.1}]O_2$ structure leads to microcrack generation in secondary particles. Thus, analyzing changes in lattice and subsequently unit-cell volume as a function of lithiation/delithiation is helpful to understand the mechanical degradation mechanism in NCM811.

In situ X-ray diffraction (XRD) confirms that the lattice-changes of interlayers in NCM materials through lithiation/delithiation, particularly at high state of charge (SOC), are highly anisotropic and induce mechanical stress/strain at grain boundaries, initiating microcracks.[36,60,89] In NCM811, the interlayers spacing, where the Li ions are located, i.e., the area between the bottom and upper oxygen planes of adjacent TM–O layers, is affected by intense nonmonotonic variations at high cutoff voltages above 4 V versus Li^+/Li.[36,60,89] Kondrakov et al.[60] studied electronic structure of NCM811 and investigated its crystallographic changes, specifically in the TM–O and Li–O slabs, during different SOC via DFT together with Bader charge analysis, operando XRD as well as ex situ hard and soft X-ray absorption spectroscopy (hXAS and sXAS, respectively).

Figure 5c shows the volume change in the unit cell as a function of lithium content. The volume decreases in a nonlinear

manner as the charge cycle begins; slowly at first (until Li content reaches to almost 0.4), and faster as the lithium content further decreases. Variation of lattice parameters *a* and *c* which depends on interlayer spacing and slab heights, respectively, dictates the change in unit-cell volume. The formula of calculating the unit-cell volume (i.e., $V = a^2c \sin \pi/3$) indicates the significant contribution of *a* lattice in determining unit-cell volume, particularly at the beginning of charge cycle ($1 \geq \text{Li} \geq 0.4$) that *a* lattice decreases steeply.[60] During charging process in NCM811, lattice parameters react in different ways; *a* lattice reduces while *c* lattice increases first (until Li content reaches to almost 0.4) and then reduces (Figure 5d).

The *c* lattice depends on h_{Li-O} and h_{TM-O}, which are the height of Lithium–Oxygen slabs and Transition metal–Oxygen slabs, respectively, that alter along z direction as shown in Figure 5e. Slab heights change upon lithiation/delithiation; h_{TM-O} reduces as lithium content decreases, while h_{Li-O} increases at the beginning of charge cycle (until Li content reaches to almost 0.4) and then decreases until the end of charge (Figure 5f). The net effect of concurrent expansion and shrinkage of these two slabs on *c* lattice parameter is positive (when $\text{Li} \geq 0.4$), indicating more pronounced change in Lithium–Oxygen slabs. Subsequently, the significant shrinkage of *c* lattice occurs as delithiation further continues ($\text{Li} < 0.4$), when both h_{Li-O} and h_{TM-O} decrease, simultaneously.[60]

According to the XAS results, shrinkage of TM–O layer is primarily due to the oxidation of nickel to higher states. The values of *a* lattice and TM–O bond length (l_{TM-O}) are indeed related to the oxidation states of transition metals and consequently their ionic radii. The decline of these values in the course of delithiation is indicative of charge compensation by TMs oxidation. More severe changes reflect higher redox states and therefore higher capacity.[36] The sXAS results along with DFT-based Bader charge analysis indicate that charge transfer between O-2p and partially filled Ni-e_g orbitals is responsible for interlayer shrinkage and further decrease of Oxygen–Oxygen repulsion.[60] In fact, in layered NCM cathode materials the interlayer distance is controlled by TM–Oxygen slabs repulsion.[36,90] At the beginning of the charge cycle interslab repulsion reduces due to the screening effect of present lithium ions on the negative charge of oxygen. As delithiation continues the interslab repulsion increases, leading to the expansion of *c* lattice.

However, in NCM811 the *c* lattice encounters contraction from almost the middle to the end of charge process, implying a decline in interslab repulsion. This decline is due to the highly mixed TM–O band induced by hybridization of O-2p and TM-3d states,[91] which means that electrons can be extracted from either TM or oxygen state. Therefore, the shrinkage occurs in *c* lattice due to the decline in effective oxygen charge and concurrent decrease in interslab repulsion.[36] These two effects (i.e., decreasing screening effect of Li, and negative charge of oxygen atoms) do not entirely counterbalance each other. It is believed that in $Li_n[Ni_{0.8}Co_{0.1}Mn_{0.1}]O_2$, interlayer distance is determined by Li screening effect ($1 > n(\text{Li}) > 0.5$), and effective charge of the oxygen atoms ($n(\text{Li}) \leq 0.5$) during charge cycle.[36] Thus, it indicates that the combination of TM and oxygen states is not linearly connected to the Li content. As a case in point, oxygen states start to engage in charge compensation beyond Li content of 0.5 (not from the beginning of charge process) until the end of charge cycle where the TM–O bands begin to mix and be more covalent.[60,91,92]

Perpetual volume changes throughout the course of charge/discharge induce mechanical strain/stress which eventually lead to microcrack generation and further mechanical degradation and lower strength.[85] Particle strength in NCM811 full-cell as a function of cycle number is shown in Figure 5g.[83] Comparing young's modulus and other structural properties of NCM811 with lower Ni-containing NCM cathode materials reveals that the former is more prone to intergranular cracking due to its lower structural stability.[31,35] NCM811 structure undergoes two types of deformation, i.e., tensile and compression, in generally two different directions, namely in-plane and out-of-plane (Figure 5h).[31] The Young's modulus and maximum strength values investigated via DFT-based framework signify that the structure of NCM811 is more susceptible to tensile- than compressive deformation. Figure 5i is indicative of anisotropic mechanical properties of NCM811, since the structure is more resistant to compression and in-plane deformations rather than tension and out-of-plane deformations.[31] According to Figure 5j,k, which illustrate Young's modulus and maximum strength of NCM811 as a function of lithium content under all deformation modes, delithiation considerably weakens the structural stability, particularly in the out-of-plane direction.[31] Ni–O and Li–O bond strengths play an important role in mechanical stability of NCM811 for in-plane and out-of-plane directions under tension, respectively. It is noteworthy that the atomic charge in Ni and oxygen will be increased due to the charge compensation during delithiation, thereby weakening the Ni–O bond.[35] Additionally, evolving of gaseous oxygen at the end of charge process (Li content less than 0.5) can compromise the mechanical stability throughout the electrochemical cycling.[88,93,94]

Although Li–O bonds contribution to mechanical stability for in-plane direction is negligible due to the weaker bond strength compared to Ni–O, their significance in out-of-plane direction is undeniable. Li–O bond network determines the interaction between Ni and oxygen layers, thereby governing the stability of the structure in this direction. As a result, declining the number of Li–O bonds during delithiation can initiate layer delamination.[31] Under compressive deformation, short bond length of Li–O would cause structural degradation in both directions. Therefore, considering the fact that out-of-plane deformation provokes more structural instability for NCM811 during cycling, taking control of the Li–O bond network is of great importance. According to First-principle calculations based on DFT done by Min et al.,[31] the value of generated stress through charge/discharge in NCM811 is much smaller than the maximum strength under all deformation modes; thus the structural failure does not occur within initial cycles, rather after considerable number of cycles due to the fatigue behavior of under stressed particles.

The structure of layered NCM materials includes secondary particles made from agglomeration of primary particles oriented in different direction with many voids and grain boundaries in between. Upon cycling, mechanical stresses grow inside the secondary particles along the boundaries and form intergranular microcracks (**Figure 6**a,b).[49] Figure 6c–f[36]

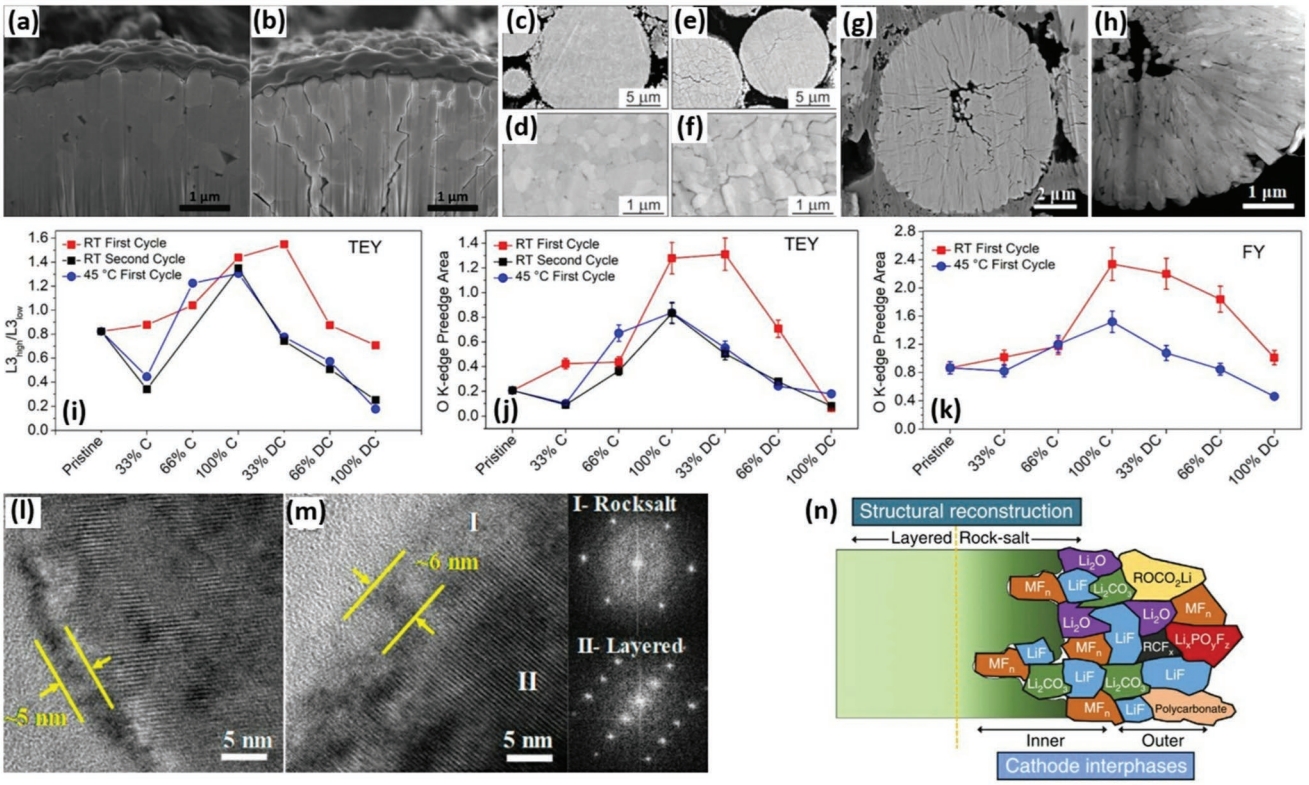

Figure 6. a) Cross-sectional SEM images of a pristine NCM811 cathode before cycling and b) after 100 times cycling at C/3 and 45 °C. Reproduced with permission.[49] Copyright 2017, The Electrochemical Society. Cross-sectional SEM images at different magnifications for NCM811 c, d) before cycling and e,f) after 50th cycle at C/2. Reproduced with permission.[36] Copyright 2017, American Chemical Society. Cross-sectional g) SEM and h) Dark-field scanning TEM image of NCM811 at fully charged state in first cycle, and in discharged state after 100th cycle, respectively. Reproduced with permission.[26] Copyright 2018, American Chemical Society. sXAS quantification at varying SOC where (i) portrays the TEY of Ni displaying the L_3 peak ratio, (j) portrays the TEY and (k) portrays FY data of the oxygen K-edge with hybridized area of the pre-edge TM-3d–O-2p. Reproduced with permission.[30] Copyright 2018, American Chemical Society. HR-TEM image of the discharged cathode after 100th cycle for l) NCM622 and m) NCM811. Reproduced with permission.[26] Copyright 2018, American Chemical Society. n) Schematic view of the intricate cathode–electrolyte interfacial, structural, and chemical reconstruction upon cycling. Reproduced with permission.[102] Copyright 2017, Springer Nature Limited.

shows cross-sectional SEM images of NCM811 before cycling and after 50 cycles. Microcracks with zigzag pattern which get narrower near the surface of the particle are noticeable in the cycled cathode. Thus, it can be deduced that intergranular cracks initiate from the center of particle, probably because of tensile deformations. Over the course of delithiation outer regions expand more and faster than inner regions because only the surface of NCM particles is in contact with electrolyte and other additives directly. Figure 6g,h shows the cross-sectional SEM and TEM images of $Li[Ni_{0.8}Co_{0.1}Mn_{0.1}]O_2$ at 4.3 V after the first charge cycle and 100th cycle, respectively.[26] The former includes some microcracks initiated from the pores in the center of the particle which most of them are stopped before reaching to the surface. Notably, there is no truce of these microcracks after 100 cycles. It appears that the generated gaps between primary particles in charge cycles were closed in subsequent discharge cycles and internal stress/strain was not big enough to damage secondary particles permanently.[26,32]

According to the research done by Yan et al.[56] on NCM111, the generation of microcracks might sometimes be instigated from the inside of the primary particle grains instead of grain boundaries. These intragranular cracks can be more pronounced at high voltages such as 4.7 V and expose new surfaces inside the primary particles to the electrolyte, thereby deteriorating the mechanical degradation and consequently battery performance. It is possible that this mechanism of crack generation happens in NCM811 as well; thus, high-voltage operation should preferably be avoided. One method to control the evolution of internal stress/strain and impede the microcrack generation in NCM811 is radial crystallography, in which primary particles are oriented radially, so that expansion and contraction occurs in a uniform way, thereby minimizing anisotropic volume changes and enhancing cycle performance.[95]

Indeed, increasing wettability of the cathode surface, which means the reduction of electrolyte contact angle, leads to a well-distributed mechanical stress/strain due to increase of the cathode–electrolyte contact area, thereby alleviating the volume change to some extent.[96] Establishing a method to boost the interaction between oxygen and transition metal layers could be another solution. For instance, introducing pillar layers or utilizing doping elements in lithium slabs to increase bridging effect and slow down the phase transition.[26] Alternatively, developing a filling glue layer inside the voids at the interface to extend the primary particles interaction has been suggested

as a potential solution.[97] Indeed, restriction of DOD can effectively stop the crack generation at the cost of energy density which is not favorable in case of commercialization.

2.2. Surface Reconstruction and Interfacial Side Reactions

Understanding the surface structure and chemistry of cathode materials along with their side reactions with electrolyte is a crucial step for designing an excellent cathode–electrolyte interface and further improving the electrochemical performance by keeping them under control. However, characterization of this interface is extremely challenging due to its volatile nature and spontaneous formation together with the paucity of decisive in situ characterization techniques.[98,99] A variety of degradations resulting in power fading, capacity fading, high impedance, low coulombic efficiency, gas evolution, etc. are in tight relationship with side reactions occurring at the interface of cathode–electrolyte between electrode surface active particles and electrolyte compounds.[100] Therefore, studying thermodynamic features and kinetics of this interfacial side reactions is of prime importance. Pristine NCM811 surface structure includes Ni cations with high oxidation states which result in formation of hole states in TM–O octahedral units and further trigger the surface structural evolution and subsequent oxygen loss, particularly at high delithiated states. In fact, because of O-2p and TM-3d orbitals hybridization in NCM811, hole states to some extent locate in O-2p orbitals which triggers oxygen loss and reaction of transition metals during cycling or storage.[101]

Steiner et al.[30] comprehensively studied the chemistry of cathode–electrolyte interface and surface reconstruction in NCM811 in different temperatures, cycle numbers and SOCs. The results show that TM dissolution and surface reconstruction occur at the initial stage of cycling and get worse at elevated temperatures and also as cycling continues. To obtain a better perception of surface reconstruction, sXAS was used to analyze the electronic structure of each element in NCM811. Total electron yield (TEY) and fluorescence yield (FY) detection mode was employed at various SOCs to probe the surface and bulk of the electrode, respectively. The ratio of higher- to lower energy peak intensity in Ni L_3-edge through the first and second cycles, in which XAS signal is less contaminated by side compounds produced from interaction with electrolyte, is representative of Ni oxidation state.[30]

As shown in Figure 6i, in first cycle at room temperature Ni oxidizes during charge and even 33% of discharge cycle and then reduces until the end of cycle.[30] However, in second cycle as well as first cycle at elevated temperature (45 °C) Ni initially reduces until 33% of charge cycle then oxidizes for charge compensation. Subsequently, with beginning of the discharge process reduction occurs to a great extent, resulting in phase transition to spinel/rock-salt defined as surface reconstruction. The results indicate that surface degradation intensifies by both temperature elevation and cycling prolongation. Oxygen K-edge pre-edge graph (Figure 6j) also demonstrates the same behavior. Hybridization of O-2p and TM-3d orbitals together with high state of Ni oxidation expedite the electrolyte oxidation and subsequently result in Ni reduction to compensate the oxygen loss from the surface of the cathode particles. FY diagram of Oxygen K-edge shown in Figure 6k indicates that at higher temperatures oxygen loss happens in deeper layers. Results also reveal that cobalt oxidation state remains unchanged and its dissolution in electrolyte accelerates at elevated temperatures. Indeed, STEM-EELS analysis confirms the existence of rock-salt structure after the first cycle and also suggests that the depth of surface reconstruction is more than anticipated.[30]

The amount of gas evolution on the surface of NCM811 over cycling reflects the stability of cathode–electrolyte interface, in which more pressure is indicative of less stability. Kim et al.[83] measured the internal pressure of charged NCM811 full-cell after long-term cycling at the high temperature of 95 °C (for 12 h). The results show lower internal pressure after first cycle and higher pressure with no evident difference after 100 and 300 cycles, suggesting that interfacial stability between cathode and electrolyte gets worse through cycling, with higher rate at initial stages and lower rate over long-term cycling. The surface of NCM811 is prone to degradation by formation of a thin layer of NiO-like rock-salt structure in pre-cycling stage during storage in air or inert atmosphere, which is related to residual active lithium and other contaminating species as well as oxygen loss.[55]

Surface reconstruction can also be initiated during cycling at initial stages when cation mixing occurs at highly delithiated states, resulting in structural evolution from layered to NiO-like rock-salt phase.[55,64,102] Parasitic reaction with electrolyte also arises with the presence of highly reactive Ni^{4+} on the newly formed layer, particularly at high potentials (above 4.2 V).[84] Reduction of tetravalent nickel in delithiated states and subsequent oxygen release undermine the crystal structure and oxidize the electrolyte, forming a cathode solid electrolyte interphase (CEI) followed with gas evolution.[103] CEI formation in most cases leads to reduction of capacity retention and coulombic efficiency due to the electrolyte consumption.[64,104,105] In effect, formation of these insulating, unstable and nonconductive layers at the cathode–electrolyte interface impede Li^+ diffusion into the layered cathode structure, resulting in impedance build-up and capacity fading. Figure 6l,m[26] shows the high-resolution TEM images of NCM622 and NCM811 after 100 cycles, in which the thickness of the damaged surface is almost 5 and 6 nm, respectively, suggesting that there is no considerable difference in surface evolution between these two cathode materials.

In synthesizing process of NCM811 excessive amount of lithium will be used to assure the formation of highly crystalline and well-ordered layered structure. Hence, unreacted lithium residues, supposedly in form of Li_2O and Li_2O_2, can be remained on the surface of the cathode material and react with CO_2 and H_2O in ambient condition to form Li_2CO_3 and LiOH which causes irreversible capacity and growth of charge transfer resistance due to lithium-ion diffusion suppression.[73,103] Indeed, powder NCM811 in water has commonly the pH value of 12 and above, which quickly forms a composite gel in NMP solvent.[106,107]

The exact composition of degradation compounds firmly depends on the electrolyte composition; they primarily form on the secondary particles surface. However, generation of microcrack through cycling may cause the penetration of electrolyte inside the primary grain boundaries and rise the interfacial

impedance over cycling.[20] The interfacial layer mostly corresponds to the deposition of decomposed electrolyte products and dissolution of transition metal ions on the cathode surface provoked by acidic compounds attack, such as HF which is a product of lithium-salt decomposition in presence of H_2O.[3,64] A schematic view of the intricate cathode–electrolyte interfacial, structural and chemical reconstruction upon cycling is depicted in Figure 6n.[102] Moreover, It has been shown that dissolution compounds from cathode surface, such as NiF_3, MnF_3, MnF_2, CoF_3 and LiF_2 migrate through electrolyte and deposit on the anode surface upon cycling.[53,108]

However, Kim et al.[83] examined nickel dissolution in NCM811 upon cycling using inductively coupled plasma-mass spectrometry (ICP-MS) analysis and concluded that nickel content in the cathode electrode remains almost constant after cycling 300 times, despite the considerable capacity fading, indicating that dissolution of nickel has minor impact on the cathode degradation. Nonetheless, ICP-MS analysis only yielded the ratio of transition metal elements, not their contents, which is not an accurate gauge for confirming the consistency of Ni amount through cycling. In addition, Jung et al. by performing On-Line Electrochemical Mass Spectrometry (OEMS) analysis on layered oxide cathode materials, including NCM811, concluded that transition metals in NCM cathode materials do not have catalytic effect on electrolyte oxidation.[109] Overall, reconstruction mechanism of the cathode surface is very complicated and employment of more sophisticated in situ techniques is necessary for studying and unraveling it with more accuracy.

3. Performance Enhancement Strategies

Designing a stable, robust and chemically favorable cathode–electrolyte interface is the primary solution to the poor cycle-life and capacity retention of Ni-rich layered cathode materials such as NCM811. To reach this goal and further improve the electrochemical performance of the LIBs before deployment in commercial scale, several strategies have been suggested and applied which include surface-, structural-, and electrolyte modification.

3.1. Surface Modification

3.1.1. Coating

The interphase layer between the surface of NCM811 and electrolyte plays an important role in controlling the degree of lithium-ion diffusion, charge transfer and parasitic reactions. Engineering the properties of this layer through nanoscale coating is a highly efficient strategy to boost the electrochemical performance of the LIBs in terms of rate capability, thermal stability and capacity retention. The function of coating layer is to serve as a protective barrier at the cathode–electrolyte interface, enhance structural stability and regulate the interface chemistry to prevent TMs' dissolution and other side reactions, promote Li^+ diffusion, and further avoid cathode degradation and electrolyte decomposition.[110,111]

Electrochemically Inactive Coating: Coating electrochemically inactive compounds such as, metal oxides, -fluorides, and -phosphates, in which the metal possesses only one stable oxidation state, have been considered as an effective strategy to improve cyclability and overall electrochemical performance of the nickel-rich layered cathode materials, particularly NCM811. These coating layers primarily act as a physical barrier between cathode surface and electrolyte to prevent active material degradation and electrolyte decomposition. Indeed, controlling the uniformity, structure, and thickness of the formed interphase layer are of great significance so as to promote lithium-ion diffusivity and reduce impedance. In this regard, a uniform and smooth nanoscale coating layer has been proved to be more effective.[24] Amphoteric metal oxides like Al_2O_3 are able to react with HF in electrolyte and transform to HF resistant metal fluorides (e.g., AlF_3) and water, thereby reducing electrolyte acidity and slowing down its degradation.[112] However, the generated water facilitates the formation of HF in electrolyte and these series of reactions will be repeated, thereby thickening the coating layer and regressing the performance. On the other hand, if the cathode material is covered with the stable metal fluorides in the first place, the HF level in electrolyte remains constant through cycling.[24,113]

Woo et al.[114] coated AlF_3 on NCM811 which resulted in enhanced rate capability, cyclability, thermal and structural stability. Although the coating layer was nonuniform and mostly amorphous (as shown in **Figure 7**a), the capacity retention of the coated sample improved from 84% to almost 93% after 60 cycles. However, no conspicuous improvement in initial capacity was observed (196 mAh g^{-1} for coated sample vs 193 mAh g^{-1} for the pristine sample at 0.5 C rate). Nyquist plots confirmed that AlF_3 coating has no effect on surface film resistance (R_{sf}). Nonetheless, the charge-transfer resistance (R_{ct}) showed considerable decline in coated sample. Restricting the direct contact between the electrolyte and cathode surface resulted in an enhanced thermal stability of the coated NCM accompanying with surpassing oxygen release from the layered structure, gas evolution and Ni^{4+} reaction with the electrolyte solution. Moreover, a comparison between AlF_3 and Al_2O_3 coated NCM indicated that the former is more resistive to HF attack in long-term cycling. Dong et al.[115] by conducting coating process on the surface of $Ni_{0.8}Co_{0.1}Mn_{0.1}(OH)_2$ in presence of CO_2 flow synthesized an Al_2O_3-coated NCM811 with excellent capacity retention and rate capability even at high cutoff voltage of 4.5 V. Despite its slightly lower initial capacity compared to the pristine material, the 1 wt% Al_2O_3-coated sample maintained 99% of its capacity after 60 cycles at 1 C within the both voltage ranges of 2.8–4.3 and 2.8–4.5 V. Although the coating layer is electrochemically inactive, it shows a better lithium-ion diffusivity compared to the pristine cathode (Figure 7b), suggesting that an optimal amount of alumina coating can build an effective cathode–electrolyte interface and promote the transmission of lithium ion.

The impact of nickel-rich NCM composition on behavior and effectiveness of Al_2O_3 coating have been studied by Han's group.[116] Experimental analyses and computational methods, such as nuclear magnetic resonance, high resolution X-ray diffraction, and DFT calculations reveal that more Mn content in the layered NCM structure (e.g., NCM532) can hinder the

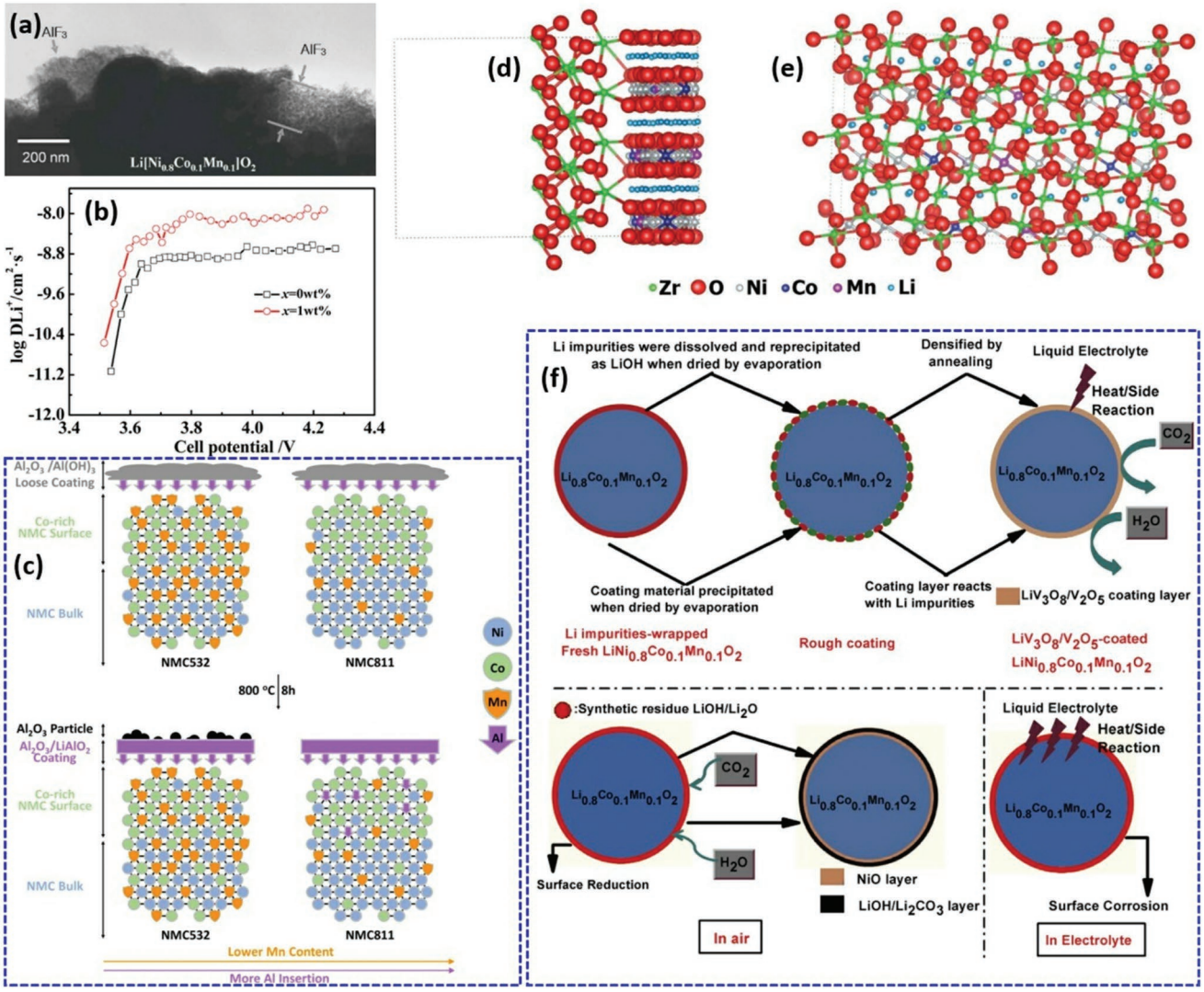

Figure 7. a) TEM image of AlF_3-coated NCM811. Reproduced with permission.[114] Copyright 2007, The Electrochemical Society. b) Comparison between Li^+ diffusion coefficient as a function of potential for xAl_2O_3-coated NCM811 samples where $x = 0$ and 1 wt%. Reproduced with permission.[115] Copyright 2017, American Chemical Society. c) Schematic comparison between surface evolution of Al_2O_3-coated NCM532 and NCM811 before and after annealing at 800 °C. Reproduced with permission.[116] Copyright 2017, American Chemical Society. Scheme of d) side view and e) top view of the most preferable interface of NCM811(110)/ZrO_2(001). Reproduced with permission.[29] Copyright 2018, Wiley. f) Scheme of coating LiV_3O_8/V_2O_5 on $Li[Ni_{0.8}Mn_{0.1}Co_{0.1}]O_2$ and its impact on suppressing unfavorable side reactions at the cathode–electrolyte interface. Reproduced with permission.[128] Copyright 2014, Elsevier.

insertion of Al cation into the lattice,[117,118] and consequently lead to aggregation of alumina particles on the cathode surface. On the other hand, Al_2O_3 coating can result in Al doping into the near-surface layers of NCM811 after annealing at high temperature (800 °C) due to the lack of Mn in its structure (Figure 7c). Initial content of Li on the cathode surface, amount of Al in the coating layer, and TMs segregation on the surface can determine the composition of interfacial layer on the cathode surface particles. It is worth to mention that penetration of alumina coating into the bulk structure has detrimental effect on cyclability and electrochemical performance.

Surface treatment of NCM cathode materials by Zirconium compounds shows great promises, particularly for NCM811. Woo et al.[119] applied a uniform sulfated zirconia (SO_4^{2-}/ZrO_2) coating layer on $Li[Ni_{0.8}Co_{0.1}Mn_{0.1}]O_2$. Although the sulfated ZrO_2-coated NCM811 delivered a slightly lower initial capacity compared to the pristine material (200 vs 203 mAh g^{-1} at 0.1 C rate and 4.3 V) due to its electrochemically inactive properties, it substantially enhanced the electrochemical and thermal performance. Sulfated zirconia coated-, zirconia coated- and pristine samples exhibited the capacity fade of 1.2%, 2.8%, and 8.9% at room temperature, and 11.1%, 20.8%, and 35.1% at 60 °C, respectively, after 50 cycles at 1 C rate within 3–4.3 V. It is suggested that Zirconia layer acts as a physical barrier to protect the cathode surface from undesirable reactions with electrolyte; alkyl sulfonate compounds can also modify the chemistry of the formed CEI layer and enhance the interfacial stability.

It is worth noting that, applying dual-function zirconium modification on NCM811 improves its electrochemical

performance to a large extent. For instance, Zr-modified NCM811 synthesized by Li et al.[120] showed a capacity retention of 92% after 100 cycles at 1 C rate, and a discharge capacity of 107 mAh g^{-1} at 10 C rate. Part of zirconium in form of Zr^{4+} diffuses into the cathode crystal structure near the surface induced by annealing during the synthesis process, and acts as pillar and increases the interlayer spacing, thus promoting the structural stability as well as Li^+ diffusivity. The rest of Zr forms a thin layer of amorphous Li_2ZrO_3 on the cathode surface and suppresses interfacial parasitic reactions. According to the XPS results, the ratio of Ni^{3+}-2p3/2 to Ni^{2+}-2p3/2 intensity is increased in Zr-modified material, which suggests that the presence of Zr–O bond can mitigate the evolution of excessive oxygen during calcination, thereby declining the formation of Ni^{2+} in the cathode structure. Schipper et al.[29] also combined zirconia-coating with Zr-doping on NCM811 via a scalable post-synthesis annealing (≥700 °C) wet-coating process using zirconium butoxide as precursor, providing a stable cathode–electrolyte interface, faster kinetics, lower impedance (R_{ct}), and improved cycle stability. They suggested that a stable interface between zirconia and cathode active materials can be formed with Li^+ diffusion channels. They modeled the most preferable and stable interface (shown in Figure 7d,e) with the lowest absolute mean strain value of about 9% at the interfacial distance of 2.0 Å using DFT calculation and coincidence site lattice method. The substitution energy E_{subs} calculation also revealed that the most preferred location for Zr substitution is the Nickel sites.

Liang et al.[121] applied an amorphous nanoscale (20–40 nm) SiO_2 coating layer on NCM811 via carbonic acid neutralization method. The cycle performance was significantly improved (capacity retention of almost 86% after 300 cycles at 1 C and 2.8–4.3 V with the same initial discharge capacity as the pristine material) even at high temperature (60 °C) and elevated cutoff voltage (4.4 V). Indeed, polarization gap and charge-transfer resistance during cycling decreased to a great extent. HF concentration in electrolyte also declined considerably due to the reaction with SiO_2, thereby slowing down the TMs dissolution. Dai et al.[122] applied Y_2O_3 coating on NCM811 via a wet-chemical method. Although the coating layer was detected to be nonuniform, it improved the electrochemical performance by promoting a stable interface and suppressing active materials dissolution, thereby maintaining low impedance and boosting lithium-ion diffusivity. 3 wt% yttria-coated sample delivered a capacity retention of 91.45% after 100 cycles at 1 C with slightly better initial capacity than the pristine sample as well as better capacity at higher rates. Finding better methods to form a uniform yttria coating on $Li[Ni_{0.8}Co_{0.1}Mn_{0.1}]O_2$ would result in even better cathode–electrolyte interface and consequently superior cell performance. Moreover, Although an optimized amount of CuO (2 wt%) coated on NCM811[123] improves the electrochemical performance, it is not as efficient as most of the other metal oxide coatings studied before.

Li-Reactive and Lithium-Ion Conductive Coating: Lithium residues remained from synthesis process can react with moisture, air or electrolyte compounds and re-precipitate on coating layer and even result in gas evolution, compromising the integrity and stability of the cathode–electrolyte interface and overall cell efficiency. As a result, some researchers' attention has been attracted to Li-reactive coating materials.[20] Cho et al.[124] coated $AlPO_4$ on $Li[Ni_{0.8}Co_{0.1}Mn_{0.1}]O_2$ via a wet-coating process. The thickness of coating was measured to be 10 nm. Rate capability and capacity retention improved substantially, i.e., capacity retention of almost 100% after 200 cycles at various discharge rates (from 0.2 to 0.5, 1, and 2 C) and charge rate of 1 C between 3 and 4.2 V, with initial capacity of almost 174 mAh g^{-1}. The differential scanning calorimetry (DSC) indicated an excellent thermal stability in coated sample. Coating of $AlPO_4$ on NCM811 significantly reduces exothermic reaction at delithiated states even at high voltages of 4.5 and 12 V. The cell surface temperature of the bare cathode reached 250 °C while that of the coated material did not exceed 110 °C, indicating that the coating material can considerably control the heat generation.[125] It is suggested that high-covalent nature of the bond between Al and $(PO_4)^{3-}$ makes the coating layer resistant to electrolyte reaction.[126] Indeed, the coating layer reduces the exposed surface of the cathode material to electrolyte and further declines the oxygen evolution and impedes the HF attack. The enhanced electrochemical performance of the coated sample may be also due to the Li reactivity of $AlPO_4$ which is able to react with residual lithium compounds, such as Li_2CO_3 and LiOH, on surface of the cathode material and control the chemistry of the surface in an effective way.

Xiong et al.[127] modified the surface of NCM811 by in situ coating of LiF. They used the optimized amount of NH_4F to precipitate the residual Li on the cathode surface and form a nanoarchitecture layer of HF inhibitor LiF to protect the surface of cathode particles from excessive HF attack. Despite the lithium insulating characteristic of LiF, a thin coated layer of this compound on $Li[Ni_{0.8}Co_{0.1}Mn_{0.1}]O_2$ resulted in improved rate capability and electrochemical performance, particularly at higher C rates and temperature, i.e., 2–10 C rates and 60 °C, respectively. Lithium-reactive V_2O_5 coating layer on NCM811 (studied by Xiong et al.[128,129]) also showed great promise as HF inhibitor/scavenger and protective layer which avoid undesirable contact between electrolyte and active surface area of the cathode particles. Indeed, V_2O_5 has superiority in Li^+ diffusivity and electrical conductivity compared to the most metal oxides, -phosphates, and -fluorides. A homogenous V_2O_5 coating layer with the thickness of 10–30 nm was obtained from the reaction of NH_4VO_3 and Li impurities (i.e., $LiOH/Li_2O$) on the surface of NCM811, followed by annealing. Formation of LiV_3O_8 is also inevitable due to the reaction of V_2O_5 with Li residues through calcination. A schematic view of this coating process and its effect on protecting the cathode surface is illustrated in Figure 7f.[128] V_2O_5-coated NCM811 shows considerably enhanced cycling performance, particularly at higher C rates and temperatures. For instance, the coated sample delivered a capacity retention of 76.6% after 100 cycles (60 °C, 2 C rate) with initial capacity of 173.4 mAh g^{-1} compared to that of 44.5% for the pristine material. The structural analysis also reveals that this coating layer can postpone Ni^{3+}/Ni^{2+} transformation. Moreover, the comparison between TEM images of the pristine and V_2O_5-coated cathode surface after 100 cycles at 60 °C, shown in **Figure 8**a,b,[129] indicates the effectiveness of the protective layer.

MoO_3 is another Li-reactive metal oxide with superior theoretical lithium storage, i.e., 1117 mAh g^{-1}.[130] Indeed, molybdenum trioxide possesses high Li^+ diffusivity[131,132] and

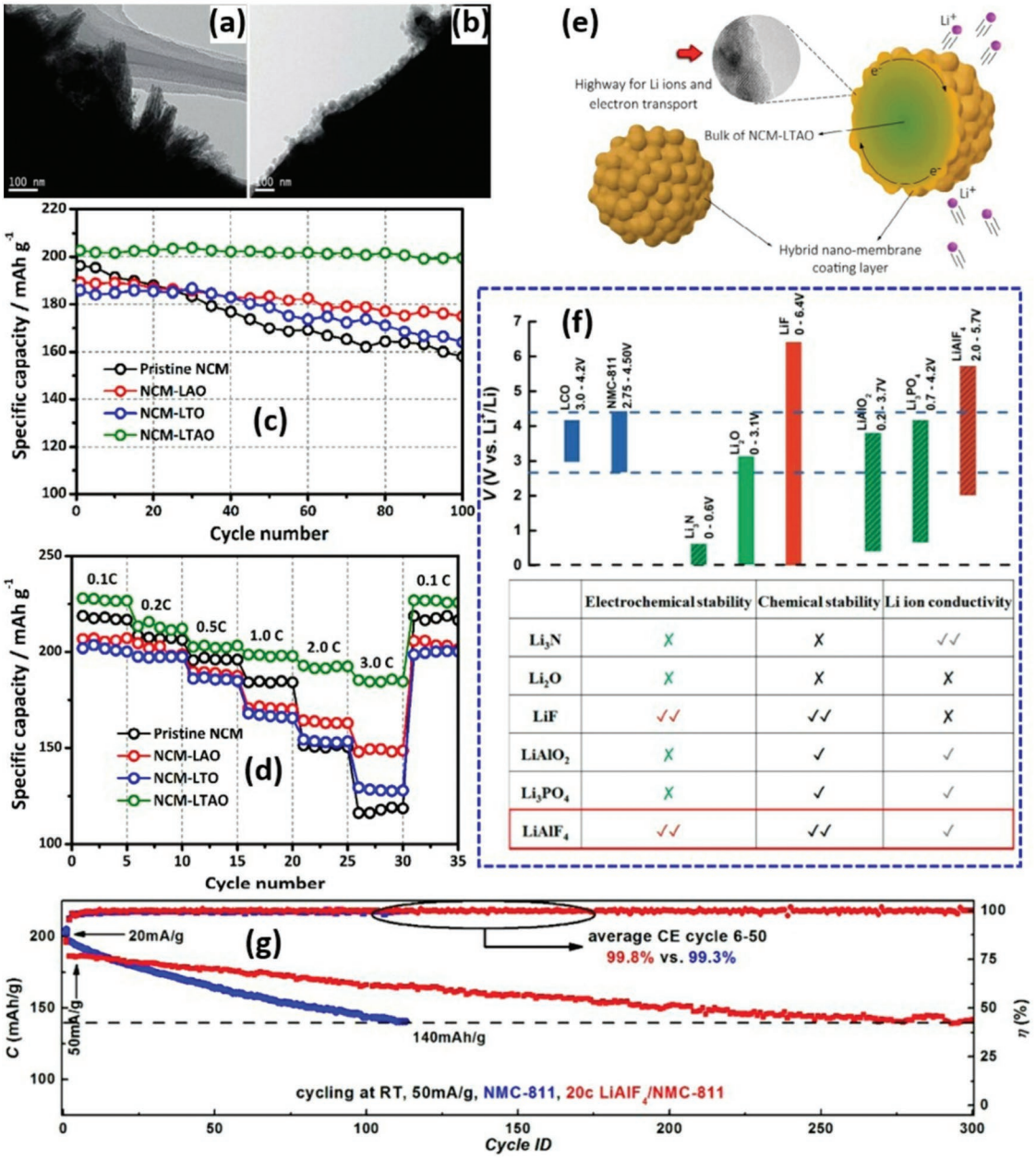

Figure 8. TEM images of a) pristine and b) V_2O_5-coated $Li[Ni_{0.8}Co_{0.1}Mn_{0.1}]O_2$ after cycling 100 times at 60 °C. Reproduced with permission.[129] Copyright 2013, Royal Society of Chemistry. c) Cycling performance at 0.5 C and d) rate capability of pristine NCM811, NCM811-LAO, NCM811-LTO, and NCM811-LTAO. e) Schematic illustration of the hybrid nanomembrane LTAO-coated NCM811. Reproduced with permission.[43] Copyright 2016, American Chemical Society. f) Electrochemical stability windows of several Li-containing materials as coating candidates for NCM811 along with some of their characteristics. g) Cycling performance of pristine and 20c ALD $LiAlF_4$-coated NCM811 between 2.75 and 4.5 V at room temperature. Reproduced with permission.[40] Copyright 2016, American Chemical Society.

superior thermodynamic stability[133,134] due to its particular open structure, and high Mo–O bond energy, respectively. Huang et al.[135] treated the surface of NCM811 with dry-coating of MoO_3/Li_2MoO_4 via a low velocity ball milling followed by calcination at 600 °C. In fact, Li_2MoO_4 is a product of MoO_3 reaction with lithium residues (Li_2O/LiOH) on the cathode surface during calcination. Molybdenum trioxide (3 wt%)-treated cathode shows improvement in initial coulombic efficiency (83.3% vs 89.0%), capacity retention (94.8% after 100 cycles, 2.8–4.3 V at 1 C) as well as rate capability. According to the results, a spinel structure with lithium-ion transition channels is formed at the interface of cathode–electrolyte, promoting Li^+ diffusion along with decreasing charge-transfer resistance and polarization at higher rates.

Recently, Lithium-ion conductors as a protective layer for high capacity Ni-rich cathode materials with the ability of providing 3D tunnels for facilitation of Li^+ transportation, suppressing parasitic interfacial reaction, and stabilizing

cathode–electrolyte interfacial structure have been attracted great attentions. Lithium titanium oxide (LTO) in its different phases (i.e., $LiTi_2O_4$, Li_2TiO_3, $Li_4Ti_5O_{12}$) have been studied by several researchers as a Li-ion conductive coating on NCM811 to improve its electrochemical performance. At 1 C rate between 2.7 and 4.3 V in room temperature, 1 wt% $LiTi_2O_4$-coated NCM[43] with initial capacity of 182 mAh g^{-1} after 100 cycles, 3 wt% Li_2TiO_3-coated NCM[136] with initial capacity of 164 mAh g^{-1} after 170 cycles, and 1 wt% $Li_4Ti_5O_{12}$-coated NCM[39] with initial capacity of 160 mAh g^{-1} after 170 cycles exhibit the capacity retention of 85%, 98%, and 76%, respectively, along with enhanced rate capability. The improvement is attributed to prevention of direct contact between cathode and electrolyte as well as better Li-ion diffusivity and electron conductivity. $LiAlO_2$ (LAO) have also been considered as Li-ion conductive coating for $Li[Ni_{0.8}Co_{0.1}Mn_{0.1}]O_2$. LAO-coated NCM811[43,137] prepared via hydrolysis–hydrothermal method has shown excellent electrochemical performance which can be ascribed to high Li^+ diffusivity as well as slight Al doping that enhances the structure stability of the cathode material. Li et al.[43] by employing a hybrid coating layer (denoted as LTAO), combining both LTO and LAO, via a scalable method substantially improved the cycling performance and rate capability of NCM811. LATO-coated NCM811 delivers a capacity of 187 mAh g^{-1} after 100 cycles at 1 C rate between 2.7 and 4.3 V with capacity fading of only 4%. A comparison between cycling performance and rate capability of LTAO-, LTO-, and LAO-coated NCM811 is shown in Figure 8c,d. Synergetic incorporation of $LiTi_2O_4$ and $LiAlO_2$ as a homogeneous coating layer and using lithium residues on the cathode surface as the Li source resulted in a stable interphase structure with the ability of rapid transportation of Li-ions and electrons between the bulk cathode material and electrolyte (schematically illustrated in Figure 8e) and decrease of impedance through cycling.

Figure 8f illustrates the operational electrochemical stability windows of several Li-containing materials as coating candidates along with some of their characteristics.[40,138] $LiAlF_4$ appears to be an excellent choice as a protective interfacial layer on cathode materials due to its high resistance toward oxidation and reduction together with its superior stability and ion conductivity. In this regard, Xie et al.[40] applied a thin film of $LiAlF_4$ via atomic layer deposition (ALD) method by implementing alternative sub-cycles of AlF_3 (aluminum chloride and titanium tetrafluoride) and LiF (lithium tert-butoxide and titanium tetrafluoride) directly on NCM811 electrode. As shown in Figure 8g the coated sample exhibits high capacity of 140 mAh g^{-1} after 300 cycles in a wide voltage window of 2.75–4.50 V while the capacity delivered by the pristine sample reaches to less than 140 mAh g^{-1} after only 113 cycles. Indeed, the average coulombic efficiency (CE) of the pristine cathode from 99.3% and 97.4% at room- and elevated temperature (50 °C) changed to 99.8% and 99.7%, respectively, showing that the high level of undesirable reactions between active cathode materials and electrolyte have been successfully impeded by the coating layer.

Li_3PO_4 is another Li-ion conductor and Li-reactive compound with high ionic conductivity ($\approx 10^{-6}$ Sm^{-1}) and strong bond between P and O in which PO_4^{3-} polyanions are able to react with lithium residues on the surface of cathode material.[139] As a coating material, it is able to substantially improve the electrochemical performance of NCM811 by primarily increasing Li^+ diffusivity and decreasing the charge-transfer resistance at cathode–electrolyte interface.[140,141] However, a thick coating of Li_3PO_4 can worsen the rate performance, thus the optimum amount of coating is suggested to be 1 wt%.[141] A facile one-step-calcination wet-chemical coating of Li_3PO_4 on $Ni_{0.8}Co_{0.1}Mn_{0.1}(OH)_2$ precursor (schematically shown in **Figure 9**a) has been proved as an efficient method to substantially boost the rate capability and cycle stability of the nickel-rich NCM811 by providing a stable interfacial layer.[140,141] $Li_4P_2O_7$ also shows great promise as an ion-conductive coating layer on $Li[Ni_{0.8}Co_{0.1}Mn_{0.1}]O_2$. As investigated by Hu et al.,[142] the coated sample delivers an initial capacity of 185.9 mAh g^{-1} with 93.9% retention, and 199.7 mAh g^{-1} with 88.3% retention, at 25 and 50 °C, respectively, after 100 cycles at 1 C rate. During coating process, LiH_2PO_4 reacts with the surface lithium impurities such as Li_2CO_3 and LiOH, followed by sintering, to form a uniform layer of $Li_4P_2O_7$ with an average thickness about 35 nm.

Amorphous nonstoichiometric Li-Zr-O[143] and crystalline Li_2ZrO_3[144] have also been investigated as coating materials for improving the properties of cathode–electrolyte interface in NCM811. The former reacts with residual lithium and enhance the cycling performance at elevated temperature (60 °C) with no significant change at room temperature. However, 1 wt% of the latter coated on $Li[Ni_{0.8}Co_{0.1}Mn_{0.1}]O_2$ with thickness of almost 10 nm delivers a superior capacity of 168.1 mAh g^{-1} after cycling 200 times at 1 C and 144.3 mAh g^{-1} at 10 C rate between 2.8 and 4.3 V (Figure 9b). Ion-conductive Li_2ZrO_3 coating provides 3D tunnels at the interphase layer for lithium-ion transportation through cycling. According to Zhao et al.[42] Li-ion conductor Li_2MnO_3 coating prepared by PVP-chelation and syn-lithiation method (schematically shown in Figure 9c) possesses layered/layered homostructure securely adhered to the cathode surface as well as 3D path for lithium transportation and a concentration-gradient Mn on the surface. Although the Li_2MnO_3-coated NCM811 provides a capacity retention of 83% after 150 cycles at 160 mA g^{-1} between 3 and 4.3 V, which is 14% more than the pristine one, the delivered capacity, i.e., 109 mAh g^{-1}, is not as high as those of other Li-ion conductive coatings. On the other hand, Li_2SiO_3 coating[145] effectively enhances the electrode-electrolyte stability at elevated cutoff voltage of 4.6 V and delivers 77.7% capacity retention (vs 57.6% for bare $Li[Ni_{0.8}Mn_{0.1}Co_{0.1}]O_2$) after 50 cycles at the current of 100 mA g^{-1}. Moreover, 3 wt% of Li_3VO_4[146] and $LaAlO_3$[147] as excellent ion conductors uniformly coated on $Li[Ni_{0.8}Co_{0.1}Mn_{0.1}]O_2$ via a facile wet-chemical-, and solid method, respectively, showed great promises. The significantly enhanced electrochemical performance of Li_3VO_4-coated sample is attributed to its superior Li^+ diffusion coefficient that is four times higher than that of the pristine sample after cycling 100 times (i.e., 4.83×10^{-12} cm^2s^{-1}). Indeed, the $LaAlO_3$-coated sample by reacting with lithium residues and providing remarkable Li^+ diffusivity could exhibit excellent cyclability even at high rates (Figure 9d–f).

Conducting-Polymer Coating: To date, conducting polymers have been studied by many researchers to optimize the function of different cathode materials in LIBs.[148–151] They can be absolutely effective in promoting the stability of

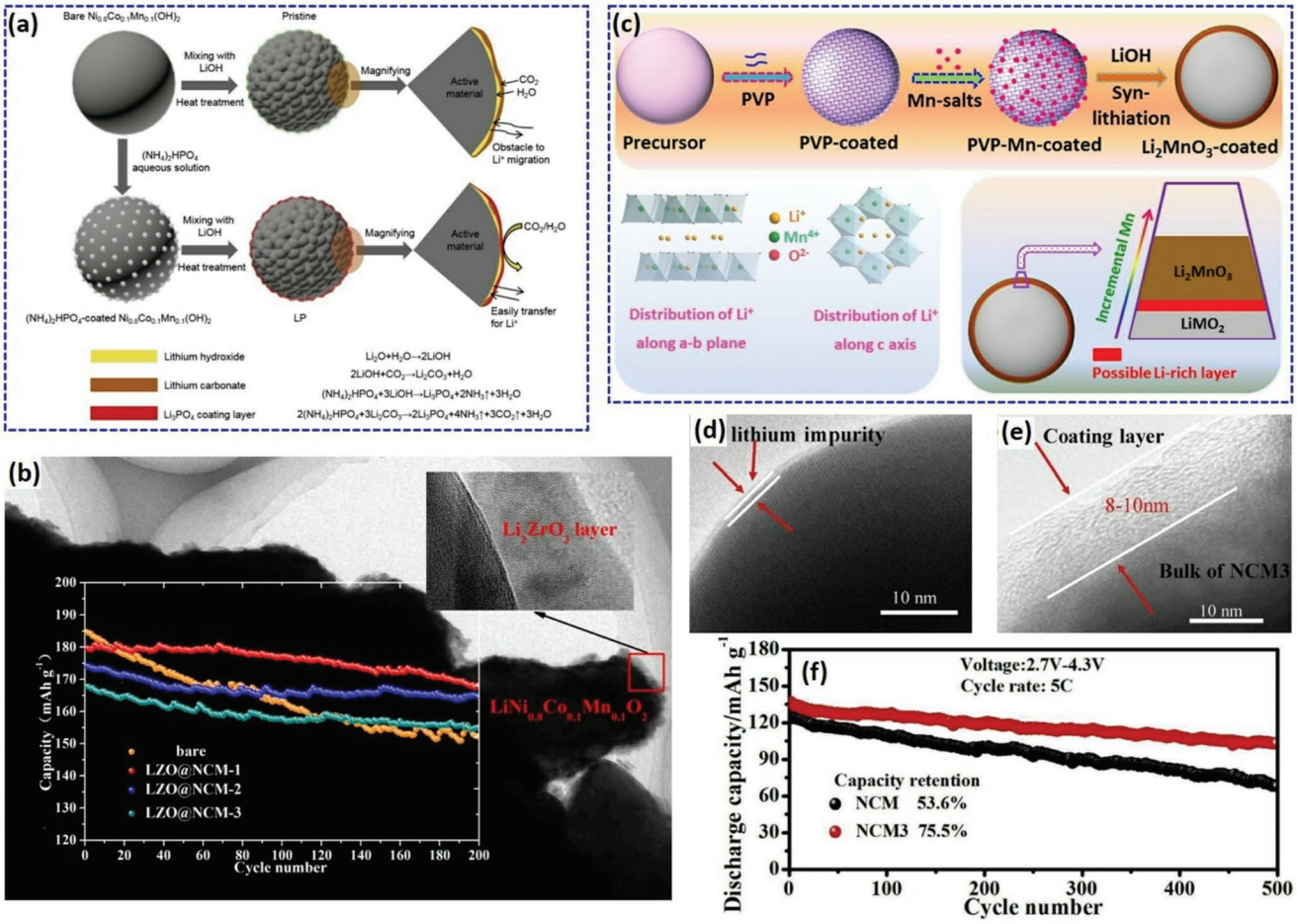

Figure 9. a) Schematic illustration of a facile one-step-calcination wet-chemical coating of Li_3PO_4 on $Ni_{0.8}Co_{0.1}Mn_{0.1}(OH)_2$ precursor compared to the pristine sample along with their surface chemistries. Reproduced with permission.[140] Copyright 2019, Elsevier. b) Combined image of the cycling performance of Li_2ZrO_3-coated NCM811 with three different concentrations of Li_2ZrO_3(LZO), i.e., 1, 2 and 3 wt%, and TEM image of the coating layer. Reproduced with permission.[144] Copyright 2017, Elsevier. c) Schematic illustration for the synthesis process of the Li_2MnO_3-coated NCM811; bottom left shows the structure of Li_2MnO_3 layer indicating Li^+ distribution along the *c* axis and *a–b* plane; bottom right shows the interface layer in detail. Reproduced with permission.[42] Copyright 2016, Elsevier. HRTEM of d) pristine NCM811 and e) $LaAlO_3$-coated NCM811 (denoted as NCM3). f) Cycling performance of NCM (representing NCM811) and NCM3 at 5 C between 2.7 and 4.3 V. Reproduced with permission.[147] Copyright 2018, Elsevier.

cathode–electrolyte interface structure in nickel-rich layered cathode materials, particularly NCM811. Polypyrrole (PPy) coating on $Li[Ni_{0.8}Co_{0.1}Mn_{0.1}]O_2$ via chemical polymerization method with Iron (III) tosylate and ethanol as the oxidant and solvent, respectively, shows great promise in maximizing its electrochemical performance.[152] A smooth nanoscale electron-conductive PPy coating layer efficiently impedes undesirable interfacial parasitic reactions, particularly at more severe conditions like high temperatures and voltages. **Figure 10**a,b shows improved cycling performance of PPy-coated NCM811 at 60 °C and high cutoff voltage of 4.5 V, respectively, compared to the pristine electrode at 2 C rate. Indeed, PPy-coated sample exhibits more alleviated ohmic polarization at high current densities due to its superior interfacial structural stability. Chen et al.[41] investigated the performance of NCM811 by dual-conductive coating of Li_3PO_4 and PPy as ion- and electron conductor, respectively. First $(NH_4)_2HPO_4$ reacts with Li residues and forms an inhomogeneous Li_3PO_4 layer, then PPy forms a uniform coating layer on surface of the cathode (schematically illustrated in Figure 10c). Apart from superior electronic and ionic conductivity of this dual-function coating layer, the structural stability of the interphase layer is improved due to the elastic characteristic of PPy, impeding the propagation of potential internal cracks over cycling.

Polyaniline (PANI) is another favorable polymer for the surface modification of $Li[Ni_{0.8}Co_{0.1}Mn_{0.1}]O_2$ owing to its nanowire-like structure, superb electronic conductivity, low cost, and easy preparation.[153,154] It can improve the cycling and rate performance of NCM811 to a great extent;[155] nevertheless, it is not an ion conductor. In this regard, Cao et al.[156] synthesized an integrated conducting composite polymer, denoted as PANI-PEG with electronic conductivity of 2.85×10^{-2} Scm^{-1}, using PANI and Poly ethylene glycol (PEG) as a lithium-ion conductor and lithium-salt solvent. An amorphous layer of PANI-PEG composite with high elasticity was homogeneously coated on NCM811 with a thickness of 30–35 nm via a wet-coating method. PANI-PEG-coated sample delivers more initial capacity than both pristine sample and PANI-coated

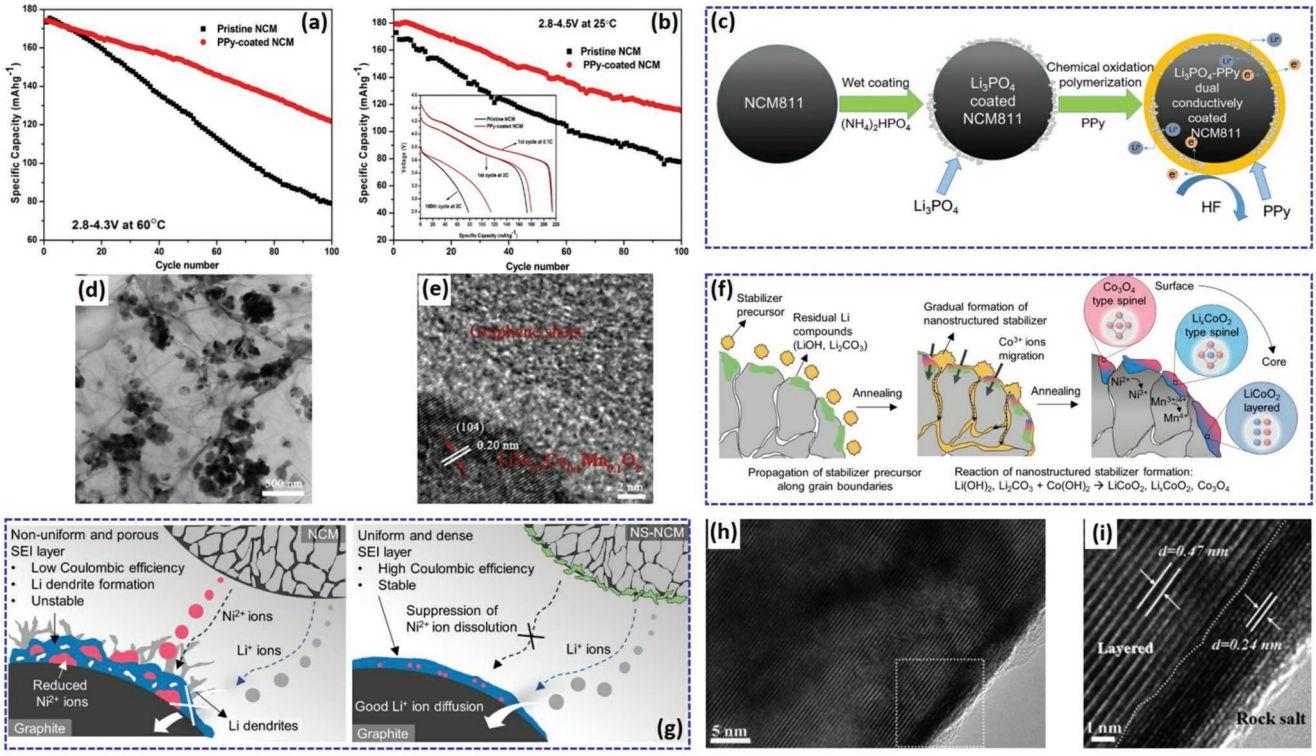

Figure 10. The cycling performance of pristine and PPy-coated NCM811 (2 C rate) at a) cutoff voltage of 4.3 V and 60 °C and b) cutoff voltage of 4.5 V and 25 °C; inset depicts the discharge profiles at various rates and cycles. Reproduced with permission.[152] Copyright 2014, Springer. c) Schematic illustration for preparation process of Li_3PO_4 and PPy dual-conductive coated NCM811. Reproduced with permission.[41] Copyright 2017, American Chemical Society. d) TEM image of the NCM811 enwrapped by graphene. e) HRTEM image of the NCM811/graphene interface area. Reproduced with permission.[157] Copyright 2014, Elsevier. f) Schematic illustration for preparation process of NS-NCM. g) Schematic illustration of the effect of epitaxially grown nanostructured stabilizer on suppressing Ni-ion dissolution and boosting the integrity of the anode SEI layer. Reproduced with permission.[158] Copyright 2018, Royal Society of Chemistry. h) HRTEM image of the cation-mixing nanolayer on the surface of NCM811 with rock-salt structure and i) the magnified image of the selected area in Figure 10h. Reproduced with permission.[160] Copyright 2016, The Electrochemical Society.

sample with only 6.7% fading after cycling 100 times at 1 C rate between 2.8 and 4.3 V. It also exhibits excellent rate capability and cycling performance at elevated temperature. Indeed, PEG as a Lewis base can effectively react with PF_5 in the electrolyte to intercept HF being generated from its hydrolysis.

3.1.2. Other Surface Treatments

Conductive graphene matrix is able to boost structural stability and electrical conductivity of the nickel-rich $Li[Ni_{0.8}Co_{0.1}Mn_{0.1}]O_2$ to a great extent. The NCM811 enwrapped by graphene (shown in Figure 10d,e) prepared by a simple chemical method could substantially promote the cycling performance without inducing any changes in structural integrity and lattice parameters.[157] The NCM-graphene composite exhibits much higher initial capacity and much less electrode polarization compared to the pristine electrode and delivers a discharge capacity of 167.5 mAh g^{-1} after cycling 150 times at 1 C between 2.8 and 4.3 V with capacity retention of 92.2% compared to that of 76.5% for the pristine one. Introducing highly conductive graphene with large surface area remarkably improves the kinetics and rate capability of the electrode by reducing the charge-transfer resistance.[157]

Cho's group[158] revealed that the cycling instability of NCM811 full-cells originates from dissolution of Ni^{2+} ions from cathode surface into the electrolyte and migration to the anode and formation of nickel particles in the anode SEI layer, further inducing a nonuniform porous layer along with the evolution of lithium dendrites. By introducing nanosized $Co(OH)_2$ as a stabilizer precursor to the surface of NCM material (denoted as NS-NCM) via a facile powder mixing followed by annealing, it penetrates into the inter-grain voids all over the cathode surface and reacts with lithium residues and forms an epitaxial nanostructured stabilizer layer (schematic illustration of the synthesis process is shown in Figure 10f). During this process Ni^{2+} to Ni^{3+} oxidation occurs under O_2 atmosphere above 300 °C, resulting in cobalt hydroxide to Co_3O_4 phase transformation and TM gradient formation with poor Ni and rich Co concentration at the surface which effectively impede microcrack generation and parasitic reaction with the electrolyte. Figure 10g schematically illustrates the effect of epitaxially grown nanostructured stabilizer on robustness and integrity of the anode SEI layer. The surface treated $Li[Ni_{0.8}Co_{0.1}Mn_{0.1}]O_2$ (denoted as NS-NCM) full-cell exhibits a capacity retention of 86% at 0.5 C charge and 1 C discharge rate between 2.8 and 4.2 V after 400 cycles at 25 °C and an excellent cycling performance with an average coulombic

efficiency of 99.8% at 45 °C. The thermal/structural stability of the treated-electrode are attributed to declined amount of Ni^{2+} ions by formation of TM concentration gradient at the cathode particle surface, reduction of cation mixing, and physical protection of the cathode surface by the nanostructured stabilizer compounds. On the other hand, $Co(OH)_2$ treated NCM811 by tang et al.[159] delivers less capacity than the pristine sample until 190th cycle, but exhibits a superior capacity retention of 81.4% (compared to that of 69.8% for the pristine cathode) after cycling 400 times in a pouch cell at 1 C between 3 and 4.2 V. The difference in results may be due to the different amount of precursor incorporation or dissimilarity between treatment processes.

Pre-cycling (5 cycles at 0.1 C) of NCM811 at high voltage (2–4.5 V) and then cycling in lower cutoff voltage of 4.3 V can surprisingly improve the structural/thermal stability and consequently cycle-life (83% capacity retention after 500 cycles) of this cathode material without any necessary chemical treatment.[160] In fact, an in situ cation-mixing nanolayer (≈3 nm) with rock-salt structure will form on the cathode surface which can efficiently impede further structural degradation of the balk layers through cycling (Figure 10h,i). Divalent nickel ions in this layer screen Oxygen–Oxygen repulsion during charge process and suppress other TMs to further migrate into the lithium sites, inhibiting structural collapse. Chao et al.[98,161,162] considerably improved the stability of cathode–electrolyte interface and impeded electrolyte decomposition in NCM811 by forming uniform artificial CEI layers on surface of the cathode material via simple, cost-effective and scalable synthesis processes with satisfactory enhancement of electrochemical performance. Formation of these CEI layers facilitates lithium diffusion while inhibits electron transfer. All the studied artificial CEIs with different compounds, i.e., Poly three-alkylthiophene (P3HT) with low molecular weight (36 KDa),[162] 0.5 wt% organic amphiphilic sodium dodecyl sulfate (SDS),[161] and 5 wt% organic amphiphilic SO_3-based,[98] result in superior cycling and overall electrochemical performance. Li et al.[163] also introduced 4-vinylbenzeneboronic acid (4-VBBA) to the surface of NCM811 to bond with the oxygen-containing groups and make the cathode surface less hydrophilic and more resistance to reaction with residual water in the electrolyte. Although this strategy could improve the electrochemical performance to some extent, it was not as effective as other methods mentioned earlier in this section.

In summary, to design a superior cathode–electrolyte interface for NCM811, disparate surface modification methods using various compounds with different characteristics studied so far have been reviewed in this section. A desirable modified surface has to be uniform with optimum thickness and protect the cathode surface from degradation by preventing parasitic side reactions, particularly with electrolyte compounds, and further suppress electrolyte decomposition, impede continuous phase transition and gas evolution, facilitate Li^+ diffusion and lower the interfacial impedance even at elevated voltages and temperatures. Nevertheless, an excellent surface modification strategy for improving the cycling performance, rate capability and thermal stability of NCM811 cathode material, despite from enhancing the robustness of cathode–electrolyte interface, has to be scalable and cost-effective. Possessing all these features would make NCM811 a favorable choice for commercialization as a promising cathode material for LIBs.

3.2. Structural Modification

Structural/thermal instability of NCM811 cannot be entirely resolved by means of solely surface modification. Ni-rich NCMs at highly delithiated states, particularly at high voltages, may endure oxygen vacancy, gas evolution and migration of Ni^{2+} to the Li slabs (cation-mixing), which may be the commence of phase transition, microcrack generation and further cathode–electrolyte interface degradation. In this regard, many researchers have studied on modifying the cathode structure to impede these degradations by employing different strategies. Among them, designing concentration-gradient structures and doping extrinsic ions are the most promising ones.

3.2.1. Concentration-Gradient Structure

Concentration-gradient structure has been studied by many researchers to overcome the shortcomings of high capacity nickel-rich layered cathode materials by promoting electrode-electrolyte interfacial stability, structural integrity and chemical properties, minimizing side reactions, and impeding detrimental volume changes. It can be divided into three major categories (**Figure 11**a), i.e., core–shell structure (CS), shell concentration-gradient structure (SCG), full concentration-gradient structure (FCG). Co-precipitation method, duo to its unique mechanism, has been considered as the most suitable synthesis strategy to prepare the precursors of this type of cathode materials. High nickel and manganese concentration at the inner and outer layers in this type of structure, respectively, can stabilize the interface of cathode–electrolyte in $Li[Ni_{0.8}Co_{0.1}Mn_{0.1}]O_2$ by confining the degradation of active materials due to the lack of highly active Ni^{4+} and presence of inactive Mn^{4+} in near-the-surface regions.[111,164] Concentration-gradient structure restricts cation mixing and subsequently formation of $Fm\bar{3}m$ space groups and disordered phases during cycling, thereby reducing interfacial impedance and improving cyclability.[165]

Core–shell structure with high-capacity nickel-rich NCM811 (thickness of about 13 μm) as the core encapsulated in a lower-active thermally/structurally stable $Li[Ni_{0.5}Mn_{0.5}]O_2$ (thickness of about 2 μm) shell was first developed by Sun et al. (Figure 11b).[166] The cathode exhibited an initial capacity of 188 mAh g^{-1} at 40 mA g^{-1} between 3.0 and 4.3 V and owing to the advantage of its Ni-rich core and Mn-rich shell a remarkable long-term cycling and superior onset temperature of the exothermic decomposition (250 °C) were obtained. Sun's group further developed more CS-cathode materials such as $Li[(Ni_{0.8}Co_{0.2})_{0.8}(Ni_{0.5}Mn_{0.5})_{0.2}]O_2$[167] and $Li[(Ni_{0.8}Co_{0.1}Mn_{0.1})_{1-x}(Ni_{0.5}Mn_{0.5})_x]O_2$[168,169] with improved electrochemical performance, and paved the way for evolution of more efficient CS-cathode materials. For example, CS-$Li[(Ni_{0.8}Co_{0.1}Mn_{0.1})_{0.7}\ (Ni_{0.45}Co_{0.1}Mn_{0.45})_{0.3}]O_2$[170] exhibits superior cycling stability at elevated temperature (55 °C) and various cutoff voltages (4.3, 4.4, and 4.5 V) compared to the same non-core–shell cathode material. Additionally,

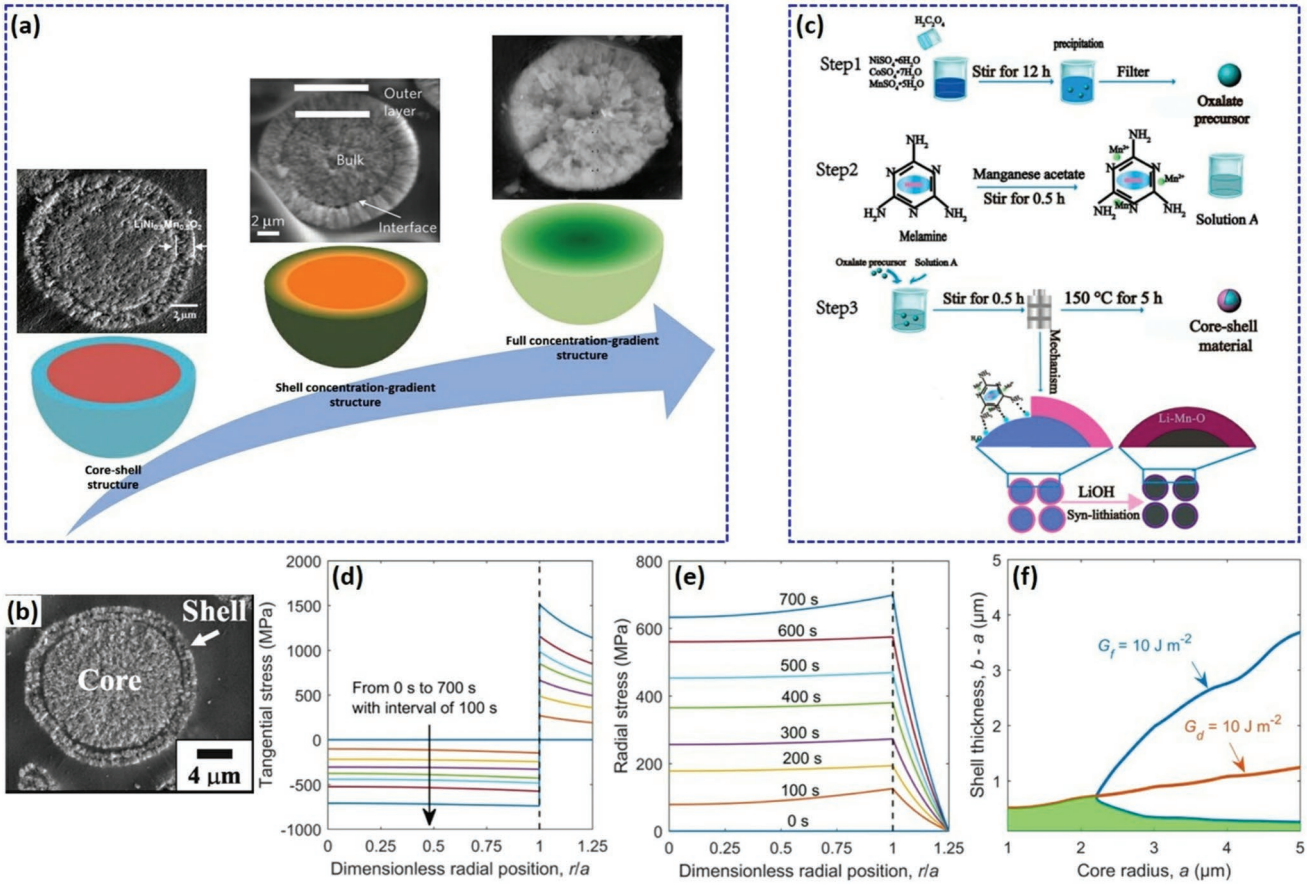

Figure 11. a) Schematic illustration of three major categories of concentration-gradient structures. Reproduced with permission.[17] Copyright 2009, Macmillan Publishers Limited. Reproduced with permission.[167] Copyright 2006, American Chemical Society. Reproduced with permission.[175] Copyright 2014, Elsevier. b) SEM image of core–shell structure. Reproduced with permission.[168] Copyright 2006, The Electrochemical Society. c) Schematic view of the preparation process of core–shell structured $Li[Ni_{0.8}Co_{0.1}Mn_{0.1}]O_2$@0.03[Li–Mn–O]. Reproduced with permission.[171] Copyright 2018, American Chemical Society. Radial distribution of d) tangential stress and e) radial stress at eight times during Li intercalation and deintercalation, respectively, in core–shell structured cathode with $Li[Ni_{0.8}Mn_{0.1}Co_{0.1}]O_2$ core and $Li[Ni_{0.4}Mn_{0.4}Co_{0.2}]O_2$ shell. f) Design map for the core–shell structure; the green region signifies the appropriate design area. Reproduced with permission.[34] Copyright 2017, American Chemical Society.

CS-$Li[Ni_{0.8}Co_{0.1}Mn_{0.1}]O_2$@0.03[Li–Mn–O][171] synthesized via a different method (schematically shown in Figure 11c) delivers a satisfactory electrochemical behavior at the high current of 10 C, i.e., capacity of 118 mAh g^{-1} with almost 82% retention after 200 cycles. The improved rate performance is due to the ultrathin stable spinel-structured shell which provides 3D paths for Li^+ diffusion along with large proportion of the high-capacity Ni-rich core. Indeed, CS-$Li[(Ni_{0.8}Co_{0.1}Mn_{0.1})_{0.9}(Ni_{1/3}Co_{1/3}Mn_{1/3})_{0.1}]O_2$[172] shows its superiority when cycles at 2 C and 60 °C, indicating that superiority of core–shell cathode materials are more accentuated at high rates and elevated temperatures.

In general, cathode particles during lithiation encounter tensile radial stress. Nevertheless, in CS-cathode materials due to the restricting function of the shell, radial stress in opposite direction (compression) will be exhibited. To offset this effect, an extensive discontinuous tangential stress at the core–shell interface takes place (Figure 11d) which may cause shell fracture. Upon delithiation, the core experiences more contraction than the shell, leading to a considerable radial stress (Figure 11e) at the core–shell interface which may result in debonding between the two parts.[34] A rapid degradation in capacity and cycling performance would appear if each of these two failure mechanisms happens during cycling due to its severe impact on Li^+ diffusivity and electronic conductivity. For example, emerging of a gap at the core–shell interface of CS-$Li[(Ni_{0.8}Co_{0.2})_{0.8}(Ni_{0.5}Mn_{0.5})_{0.2}]O_2$ due to the difference in crystal structure have been reported.[17,167] Wu et al.[34] by simulation of mechanical reaction of the core–shell $Li[(Ni_{0.8}Co_{0.1}Mn_{0.1})_{1-x}(Ni_{0.4}Mn_{0.4}Co_{0.2})_x]O_2$ upon cycling and using fracture/debonding energy release rates have created a design map (Figure 11f), in which the safe region for choosing appropriate shell thickness and core radius to avoid any structural failure have been marked by green color. According to this diagram, a shell thickness more than 0.7 μm is not recommended, and a shell narrower than 0.18 μm is compatible with the core radius up to 5 μm.

To deal with the shortcomings of core–shell cathode materials, Sun et al.[17] reported a novel cathode material with high capacity NCM811 as the core encapsulated by a concentration-gradient outer layer (**Figure 12**a) with less Ni and more Mn and Co concentration from the core edge (i.e., 8:1:1) toward the surface (i.e., 4.6:3.1:2.3). The smooth change of

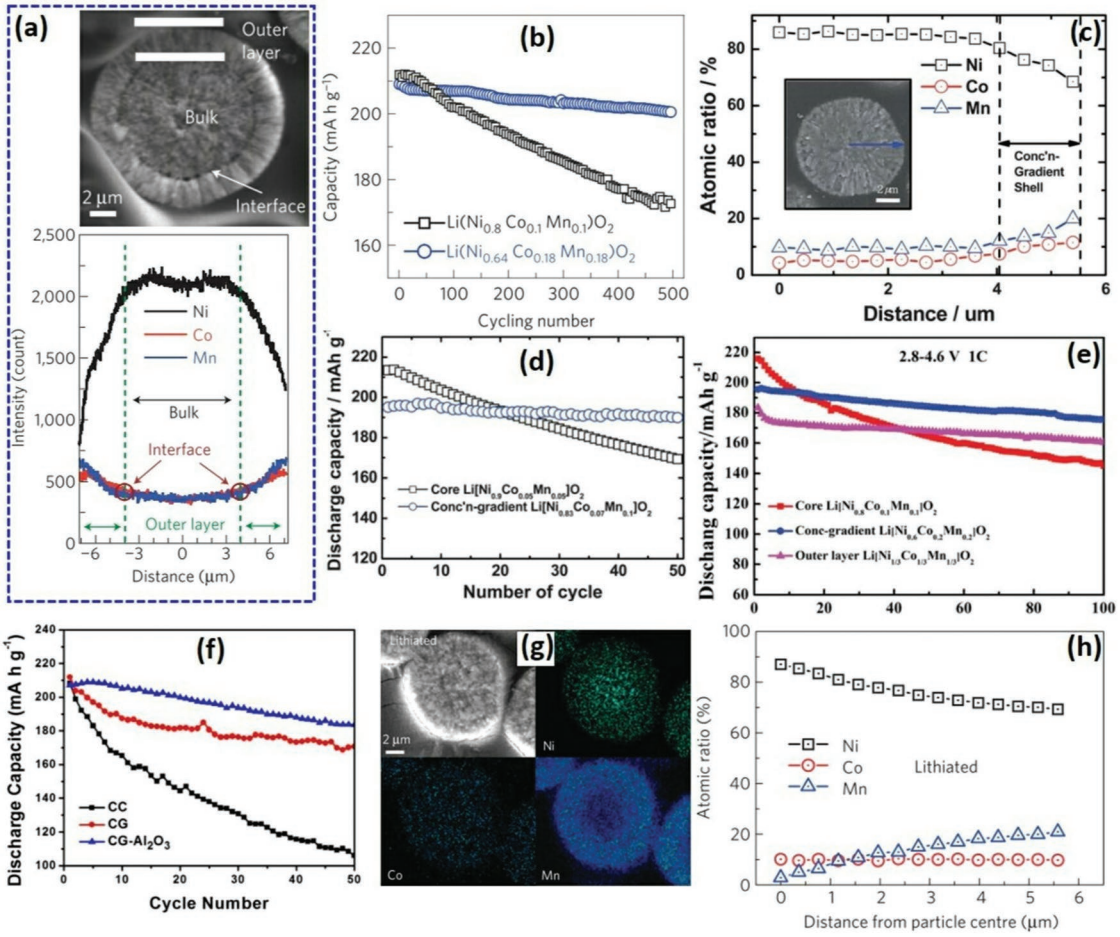

Figure 12. a) SEM and EPMA compositional-change for SCG-cathode with NCM811 as the core encapsulated by a concentration-gradient outer layer. b) Cycling performance at 1 C (cutoff voltage of 4.2 V) in an Al-pouch full-cell with graphite anode and either $Li[Ni_{0.8}Co_{0.1}Mn_{0.1}]O_2$ or SCG material with NCM811 core as the cathode. Reproduced with permission.[17] Copyright 2009, Macmillan Publishers Limited. c) EPMA compositional-change (inset is cross-sectional SEM image) of SCG-$Li[Ni_{0.83}Co_{0.07}Mn_{0.1}]O_2$ from center toward surface of the cathode particle. d) Cycling performance of SCG-$Li[Ni_{0.83}Co_{0.07}Mn_{0.1}]O_2$ in comparison with $Li[Ni_{0.90}Co_{0.05}Mn_{0.05}]O_2$. Reproduced with permission.[164] Copyright 2011, Royal Society of Chemistry. e) Cycling performance of SCG-$Li[Ni_{0.6}Co_{0.2}Mn_{0.2}]O_2$ with NCM811 in the core surrounded by CG-NCM111 at 1 C between 2.8 and 4.6 V. Reproduced with permission.[165] Copyright 2018, Royal Society of Chemistry. f) Cycling performance of alumina-coated-SCG-$Li[(Ni_{0.8}Co_{0.1})_{0.7}(Ni_{0.2}Mn_{0.8})_{0.3}]O_2$ compared to the pristine (CC) and uncoated (CG) samples. Reproduced with permission.[173] Copyright 2015, Elsevier. g) SEM elemental mapping and h) EPMA compositional-change in lithiated state for FCG-cathode material. Reproduced with permission.[174] Copyright 2012, Macmillan Publishers Limited.

the TMs concentration in the shell layer effectively alleviates the radial stress at core–shell interface through de-/lithiation and improves the cycling performance of the SCG-cathode in a great extent. As shown in Figure 12b, SCG-cathode in an Al-pouch full-cell with a mesocarbon microbead graphite as the anode cycled at 190 mAh g^{-1} between 3 and 4.2 V can deliver an initial capacity of almost 210 mAh g^{-1} with only 3.5% decay after 500 cycles. Later, they reported SCG-$Li[Ni_{0.83}Co_{0.07}Mn_{0.1}]O_2$[164] (Figure 12c) with initial discharge capacity of 195 mAh g^{-1} with only 3.1% decay after 50 cycles at the cutoff voltage of 4.3 V (Figure 12d).

The SCG cathode materials have shown good promises at high cutoff voltages owing to their unique structure. As a case in point, SCG-$Li[Ni_{0.6}Co_{0.2}Mn0_{.2}]O_2$[165] with NCM811 in the core surrounded by CG-NCM111 exhibits an initial capacity of 196 mAh g^{-1} with only 10% decay after cycling 100 times at 1 C between 2.8 and 4.6 V (Figure 12e). It also delivers a superior capacity of 153.1 and 167.6 mAh g^{-1} at 5 C and 2 C, respectively. Moreover, other modification methods can be applied to further promote the electrochemical performance of SCG-cathode materials. For example, Manthiram's group[173] studied alumina-coated-SCG-$Li[(Ni_{0.8}Co_{0.1})_{0.7}(Ni_{0.2}Mn_{0.8})_{0.3}]O_2$ with considerably enhanced cycling and thermal stability. The treated sample provides 205 mAh g^{-1} at 1/5 C rate (cutoff voltage of 4.5 V, 55 °C) with 11% capacity decay after 100 cycles (Figure 12f).

Although SCG-cathodes exhibit better electrochemical properties than CS-cathodes in general, sometimes the thickness of concentration-gradient shell is not adequate to guarantee the stability of the cathode structure, particularly at higher temperatures. Hence, Sun and Amine's group[174] introduced the full concentration-gradient cathode synthesized via a modified

co-precipitation method in which the concentration of nickel and manganese gradually decreases and increases in a linear manner, respectively, from center toward the surface of each particle (Figure 12g,h). The FCG-cathode exhibited an excellent initial capacity of 215.4 mAh g^{-1} at the current density of 44 mA g^{-1} and high cutoff voltage of 4.5 V with only 12% decay after 100 cycles. In situ HEXRD further confirmed its superior thermal stability and safety properties. So far, FCG-cathode materials have been proved to be efficient in optimizing capacity, cycling stability and rate performance of nickel-rich cathode materials such as NCM811. For example, FCG-NCM811[175] showed an initial capacity of almost 203 mAh g^{-1} (1 C, 2.8–4.3 V, 55 °C) with good cycling stability (**Figure 13**a) as well as superb rate capability (175 mAh g^{-1} at 2 C).

Moreover, to take full advantage of Ni-rich inner layers and Mn-rich outer layers in FCG cathode materials, a two-sloped full-concentration gradient cathode (denoted as TSFCG) was developed by Sun's group[176] with extra Ni-rich\Mn-poor core decreasing\increasing smoothly and then steeply toward the outer layers (TMs atomic ratio from center toward the surface is shown in Figure 13b).The TSFCG-Li$[Ni_{0.8}Co_{0.06}Mn_{0.14}]O_2$ shows an excellent cycling performance (Figure 13c) with 94.6% capacity retention after 100 cycles (105 mAh g^{-1}, 2.7–4.3 V). Indeed, EIS results prove a stable cathode–electrolyte interface with low impedance due to the low concentration of nickel at near-the-surface layers. They further incorporated Al into the structure via co-precipitation to obtain Al substituted-TSFCG-Li$[Ni_{0.84}Co_{0.06}Mn_{0.09}Al_{0.01}]O_2$ (shown in Figure 13d).[177] The presence of Al^{3+} could effectively lower the cation disorder and boost the structural stability and consequently cycling performance. The cathode after cycling 100 times at 0.5 C could deliver an outstanding discharge capacity of 197 mAh g^{-1} (capacity fading of only 4.9%) at 4.3 V and 202 mAh g^{-1} (capacity retention of almost 90%) at 4.5 V (Figure 13e).

In spite of substantial electrochemical improvements achieved by employing nickel-rich cathode materials with concentration gradient structure, particularly regarding stabilizing cathode–electrolyte interface, the practical application of them in commercialized LIBs notably depends on their preparation method. The current synthesis method is a multistep, costly and highly sensitive procedure due to the need for a precise control over every co-precipitation parameter during the entire process. Hence, optimization of the preparation route in future studies is of great significance.

3.2.2. Doping Extrinsic Ions

Utilizing extrinsic ions as doping elements inside the NCM layered structure have been broadly studied as an effective strategy to deal with structural and thermal instability and promoting the capacity retention of Ni-rich cathode materials, and NCM811 in particular. Generally, employing dopants leads to decline in discharge capacity due to the decrease in

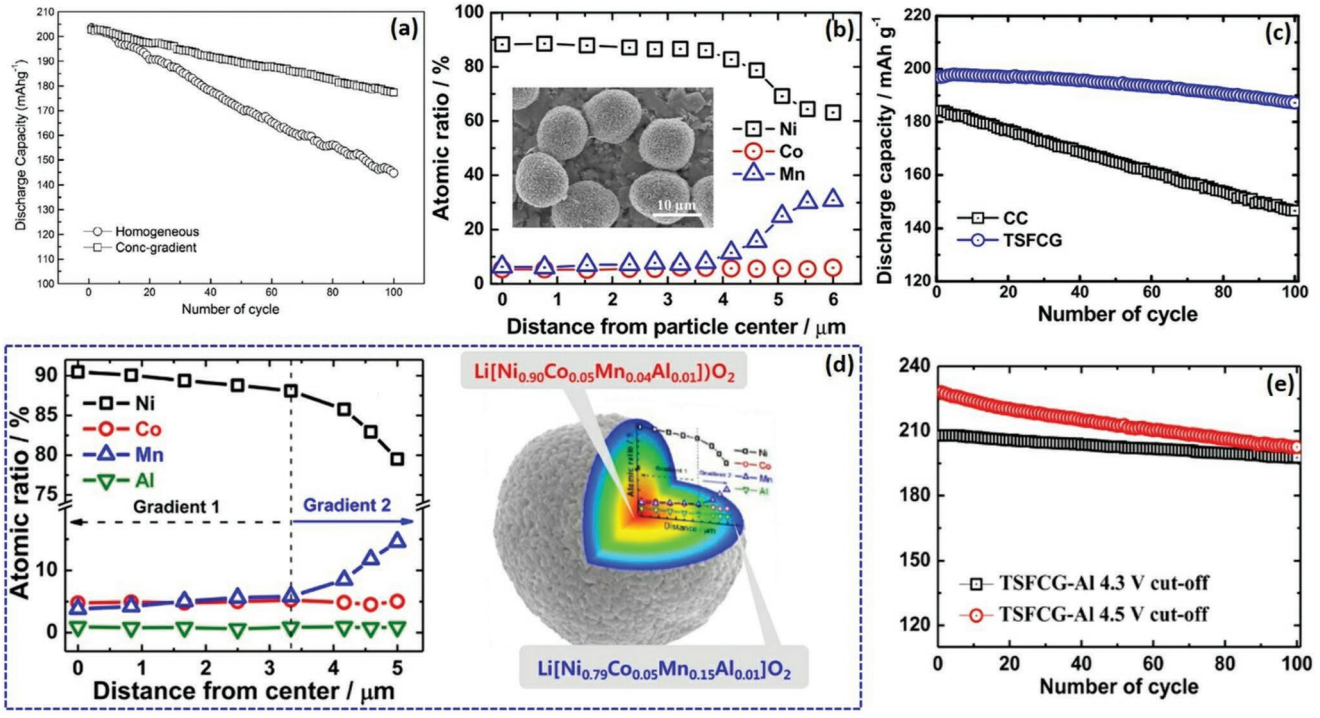

Figure 13. a) Cyclic performance of the homogenous- versus FCG-NCM811 cells at 1 C between 2.8 and 4.3 V at 55 °C. Reproduced with permission.[175] Copyright 2014, Elsevier. b) SEM and EPMA line scan of the TMs atomic ratio as a function of distance from the particle center for TSFCG-Li$[Ni_{0.8}Co_{0.06}Mn_{0.14}]O_2$. c) Cycling performance of half-cells employing homogenous (CC) and TSFCG cathodes cycled between 2.7 and 4.3 V at the current of C/2. Reproduced with permission.[176] Copyright 2015, Royal Society of Chemistry. d) EPMA line scan results for Al substituted-TSFCG-Li$[Ni_{0.84}Co_{0.06}Mn_{0.09}Al_{0.01}]O_2$ from center toward surface of the particle along with its schematic composition. e) Cycling performance of Al substituted-TSFCG-Li$[Ni_{0.84}Co_{0.06}Mn_{0.09}Al_{0.01}]O_2$ between 2.7 and 4.5 V at the current of C/2. Reproduced with permission.[177] Copyright 2016, American Chemical Society.

concentration of electrochemical active ions in the structure. Hence, optimizing the dopant ratio to reach a balance between capacity and stability is of great importance. The major tasks of the doping ions in Ni-rich NCM cathodes can be categorized into four disciplines to inhibit: 1) cation mixing and consequently unfavorable phase transformation; 2) distortion of lattice and further microcracking; 3) clustering of Mn (Co) and further surface Ni segregation; 4) oxygen evolution by increasing M–O bonding strength. Indeed, all of the above-mentioned effects are in tight relationship with the interphase layer as discussed earlier in Section 2. Therefore, employing doping elements strongly influences the stability of the cathode–electrolyte interface.

It is noteworthy that employing one dopant cannot address all of these issues; it may even fix one problem and aggravate the others.[178] Hence, having knowledge about the influence mechanism of each dopant and mitigating their side effects are indispensable for boosting the overall performance. Anion dopants can substitute oxygen in 6c site and cation dopants, which are more prevalent and practical in case of NCM811, can substitute Ni, Mn, Co (3a) or Li (3b) sites.[179] Considering the "heat of formation" value,[180] most dopants are able to migrate into TM sites but rarely in Li sites (except for some dopants such as Mg^{2+}[47,179,181] and Zr^{4+}[182]). Indeed, substitution at Co sites in most cases enhances charge transfer and phase stability, while Mn sites substitution impedes gas evolution and cation mixing.[180]

Cation mixing or Ni-Li exchange can occur through synthesis process or cycling whereby divalent nickel ions migrate to Li slabs and lithium ions may migrate to TM layers, hindering Li^+ insertion/extraction and further worsening rate capability and capacity retention. It can be suppressed by reducing the amount of Ni^{2+} by doping appropriate cations (preferably with lower valence)[183] in TM sites, or doping more stable cations with the same formation energy as Li-Ni exchange (such as Mg^{2+} and Zr^{4+} which possess ionic radius close to that of Li^+, i.e., 0.72 vs 0.76 Å) in Li slabs to prevent Ni^{2+} migration.[180] In addition, these stable ions in Li sites, unlike Ni ion which possesses multiple oxidation states, can act as pillars during delithiation and screen oxygen atoms repulsion, thereby stabilizing the structure.[184] It is worth noting that reducing the amount of Ni^{2+} is not always desirable. For example, interaction between Co^{3+}, Mn^{4+} and Ni^{4+} with Ni^{2+} is much stronger than that with Ni^{3+}. Therefore, formation of individual clusters of Mn or Co ($Mn^{4+}Mn^{4+}$ and $Co^{3+}Co^{3+}$) and Ni segregation in absence of divalent nickel is more probable; hence substituting high and low valence dopants at the same time in different sites can be helpful for tuning Ni with different oxidation states.

Lattice distortion problem, on the other hand, cannot be entirely solved by employing doping strategy. **Figure 14**a,b[180] show the lattice parameters *a* and *c* and the overall volume change of doped-NCM811 as a function of lithium content during delithiation. Notably, doping elements cannot decrease

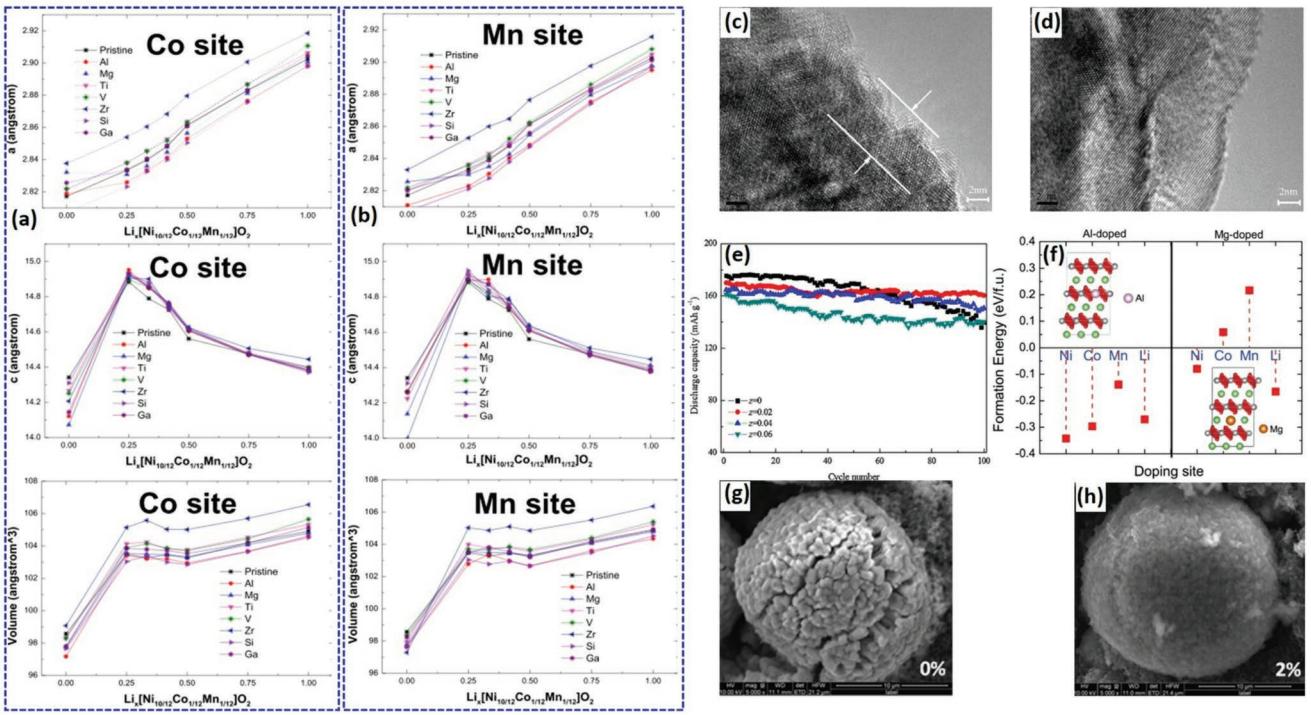

Figure 14. Calculated lattice parameters, *a*, *c*, and volume of doped NCM811 as a function of Li content at a) Co sites and b) Mn sites. Reproduced with permission.[180] Copyright 2017, Royal Society of Chemistry. TEM image of $Li[Ni_{0.8}Co_{0.1}Mn_{0.1}]O_{2-z}F_z$ ($z = 0$, 0.02) electrodes after cycling 100 times at room temperature for c) $z = 0$ and d) $z = 0.02$. e) Cycling performance of $Li[Ni_{0.8}Co_{0.1}Mn_{0.1}]O_{2-z}F_z$ at the current density of 400 mAh g^{-1} at room temperature. Reproduced with permission.[188] Copyright 2013, Elsevier. f) The formation energy of doping Al and Mg at Ni, Co, Mn, and Li sites; insets show the preferable doping sites for Al (top left) and Mg (bottom right), which are nickel and lithium sites, respectively. Reproduced with permission.[47] Copyright 2017, Royal Society of Chemistry. SEM images of $Li[Ni_{0.8}Co_{0.1}Mn_{0.1}]O_2$ after 200th cycle for g) the pristine and h) 2% Ti-doped $Li[Ni_{0.8}Co_{0.1}Mn_{0.1}]O_2$. Reproduced with permission.[189] Copyright 2015, Elsevier.

the lattice distortion to a great extent and even show detrimental effects in some cases. Nonetheless, doping can positively affect the redox potential during cycling in normal voltage range and prevent large lattice distortion from happening. Moreover, oxygen evolution as a damaging phenomenon responsible for instability of nickel-rich cathodes can be controlled by doping. Dopants which possess stronger bonds with oxygen ion compared to nickel can alleviate oxygen evolution to a great extent. Nevertheless, only redox active elements like Zr,[182] Ti[185] and V[180] can mitigate the oxidation of oxygen atoms at elevated voltages and highly delithiated states, by being oxidized at the end of charge process. Anion doping is regarded as an effective strategy to improve thermal and structural stability of the cathode and stabilize the discharge potential plateau by being partially substituted with O^{2-}.[48]

Between anion candidates, F^- have been considered as the most promising one in improving electrochemical properties of $Li[Ni_{0.8}Co_{0.1}Mn_{0.1}]O_2$.[186–188] Stronger Li–F bonds (577 kJ mol^{-1}) compared to Li–O bonds (341 kJ mol^{-1}) together with stronger bonds between TMs and fluorine cause more stable structure. In addition, substitution of fluorine in oxygen sites results in partially reduction of trivalent nickel (0.56 Å) to divalent nickel (0.69 Å) along with more repulsion in oxygen matrix, thereby expanding the lattice parameters *a* and *c*.[186,187] F-substituted NCM811 can maintain a stable cathode–electrolyte interface, well-layered structure and protect the surface from HF attack even after long cycling (Figure 14c,d). Indeed, an optimized amount of F^- dopant can substantially boost the cycling performance even at a high rate of 400 mA g^{-1} (Figure 14e).[188]

To date, many cations, such as Al^{3+},[47,181] Mg^{2+},[47,179–181] Ti^{4+},[185,189] Zr^{4+},[120,182,190,191] Ca^{2+},[192] Si^{4+},[180] Mn^{3+},[193] V^{5+},[180] Zn^{2+},[194] Cr^{3+},[195,196] Ga^{3+},[180] La^{3+},[197] Y^{3+},[198] Rb^+,[199] and Mo^{6+},[133] have been studied as dopants for structural modification of Ni-rich NCM811. Fe substitution in NCM cathode materials with high nickel content has not shown great improvements.[20] It lowers discharge capacity and Li^+ diffusivity and increases Ni-ions oxidation potential. On the other hand, Cr as another electrochemically active element can promote Li-ion diffusion as well as discharge capacity, and reduce Jahn-Teller distortion when doped into the NCM811 structure.[196] Ionic radius of Ni^{2+} and Cr^{3+} are almost similar (0.69 vs 0.62 Å) and with Cr-doping the amount of active ions in the structure increases. As reported by Li et al.,[196] $Li[Ni_{0.79}Co_{0.1}Mn_{0.1}Cr_{0.01}]O_2$ prepared by fast co-precipitation can deliver a capacity of 164.2 mAh g^{-1} at 5 C with almost 11% fading after 50 cycles (2.7–4.3 V). Nevertheless, uncontrolled excessive Cr-doping leads to fast capacity fading and undesirable cycling performance owing to the formation of Mn^{3+} as well as Cr^{6+} which partially occupy the lithium sites.[195]

Moreover, co-substituted NCM811 by Cr and Mg, in which Cr resides in Ni sites and Mg occupies Li sites, have shown prominent enhancement in electrochemical properties.[179] Al-Mg pair-doping is another efficient way of enhancing electrochemical properties of NCM811.[47,180,181] Incorporation of these two dopants into the host structure increases the strength of TM–O bonds. It is reported that substitution of Al and Mg in Mn sites minimizes both cation mixing and phase stability.[181] However, both experimental and computational studies reveal that the most preferred doping locations for Al and Mg are Ni and Li sites, respectively.[47,200] Figure 14f illustrates the preferable doping sites for Al and Mg in detail, regarding their formation energy calculated by DFT method.[47] Al doping can impede cation disordering as well as evolution of oxygen vacancies, boosting thermal stability; at the same time, substituted Mg suppresses structural failure and lattice distortion by occupying lithium location in 3b site.[47,181]

Ti^{4+} is another cation (ionic radius 0.60 Å) with many advantages as a dopant. According to Liang et al.[180] substitution of Ti in Mn and Co sites can be helpful for phase stability and preventing Mn (Co) clustering, respectively, but detrimental for cation mixing. However, Jiang et al.[194] reports that Ti-doped NCM811 experiences only 1.6% cation mixing compared to 2.9%, 2.67% and 1.97% for the pristine, Mg-doped and Al-doped samples, respectively, suggesting that the preferred location for Ti substitution is probably Ni sites. Indeed, Ti substitution strengthens M–O bonds, particularly Ni–O, to a great extent (i.e., more than that in Al-, Mg-, and Zn-substituted samples), resulting in more stable M–O network and consequently less oxygen vacancies and gas evolution which leads to more thermal and structural stability.[194] Figure 14g,h show the SEM images of 2% Ti-doped NCM811 after cycling 200 times, indicating effective role of Ti doping on alleviating lattice distortion and extreme volume changes.[189] Ti-doped $Li[Ni_{0.8}Co_{0.1}Mn_{0.1}]O_2$ can exhibit a capacity retention of 93.8%[194] and 86.9%[189] after 200 cycles at 1 C with cutoff voltages of 4.3 and 4.5 V, respectively. Despite the good cycling stability, the improvement in rate capability is not much significant due to the heightened polarization after Ti doping.[185,189]

On the other hand, Zr-substituted NCM811 shows excellent rate performance and cycling behavior. Zr can modify the cathode performance by being doped into TM and Li sites, and forming a Li-rich layer (i.e., Li_2ZrO_3) on the surface, simultaneously. Although some studies only discussed about the formation of Li_2ZrO_3 coating layer,[144,201] the others confirm the presence of both doped and coated Zr but present different mechanisms.[120,182,190,191] He et al.[182] report a Zr-modified $Li[Ni_{0.8}Co_{0.1}Mn_{0.1}]O_2$ with gradient concentration of Zr^{4+} into the layered structure (i.e., higher amount at the outer layers) as well as a lithium-ion conductive Li_2ZrO_3 layer on the surface. $I_{(003)}/I_{(104)}$ ratio (denoted as *R*) obtained from the Rietveld refinement results is indicative of cation mixing degree; a value above 1.2 means that the amount of cation mixing is acceptable and the structure has maintained its layered form. It is worth noting that doping of Zr^{4+} heightens the amount of Ni^{2+} for the sake of charge compensation. However, the value of *R* for the Zr-modified sample increases, indicating that despite the increased amount of Ni^{2+}, cation mixing is alleviated. It suggests that part of Zr^{4+} ions reside in Li slabs owing to their similar ionic radius and prevent Ni^{2+} cations from exchanging their places with Li^+. The substituted Zr^{4+} cations in TM and Li slabs guarantee the stability of crystal structure (because of strong Zr–O bond) and reduce cation mixing and lattice distortion (because of pillar effect), respectively. The Zr gradient-concentration is beneficial for weakening the obstructive effect of Zr ions in Li sites and strengthening their pillar effect, resulting in superior rate and cycling performance (i.e., 164.7 mAh g^{-1} at 10 C and 83.2% capacity retention after 200 cycles at 1 C between 2.8 and 4.5 V). Besides, the ion conductive Li-rich coating layer can

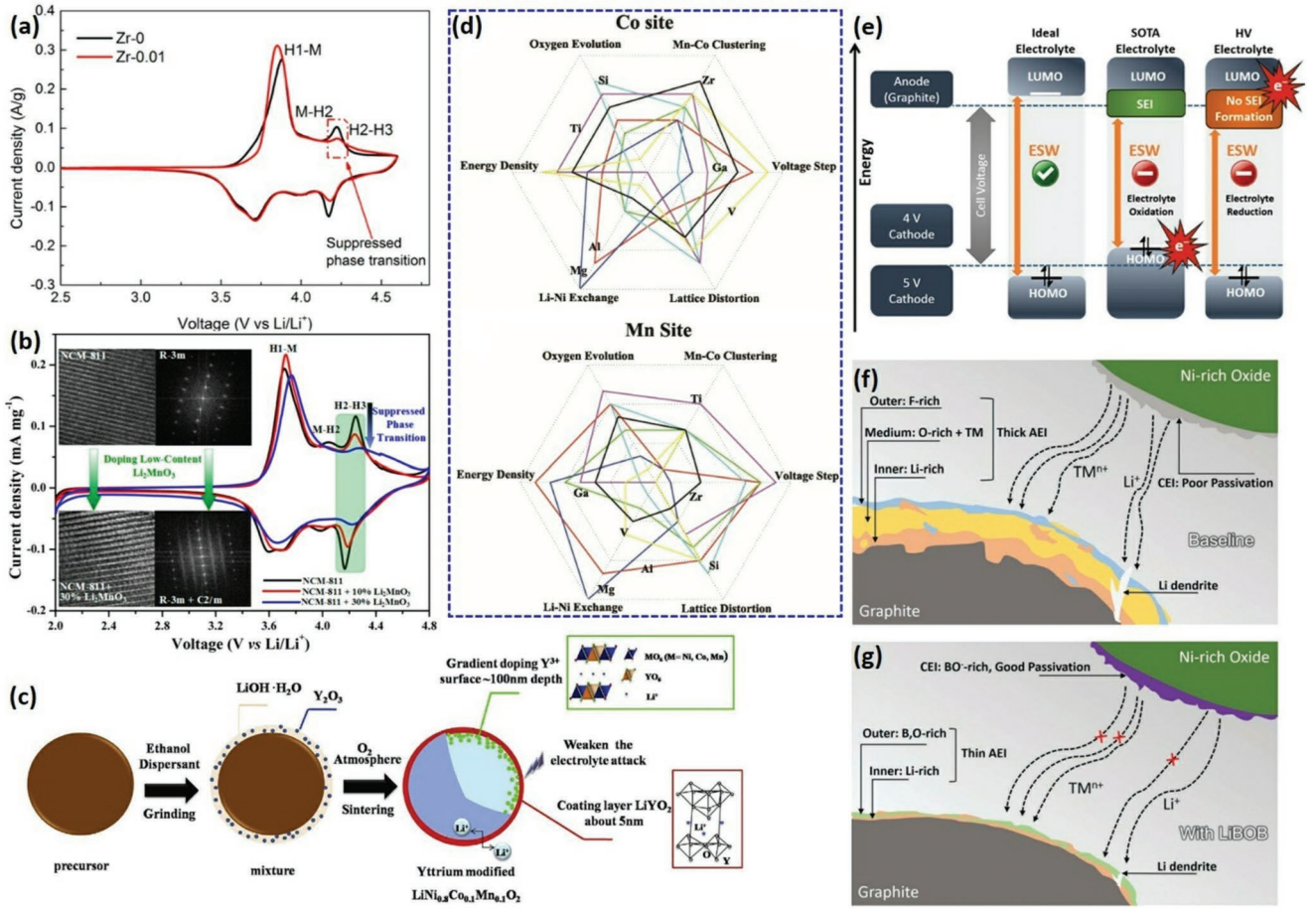

Figure 15. a) First cycle CV curves for the pristine (Zr-0) and Zr-doped (Zr-0.01) NCM811 with a scan rate of 0.1 mV s^{-1} between 2.5 and 4.6 V. Reproduced with permission.[182] Copyright 2018, Wiley. b) CV curves of the pristine and Li_2MnO_3-modified NCM811 between 2 and 4.8 V; insets show HRTEM images before and after modification. Reproduced with permission.[70] Copyright 2016, American Chemical Society. c) Schematic illustration of synthesis process of Y-modified NCM811 cathode material. Reproduced with permission.[198] Copyright 2019, Elsevier. d) Spider plots of doping impact of each element (at Co and Mn sites) on different electrochemical and structural properties of NCM811. Reproduced with permission.[180] Copyright 2017, Royal Society of Chemistry. e) Schematic energy diagram of a Li-ion battery with graphite anode, 4 and 5 V cathode, and various electrolytes, i.e., an ideal electrolyte, a state-of-the-art (SOTA) $LiPF_6$/organic carbonate-based electrolyte and a high-voltage (HV) thermodynamically stable electrolyte; the electrochemical stability window (ESW), LUMO energy level, and HOMO energy level are depicted as well. Reproduced with permission.[33] Copyright 2018, Springer. Schematic illustration of Impact of passivated CEI layer (on the surface of Ni-rich cathode) on AEI formation (on the surface of graphite anode) during long-term cycling with f) baseline electrolyte and g) LiBOB-modified electrolyte. Reproduced with permission.[209] Copyright 2018, Wiley.

boost Li^+ diffusion and impede undesirable cathode–electrolyte side reactions. CV curves of the first cycle for the Zr-modified and pristine sample (illustrated in **Figure 15**a) displays a lower polarization after Zr doping. Additionally, the H2 to H3 (with two different hexagonal structures) peak at 4.23 V is considerably abated after Zr doping, revealing its effectiveness in suppressing the phase transformation during de-/lithiation.

Han et al.[191] despite employing the almost same synthesis method report a different mechanism of effect. The results indicate that Zr partially migrates into the bulk structure and a nanothick (≈5 nm) Zr-concentrated cation-mixed layer forms on the surface, in which part of Ni^{2+} occupy Li sites and inhibit further Li^+/Ni^{2+} disordering by applying repulsive force. The modified $Li[(Ni_{0.8}Co_{0.1}Mn_{0.1})_{0.985}Zr_{0.015}]O_2$ delivers a capacity retention of 93.2% after cycling 100 times at 1 C between 2.8 and 4.5 V. Li et al.[120] report an increase in Ni^{3+}/Ni^{2+} ratio in Zr-modified NCM811 and attributes it to the stronger Zr–O bond which effectively mitigates oxygen evolution, hence minimizing the formation of divalent nickel. According to Gao's group,[190] Li_2ZrO_3 layer only forms on 5 at% Zr-modified NCM811 and for lower concentration of Zr other Li-rich zirconates, such as Li_4ZrO_4 and $Li_6Zr_2O_7$ would appear on the surface, and the rest of Zr^{4+} ions reside in TM sites. Mn surface doping is another effective strategy for stabilizing the structure of $Li[Ni_{0.8}Co_{0.1}Mn_{0.1}]O_2$.[70,193,202] Li_2MnO_3-modified NCM811 with stable structure and excellent high-voltage (2–4.8 V) cycling performance is a good example in which Li_2MnO_3 is effectively integrated with the crystal structure and efficiently suppresses H2 to H3 phase transition and further anisotropic lattice-changes (Figure 15b).[70]

Moreover, doping of low-valent Ca^{2+}[192] and Rb^+[199] with large ionic radius (1 and 1.52 Å, respectively) is reported to

decrease the formation of Ni^{2+} and consequently cation disordering, lower the polarization, and increase the Li^+ diffusivity. On the other hand, high-valent Mo^{6+} (0.59 Å) with smaller ionic radius close to that of Mn^{4+} (0.53 Å), Co^{3+} (0.54 Å), Ni^{3+} (0.56 Å), and Ni^{2+}(0.69 Å) occupies TM sites and maximizes the formation of Ni^{2+} due to the charge compensation, thus increasing the cation mixing in case of high-concentration doping. It is reported that substitution of Mo with Mn in NCM811 declines the amount of oxygen evolution for 54%, resulting in a superior thermal stability.[133] Cations of rare earth elements, such as lanthanum (La^{3+}) and yttrium (Y^{3+}) possess large ionic radii, high electric charge and self-polarization capability. Formation of a cation-mixed (perovskite phase) layer of $La_2Li_{0.5}Co_{0.5}O_4$ on La-doped $Li[Ni_{0.8}Co_{0.1}Mn_{0.1}]O_2$ has been reported by Wang's group.[197] The La-doped sample maintains 95.2% of its initial capacity after 100 cycles at 1 C. Zhang et al.[198] reports a Y-modified NCM811 with gradient-concentration of doped Y^{3+} and a nanothick lithium-conductive $LiYO_2$ layer generated from the reaction of Y_2O_3 and Lithium residues on the cathode surface (synthesis process is shown in Figure 15c). The 2 mol% Y-modified sample stabilizes the cathode–electrolyte interface, lowers polarization, boosts Li^+ diffusivity, and more importantly, delivers an excellent capacity retention of 98.4% after 100 cycles (0.5 C rate, 2.8–4.5 V).

Moreover, Liang et al.[180] employed DFT method to study the doping effect of seven cations, i.e., Mg^{2+}, Al^{3+}, Ti^{4+}, Zr^{4+}, Si^{4+}, Ga^{3+}, and V^{5+}, on the electrochemical properties of $Li[Ni_{1-2y}Co_yMn_y]O_2$ ($y \leq 0.1$) in order to design optimized multidoping strategies with minimized side reactions. Because only a few dopants can reside at Li sites (such as Mg and Zr), and Ni sites contain the primary redox active ions in the cathode structure, Mn and Co sites have been considered as the preferred doping sites in their study. Figure 15d illustrates the impact of some selected dopants on Li-Ni exchange, lattice distortion, Mn (Co) clustering, voltage, energy density and oxygen evolution. In this regard, substitution of Ti or Zr at Co sites and Al at Mn sites has been proposed as a promising multidoping strategy.

Summarily, utilizing extrinsic ion substitution method, particularly multidoping strategy in different fitting doping sites, is able to boost the electrochemical properties of the cathode to a great extent by effectively adjusting the characteristics of the cathode–electrolyte interface through controlling cation exchange, surface reconstruction, oxygen evolution and microcrack generation in high nickel-containing layered NCM811 cathode material. Nevertheless, at elevated cutoff voltages (i.e., more than 4.2 V) in which more lithium will be extracted from the cathode structure during the charge process, doping approach can hardly suppress oxygen evolution and lattice distortion. Accordingly, employing other modification strategies, such as coating or concentration-gradient structure, along with optimized amount of appropriate dopants regarding their mechanism of effects, can be a proper direction for future studies.

3.3. Electrolyte Modification

$Li[Ni_{0.8}Co_{0.1}Mn_{0.1}]O_2$ as a high-capacity positive electrode for LIBs suffers from poor cycling and safety performance which is partly attributed to instability of electrode–electrolyte interphase (EEI). The electrolyte plays a significant role in formation, composition and function of this interphase layer. To date, different groups of electrolytes, i.e., ionic liquid based, liquid aqueous, polymeric, hybrid and ceramic solid have been employed in LIBs;[203,204] but the most prevalent and commercialized one is organic solvent-based electrolyte consisted of a lithium salt (e.g., $LiPF_6$) and several organic solvents. In this regard, the modification strategies recommended in this section have been applied to this group of electrolytes.

The LUMO's energy level for the electrolyte is lower than the anode (i.e., graphite) electrochemical potential (schematically shown in Figure 15e).[33] Thermodynamic volatility of the EEI leads to reduction of electrolyte by receiving electron from the anode until a preferable insulating SEI layer forms at the anode–electrolyte interface, which impedes further reduction while allows Li-ion transportation.[205] Moreover, high-voltage NCMs (e.g., 5 V) are significantly restrained by the low-range (i.e., 1–4.4 V) electrochemical stability window (ESW) of the state-of-the-art (SOTA) carbonate-based electrolytes, resulting in undesirable side reaction, TMs dissolution, electrolyte decomposition, chemical oxidation and further gas evolution and capacity fading.[206,207] Indeed, their electrochemical potential is theoretically under the highest occupied molecular orbital (HOMO)'s energy level of the electrolyte, yielding electrolyte oxidation by electron transfer to the cathode until an efficient insulating passivation layer forms at the cathode–electrolyte interface.[33] It is worth nothing that these formed interphases on cathode/anode–electrolyte interfaces (i.e., CEI and AEI, respectively) can considerably affect each other and further overall cell operation and efficiency.[108,208] For example, Manthiram's group,[209] very recently, tailored a boron-oxygen-rich CEI on a Ni-rich cathode material by employing 1.5% lithium bis(oxalate) borate (LiBOB) in a carbonate-based electrolyte. As a result, parasitic side reactions and electrolyte decomposition at the cathode surface were substantially inhibited and Li-ion diffusivity increased. Time-of-flight secondary ion mass spectrometry (TOF-SIMS) revealed the positive effect of the newly formed CEI on the chemical composition and thickness of the AEI layer (schematically shown in Figure 15f,g). Accordingly, LiBOB as an electrolyte additive could effectively promote the cycling performance of the Ni-rich/graphite cell (80% capacity retention after 500 cycles) by perfectly tuning the composition of CEI and further AEI layer. Therefore, one efficient way to boost the stability of these interphase layers and other properties of the battery cell is the modifying of electrolyte formulation by employing appropriate amount of functional additives (i.e., ≤ 5 wt%) without changing the overall properties of the electrolyte.[205,210]

A host of electrolyte additives have been studied so far, which can be categorized regarding their specific targeted application (**Figure 16**a).[33] The function of EEI-forming additives (e.g., Vinylene carbonate (referred to VC) as the most studied one)[108,204] is to be reduced/oxidized by electrochemical reactions before the main electrolyte compounds in order to form a nanothick insoluble AEI/CEI on the anode/cathode surface to act as a shield and impede electrolyte decomposition.[98] To date, several comprehensive studies regarding the function of different electrolyte additives in NCM/graphite LIBs[211,212] (including NCM111, NCM532 and NCM622) have been done.

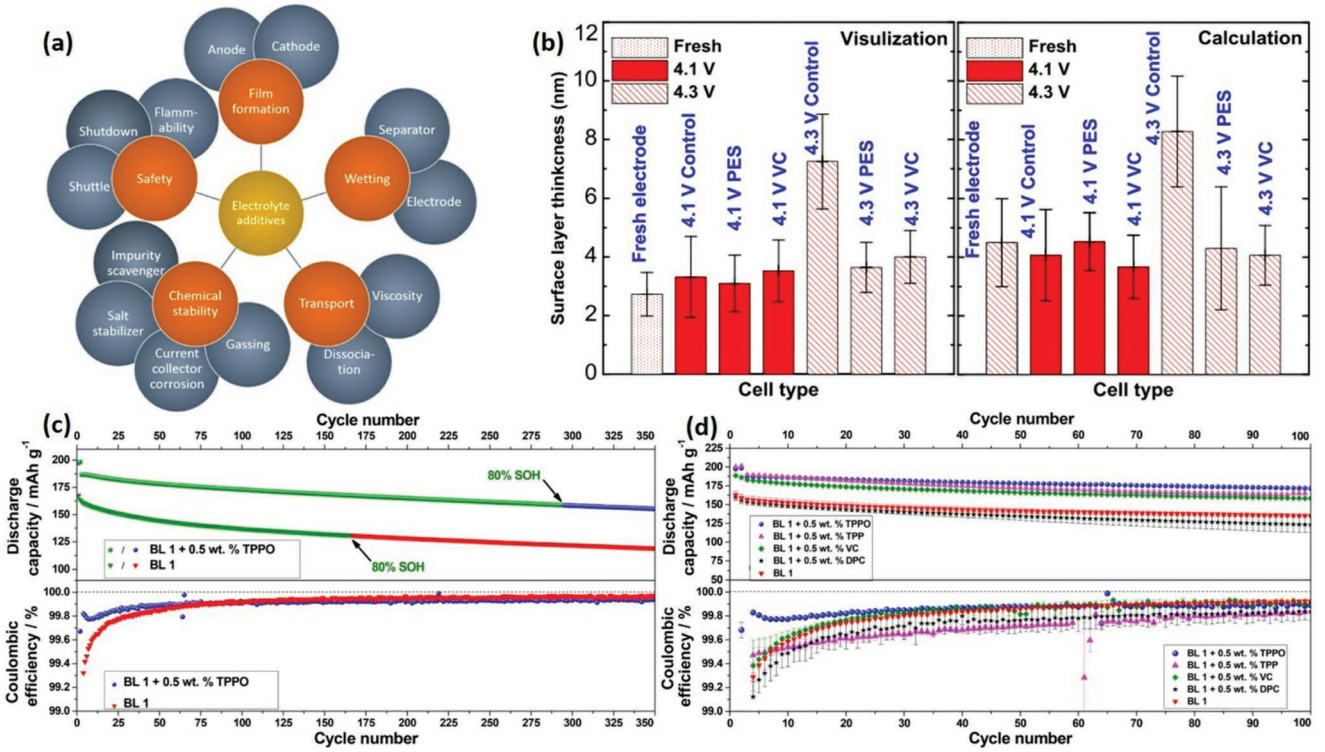

Figure 16. a) Target functions of different electrolyte additives in LIBs. Reproduced with permission.[33] Copyright 2018, Springer. b) Summary of the surface thickness of the rock-salt layer on the surface of NCM811 as a function of cutoff voltage and electrolyte additives (i.e., 2% VC and 2% PES) determined visually (left diagram) and by image analysis (right diagram). Reproduced with permission.[213] Copyright 2017, The Electrochemical Society. c) Comparison between long-term cycling performance of the cells (NCM811/graphite) with TPPO-included/excluded electrolytes; BL 1 (= 1 M $LiPF_6$, EC/EMC 3:7 by wt.). d) Cycling performance of the cells (NCM811/graphite) with TPPO-included electrolytes compared to various promising electrolyte additives, i.e., TPP, VC, and DPC. Reproduced with permission.[214] Copyright 2018, American Chemical Society.

However, they do not necessarily yield the same results in case of NCM811 due to its unique characteristics and surface chemistry. For example, prop-1-ene-1,3-sultone (PES), VC, methylene methane disulfonate (MMDS), and trimethyl silyl phosphite (TMSPi), which are able to substantially enhance the cycling stability of NCM111-442/graphite, were confirmed not to adequately improve the NCM811/graphite LIBs performance.[72,84] The major failure is attributed to the high impedance particularly when cycling above 4.2 V.

Li et al.[213] investigated the function of cutoff voltage and electrolyte additives (i.e., 2% VC and 2% PES) in formation and suppression of cation-mixed layer on the surface of NCM811 through cycling. It was revealed that a rock-salt layer begins to severely grow when the cutoff voltage exceeds 4.1 V, which can be substantially suppressed by employing appropriate electrolyte additives (Figure 16b). Nonetheless, the sample with PES and VC as additives still suffered from rapid capacity fading and high impedance growth, respectively, indicating that poor performance of the cell cannot be merely attributed to the growth of the rock-salt layer on the cathode surface. In a research conducted by Qiu et al.,[72] the effectiveness of two electrolyte additives, namely diphenyl carbonate (DPC) and methyl phenyl carbonate (MPC), have been studied either separately or as a ternary additive combination along with TMSPi and MMDS in a NCM811/graphite pouch-cell. The results of ultrahigh precision coulometry (UHPC), gas measurements, AC impedance spectroscopy as well as long-term cycling tests reveal the superiority of the sample with 1 wt% DPC compared to those with other electrolyte additives. Employing 1 wt% DPC reduces gas evolution (while MPC increases it) and impedance growth, and improves capacity retention, coulombic efficiency and voltage stability during storage. Indeed, it is believed that undesirable parasitic reactions at the cathode–electrolyte interface have been considerably impeded due to the smaller slippage rate in the charge endpoint capacity through cycling. It is worth mentioning that neither of the additives was reduced prior to ethylene carbonate (EC) on the anode, indicating that they act as AEI modifiers rather than AEI formers.

Recently, Beltrop et al.[214] introduced nontoxic and low-cost triphenylphosphine oxide (TPPO) as an excellent electrolyte additive for $Li[Ni_{0.8}Co_{0.1}Mn_{0.1}]O_2$/graphite cell. 0.5 wt% TPPO was added to two slightly different carbonate-based electrolytes (= 1 M $LiPF_6$, EC/EMC 3:7 vs 1:1 by wt.). Less EC-containing electrolyte (denoted as BL1) yielded better cycling performance which is in agreement with other studies conducted by Dahn's group about the performance of EC-free carbonate-based electrolytes.[215,216] ICP-MS analysis and XPS confirmed the participation of TPPO in formation of AEI and CEI, indicating the reduction and oxidation of the electrolyte additive prior to the electrolyte solvent, further verified by shifting of the electrolyte reduction onset potential to higher values in CV diagram, and increased amount of $LiPO_xF_z$ compounds and alkyl carbonates

Table 1. Discharge capacity and coulombic efficiency at 1st, 5th, and 100th cycles as well as capacity retention after 100 cycles for NCM811/graphite cell excluding/including different electrolyte additives, namely, TPPO, TPP, VC, and DPC; BL 1 (= 1 M $LiPF_6$, EC/EMC 3:7 by wt.).[214]

Electrolyte	Discharge capacity [mAh g^{-1}]			Coulombic efficiency [%]			Capacity retention
	1st cycle	5th cycle	100th cycle	1st cycle	5th cycle	100th cycle	100th/3rd [%]
BL 1	163	156	135	70.5	99.4	99.9	86
BL 1 + 0.5 wt% TPPO	198	187	172	86.2	99.8	99.9	92
BL 1 + 0.5 wt% TPP	200	189	165	84.3	99.5	99.8	87
BL 1 + 0.5 wt% VC	189	181	158	82.3	99.4	99.9	86
BL 1 + 0.5 wt% DPC	160	152	123	69.4	99.3	99.8	80

in CEI layer. It is worth mentioning that AEI layer in the TPPO-free electrolyte primarily consists of organic and carbon/metal species, which is in agreement with the reported increased loss of active lithium, while the one with TPPO mainly contains inorganic compounds probably from decomposition of conductive salt species. In fact, TPPO-induced SEI layer is an efficient Li-conducting and electronically insulating layer with the ability of impeding parasitic electrode-electrolyte side reactions. Figure 16c compares the long-term cycling performance of the cells with TPPO-included/excluded electrolytes. Addition of TPPO can significantly increase the initial CE and improve capacity retention, i.e., above 80% state of health (SOH) after 295 cycles and around 77% after 350 cyles. Moreover, the electrochemical effectivity of TPPO compared to varoius promising electrolyte additives, i.e., TPP, VC and DPC, is tested (Figure 16d). According to the results (presented in **Table 1**) the cell with TPPO-containing electrolyte delivers the best discharge capacity, initial and average CE, and cycling stability.

In general, preeminent influence of electrolyte composition on cycling, rate, safety and overall electrochemical performance of LIBs is indisputable. Employing electrolyte additives has shown significant promises regarding the enhancement of electrolyte properties. Nonetheless, the efficiency of additives tightly depends on the cathode material type and composition. In this regard, more comprehensive and systematic studies are required to investigate the function of various additives with different concentration and their interaction with one-of-a-kind NCM811 upon cycling. Besides, to accurately scrutinize the complicated mechanism of this interaction at the cathode–electrolyte interface, employing more state-of-the-art in situ techniques as well as quantitative methods are required in future studies.

4. Outline and Conclusions

Among the potential candidates for cathode material in near-future LIBs, nickel-rich NCM811 is the most auspicious one regarding its discernible advantages, namely high energy density and discharge capacity. Nonetheless, it suffers from unsatisfactory cyclability, thermal stability and rate capability in its pristine state, particularly during cycling at elevated voltages. Accordingly, many researches have been conducted to address these downsides and further resolve them. The origins of these drawbacks and effective strategies for overcoming them have been thoroughly discussed in this review. Notably, all the chemical, structural, and electrochemical degradation from bulk to surface of the cathode material are by some means in relationship with the cathode–electrolyte interface. In other words, the robustness and integrity of this area through cycling insures the efficacy of the whole cell.

Thus far, various coating strategies (namely, electrochemically inactive coating, Li-reactive/Li-ion conductive coating, and conducting-polymer coating) along with other surface treatments (such as pre-cycling, employing surface stabilizers, and forming artificial CEI layers, etc.) as well as structural modification (primarily designing concentration-gradient structure or doping extrinsic ions into the cathode structure) and electrolyte enhancement methods have been studied to elevate the performance of NCM811 and mitigate its shortcomings. Although many of these approaches have imperative effects on stability of the cell performance upon cycling even at high cutoff voltages, they can hardly address all the problems at once. For example, by employing an appropriate Li-reactive/conductive coating, safety properties and rate capability substantially improves due to consuming of surface lithium residues by coating materials and lowering the interfacial impedance by facilitating Li^+ transportation, respectively. However, anisotropic volume changes at highly delithiated states during continuous cycling leads to mechanical degradation of the cathode material and further capacity fading.

Therefore, we believe that in order to design an excellent cathode–electrolyte interface and concurrently deal with all the issues of NCM811 at once, employing a multiapproach strategy is essential. Simultaneous adoption of surface modification strategies, such as lithium-conductive/reactive coating to mitigate TMs dissolution, parasitic side reactions, interfacial impedance and polarization gap, together with concentration-gradient structure to alleviate cation mixing, phase transition and lattice distortion seem to be a promising direction for future studies. Indeed, employing TSFCG structure to impede the microcrack generation and mechanical degradation concurrent with multications doping at different sites to increase the structural/interfacial stability along with a modified electrolyte to diminish the electrolyte decomposition is another perspective. To benefit from both coating and doping and ultimately boost the electrochemical performance of the entire cells, the surface doping method is another efficient approach which needs to be further investigated.

Although the marketable LIBs cannot entirely address the ever-growing requisites of the market, the advancement and progress of LIBs' cathode materials with superior capacity and energy density is inevitable; higher Ni (more than 80%)-containing layered NCMs and Li-rich Mn-based layered oxide

(LMR) cathode materials are among them. Despite their major shortcomings, which are poor cycling performance for the former and fast voltage decaying for the latter, they can be considered among the best candidates for the future cathode materials in LIBs due to their high energy density. Hence, studying their interface, chemical/structural properties, reaction mechanism in detail and even making a comparison between their properties and electrochemical performances after employing different modification approaches is an appropriate direction. As a result, the combination of LMR and Ni-rich layered cathode materials in order to reach a single efficient composite cathode with superior electrochemical properties is another perspective that can be further explored. Having enough knowledge about the exact mechanism of effect for each method and material is the key feature to fulfil this goal. Thus, further in-depth exploration into the cathode–electrolyte interfacial reactions using meticulous in situ microscopic characterization techniques is indispensable.

Acknowledgements

This research was supported by the National Key R&D Program of China (2018YFB0105900).

Conflict of Interest

The authors declare no conflict of interest.

Keywords

degradation mechanism, interface, modification strategies, NCM811

Received: May 16, 2019
Revised: July 5, 2019
Published online:

[1] N. S. Choi, Z. Chen, S. A. Freunberger, X. Ji, Y. K. Sun, K. Amine, G. Yushin, L. F. Nazar, J. Cho, P. G. Bruce, *Angew. Chem., Int. Ed.* **2012**, *51*, 9994.
[2] T. H. Kim, J. S. Park, S. K. Chang, S. Choi, J. H. Ryu, H. K. Song, *Adv. Energy Mater.* **2012**, *2*, 860.
[3] D. Aurbach, B. Markovsky, G. Salitra, E. Markevich, Y. Talyossef, M. Koltypin, L. Nazar, B. Ellis, D. Kovacheva, *J. Power Sources* **2007**, *165*, 491.
[4] P.-C. Chen, J. Xu, H. Chen, C. Zhou, *Nano Res.* **2011**, *4*, 290.
[5] C.-H. Yim, F. M. Courtel, Y. Abu-Lebdeh, *J. Mater. Chem. A* **2013**, *1*, 8234.
[6] J. Lu, Z. Chen, F. Pan, Y. Cui, K. Amine, *Electrochem. Energy Rev.* **2018**, *1*, 35.
[7] F. Dou, L. Shi, G. Chen, D. Zhang, *Electrochem. Energy Rev.* **2019**, *2*, 149.
[8] T. Ohzuku, A. Ueda, *J. Electrochem. Soc.* **1994**, *141*, 2972.
[9] Y. Shao-Horn, L. Croguennec, C. Delmas, E. C. Nelson, M. O'Keefe, *Nat. Mater.* **2003**, *2*, 464.
[10] A. K. Padhi, K. S. Nanjundaswamy, J. B. Goodenough, *J. Electrochem. Soc.* **1997**, *144*, 1188.
[11] B. Kang, G. Ceder, *Nature* **2009**, *458*, 190.
[12] S.-Y. Chung, J. T. Bloking, Y.-M. Chiang, *Nat. Mater.* **2002**, *1*, 123.
[13] L. Gu, C. Zhu, H. Li, Y. Yu, C. Li, S. Tsukimoto, J. Maier, Y. Ikuhara, *J. Am. Chem. Soc.* **2011**, *133*, 4661.
[14] B. L. Ellis, K. T. Lee, L. F. Nazar, *Chem. Mater.* **2010**, *22*, 691.
[15] J. Wang, X. Sun, *Energy Environ. Sci.* **2015**, *8*, 1110.
[16] Y. Xia, M. Yoshio, *J. Electrochem. Soc.* **1996**, *143*, 825.
[17] Y.-K. Sun, S.-T. Myung, B.-C. Park, J. Prakash, I. Belharouak, K. Amine, *Nat. Mater.* **2009**, *8*, 320.
[18] B. Scrosati, J. Garche, *J. Power Sources* **2010**, *195*, 2419.
[19] A. Manthiram, B. Song, W. Li, *Energy Storage Mater.* **2017**, *6*, 125.
[20] W. Liu, P. Oh, X. Liu, M. J. Lee, W. Cho, S. Chae, Y. Kim, J. Cho, *Angew. Chem., Int. Ed.* **2015**, *54*, 4440.
[21] Y. Ding, Z. P. Cano, A. Yu, J. Lu, Z. Chen, *Electrochem. Energy Rev.* **2019**, *2*, 1.
[22] S. Watanabe, M. Kinoshita, T. Hosokawa, K. Morigaki, K. Nakura, *J. Power Sources* **2014**, *258*, 210.
[23] D. J. Miller, C. Proff, J. Wen, D. P. Abraham, J. Bareño, *Adv. Energy Mater.* **2013**, *3*, 1098.
[24] S.-T. Myung, F. Maglia, K.-J. Park, C. S. Yoon, P. Lamp, S.-J. Kim, Y.-K. Sun, *ACS Energy Lett.* **2017**, *2*, 196.
[25] Y. Ding, D. Mu, B. Wu, R. Wang, Z. Zhao, F. Wu, *Appl. Energy* **2017**, *195*, 586.
[26] H.-H. Ryu, K.-J. Park, C. S. Yoon, Y.-K. Sun, *Chem. Mater.* **2018**, *30*, 1155.
[27] H.-J. Noh, S. Youn, C. S. Yoon, Y.-K. Sun, *J. Power Sources* **2013**, *233*, 121.
[28] J. Kim, H. Lee, H. Cha, M. Yoon, M. Park, J. Cho, *Adv. Energy Mater.* **2018**, *8*, 1702028.
[29] F. Schipper, H. Bouzaglo, M. Dixit, E. M. Erickson, T. Weigel, M. Talianker, J. Grinblat, L. Burstein, M. Schmidt, J. Lampert, C. Erk, B. Markovsky, D. T. Major, D. Aurbach, *Adv. Energy Mater.* **2018**, *8*, 1701682.
[30] J. D. Steiner, L. Mu, J. Walsh, M. M. Rahman, B. Zydlewski, F. M. Michel, H. L. Xing, D. Nordlund, F. Lin, *ACS Appl. Mater. Interfaces* **2018**, *10*, 23842.
[31] K. Min, E. Cho, *Phys. Chem. Chem. Phys.* **2018**, *20*, 9045.
[32] Q. Lin, W. Guan, J. Meng, W. Huang, X. Wei, Y. Zeng, J. Li, Z. Zhang, *Nano Energy* **2018**, *54*, 313.
[33] J. Kasnatscheew, R. Wagner, M. Winter, I. Cekic-Laskovic, *Top. Curr. Chem.* **2018**, *376*, 23.
[34] B. Wu, W. Lu, *J. Phys. Chem. C* **2017**, *121*, 19022.
[35] H. Sun, K. Zhao, *J. Phys. Chem. C* **2017**, *121*, 6002.
[36] A. O. Kondrakov, A. Schmidt, J. Xu, H. Gesswein, R. Moenig, P. Hartmann, H. Sommer, T. Brezesinski, J. Janek, *J. Phys. Chem. C* **2017**, *121*, 3286.
[37] P. Hou, J. Yin, M. Ding, J. Huang, X. Xu, *Small* **2017**, *13*, 1701802.
[38] S.-M. Bak, E. Hu, Y. Zhou, X. Yu, S. D. Senanayake, S.-J. Cho, K.-B. Kim, K. Y. Chung, X.-Q. Yang, K.-W. Nam, *ACS Appl. Mater. Interfaces* **2014**, *6*, 22594.
[39] Y.-D. Xu, W. Xiang, Z.-G. Wu, C.-L. Xu, Y.-C. Li, X.-D. Guo, G.-P. Lv, X. Peng, B.-H. Zhong, *Electrochim. Acta* **2018**, *268*, 358.
[40] J. Xie, A. D. Sendek, E. D. Cubuk, X. Zhang, Z. Lu, Y. Gong, T. Wu, F. Shi, W. Liu, E. J. Reed, Y. Cui, *ACS Nano* **2017**, *11*, 7019.
[41] S. Chen, T. He, Y. Su, Y. Lu, L. Bao, L. Chen, Q. Zhang, J. Wang, R. Chen, F. Wu, *ACS Appl. Mater. Interfaces* **2017**, *9*, 29732.
[42] E. Zhao, M. Chen, Z. Hu, X. Xiao, D. Chen, *Electrochim. Acta* **2016**, *208*, 64.
[43] L. Li, M. Xu, Q. Yao, Z. Chen, L. Song, Z. Zhang, C. Gao, P. Wang, Z. Yu, Y. Lai, *ACS Appl. Mater. Interfaces* **2016**, *8*, 30879.
[44] Y. Wu, T. Cao, R. Wang, F. Meng, J. Zhang, C. Cao, *J. Mater. Chem. A* **2018**, *6*, 8374.
[45] Y. Su, G. Chen, L. Chen, W. Li, Q. Zhang, Z. Yang, Y. Lu, L. Bao, J. Tan, R. Chen, S. Chen, F. Wu, *ACS Appl. Mater. Interfaces* **2018**, *10*, 6407.

[46] X. Xiong, Z. Wang, P. Yue, H. Guo, F. Wu, J. Wang, X. Li, *J. Power Sources* **2013**, *222*, 318.
[47] K. Min, S.-W. Seo, Y. Y. Song, H. S. Lee, E. Cho, *Phys. Chem. Chem. Phys.* **2017**, *19*, 1762.
[48] H. Zhang, H. Zhao, M. A. Khan, W. Zou, J. Xu, L. Zhang, J. Zhang, *J. Mater. Chem. A* **2018**, *6*, 20564.
[49] F. Schipper, E. M. Erickson, C. Erk, J.-Y. Shin, F. F. Chesneau, D. Aurbach, *J. Electrochem. Soc.* **2017**, *164*, A6220.
[50] Y. Ding, R. Wang, L. Wang, K. Cheng, Z. Zhao, D. Mu, B. Wu, *Energy Procedia* **2017**, *105*, 2941.
[51] Z. Chen, D. Chao, J. Lin, Z. Shen, *Mater. Res. Bull.* **2017**, *96*, 491.
[52] F. Schipper, D. Aurbach, *Russ. J. Electrochem.* **2016**, *52*, 1095.
[53] A. Manthiram, J. C. Knight, S. T. Myung, S. M. Oh, Y. K. Sun, *Adv. Energy Mater.* **2016**, *6*, 1501010.
[54] D.-H. Seo, J. Lee, A. Urban, R. Malik, S. Kang, G. Ceder, *Nat. Chem.* **2016**, *8*, 692.
[55] F. Lin, I. M. Markus, D. Nordlund, T.-C. Weng, M. D. Asta, H. L. Xin, M. M. Doeff, *Nat. Commun.* **2014**, *5*, 3529.
[56] P. Yan, J. Zheng, M. Gu, J. Xiao, J.-G. Zhang, C.-M. Wang, *Nat. Commun.* **2017**, *8*, 14101.
[57] L. Wu, N. Kyung-Wan, X. Wang, Y. Zhou, J.-C. Zheng, X.-Q. Yang, Y. Zhu, *Chem. Mater.* **2011**, *23*, 3953.
[58] A. Manthiram, A. V. Murugan, A. Sarkar, T. Muraliganth, *Energy Environ. Sci.* **2008**, *1*, 621.
[59] P. Hou, G. Li, X. Gao, *J. Mater. Chem. A* **2016**, *4*, 7689.
[60] A. O. Kondrakov, H. Gesswein, K. Galdina, L. de Biasi, V. Meded, E. O. Filatova, G. Schumacher, W. Wenzel, P. Hartmann, T. Brezesinski, J. Janek, *J. Phys. Chem. C* **2017**, *121*, 24381.
[61] M. Dixit, B. Markovsky, F. Schipper, D. Aurbach, D. T. Major, *J. Phys. Chem. C* **2017**, *121*, 22628.
[62] C. Masquelier, L. Croguennec, *Chem. Rev.* **2013**, *113*, 6552.
[63] Y. S. Meng, M. E. Arroyo-de Dompablo, *Acc. Chem. Res.* **2013**, *46*, 1171.
[64] K.-W. Nam, S.-M. Bak, E. Hu, X. Yu, Y. Zhou, X. Wang, L. Wu, Y. Zhu, K.-Y. Chung, X.-Q. Yang, *Adv. Funct. Mater.* **2013**, *23*, 1047.
[65] G. Cherkashinin, M. Motzko, N. Schulz, T. Späth, W. Jaegermann, *Chem. Mater.* **2015**, *27*, 2875.
[66] S. Maintz, V. L. Deringer, A. L. Tchougréeff, R. Dronskowski, *J. Comput. Chem.* **2013**, *34*, 2557.
[67] J. B. Goodenough, K.-S. Park, *J. Am. Chem. Soc.* **2013**, *135*, 1167.
[68] C. M. Julien, A. Mauger, K. Zaghib, H. Groult, *Inorganics* **2014**, *2*, 132.
[69] S. Hwang, S. M. Kim, S.-M. Bak, B.-W. Cho, K. Y. Chung, J. Y. Lee, W. Chang, E. A. Stach, *ACS Appl. Mater. Interfaces* **2014**, *6*, 15140.
[70] J. Yang, Y. Xia, *ACS Appl. Mater. Interfaces* **2016**, *8*, 1297.
[71] J. Xiao, N. A. Chernova, M. S. Whittingham, *Chem. Mater.* **2008**, *20*, 7454.
[72] W. Qiu, J. Xia, L. Chen, J. R. Dahn, *J. Power Sources* **2016**, *318*, 228.
[73] S. K. Jung, H. Gwon, J. Hong, K. Y. Park, D. H. Seo, H. Kim, J. Hyun, W. Yang, K. Kang, *Adv. Energy Mater.* **2014**, *4*, 1300787.
[74] M. Gu, I. Belharouak, J. Zheng, H. Wu, J. Xiao, A. Genc, K. Amine, S. Thevuthasan, D. R. Baer, J.-G. Zhang, *ACS Nano* **2013**, *7*, 760.
[75] C. Pouillerie, F. Perton, P. Biensan, J. Peres, M. Broussely, C. Delmas, *J. Power Sources* **2001**, *96*, 293.
[76] C.-C. Chang, J. Y. Kim, P. N. Kumta, *J. Power Sources* **2000**, *89*, 56.
[77] J. Reed, G. Ceder, *Chem. Rev.* **2004**, *104*, 4513.
[78] D. Qian, B. Xu, M. Chi, Y. S. Meng, *Phys. Chem. Chem. Phys.* **2014**, *16*, 14665.
[79] C. S. Yoon, D.-W. Jun, S.-T. Myung, Y.-K. Sun, *ACS Energy Lett.* **2017**, *2*, 1150.
[80] K. Min, K. Kim, C. Jung, S.-W. Seo, Y. Y. Song, H. S. Lee, J. Shin, E. Cho, *J. Power Sources* **2016**, *315*, 111.
[81] K. Ishidzu, Y. Oka, T. Nakamura, *Solid State Ionics* **2016**, *288*, 176.
[82] S.-G. Woo, J.-H. Kim, H.-R. Kim, W. Cho, J.-S. Yu, *J. Electroanal. Chem.* **2017**, *799*, 315.
[83] H.-R. Kim, S.-G. Woo, J.-H. Kim, W. Cho, Y.-J. Kim, *J. Electroanal. Chem.* **2016**, *782*, 168.
[84] J. Li, L. E. Downie, L. Ma, W. Qiu, J. R. Dahn, *J. Electrochem. Soc.* **2015**, *162*, A1401.
[85] Y.-k. Ahn, Y. N. Jo, W. Cho, J.-S. Yu, K. J. Kim, *Energies* **2019**, *12*, 1.
[86] U.-H. Kim, E.-J. Lee, C. S. Yoon, S.-T. Myung, Y.-K. Sun, *Adv. Energy Mater.* **2016**, *6*, 1601417.
[87] H.-H. Sun, A. Manthiram, *Chem. Mater.* **2017**, *29*, 8486.
[88] A. Mukhopadhyay, B. W. Sheldon, *Prog. Mater. Sci.* **2014**, *63*, 58.
[89] C. Ghanty, B. Markovsky, E. M. Erickson, M. Talianker, O. Haik, Y. Tal-Yossef, A. Mor, D. Aurbach, J. Lampert, A. Volkov, *ChemElectroChem* **2015**, *2*, 1479.
[90] Y. Tsai, B. Hwang, G. Ceder, H. Sheu, D. Liu, J. Lee, *Chem. Mater.* **2005**, *17*, 3191.
[91] D.-H. Seo, A. Urban, G. Ceder, *Phys. Rev. B* **2015**, *92*, 115118.
[92] A. Van der Ven, M. Aydinol, G. Ceder, G. Kresse, J. Hafner, *Phys. Rev. B* **1998**, *58*, 2975.
[93] Y.-N. Zhou, J. Ma, E. Hu, X. Yu, L. Gu, K.-W. Nam, L. Chen, Z. Wang, X.-Q. Yang, *Nat. Commun.* **2014**, *5*, 5381.
[94] O. Dolotko, A. Senyshyn, M. Mühlbauer, K. Nikolowski, H. Ehrenberg, *J. Power Sources* **2014**, *255*, 197.
[95] H.-J. Noh, Z. Chen, C. S. Yoon, J. Lu, K. Amine, Y.-K. Sun, *Chem. Mater.* **2013**, *25*, 2109.
[96] R. Kostecki, J. Lei, F. McLarnon, J. Shim, K. Striebel, *J. Electrochem. Soc.* **2006**, *1533*, A669.
[97] H. Kim, S. Lee, H. Cho, J. Kim, J. Lee, S. Park, S. H. Joo, S. H. Kim, Y.-G. Cho, H.-K. Song, S. K. Kwak, J. Cho, *Adv. Mater.* **2016**, *28*, 4705.
[98] B.-J. Chae, T. Yim, *J. Power Sources* **2017**, *360*, 480.
[99] M. Gauthier, T. J. Carney, A. Grimaud, L. Giordano, N. Pour, H.-H. Chang, D. P. Fenning, S. F. Lux, O. Paschos, C. Bauer, *J. Phys. Chem. Lett.* **2015**, *6*, 4653.
[100] F. Yu, Z. Yuan, T. Yang, B. Qian, *Phys. Chem. Chem. Phys.* **2018**, *20*, 19195.
[101] F. Lin, D. Nordlund, I. M. Markus, T.-C. Weng, H. L. Xin, M. M. Doeff, *Energy Environ. Sci.* **2014**, *7*, 3077.
[102] W. Li, A. Dolocan, P. Oh, H. Celio, S. Park, J. Cho, A. Manthiram, *Nat. Commun.* **2017**, *8*, 14589.
[103] Y. Kim, *J. Mater. Sci.: Mater. Electron.* **2013**, *48*, 8547.
[104] D.-W. Jun, C. S. Yoon, U.-H. Kim, Y.-K. Sun, *Chem. Mater.* **2017**, *29*, 5048.
[105] U.-H. Kim, S.-T. Myung, C. S. Yoon, Y.-K. Sun, *ACS Energy Lett.* **2017**, *2*, 1848.
[106] T. Ohzuku, A. Ueda, M. Nagayama, Y. Iwakoshi, H. Komori, *Electrochim. Acta* **1993**, *38*, 1159.
[107] D.-H. Cho, C.-H. Jo, W. Cho, Y.-J. Kim, H. Yashiro, Y.-K. Sun, S.-T. Myung, *J. Electrochem. Soc.* **2014**, *161*, A920.
[108] K. Xu, *Chem. Rev.* **2014**, *114*, 11503.
[109] R. Jung, M. Metzger, F. Maglia, C. Stinner, H. A. Gasteiger, *J. Phys. Chem. Lett.* **2017**, *8*, 4820.
[110] S.-T. Myung, K. Amine, Y.-K. Sun, *J. Mater. Chem.* **2010**, *20*, 7074.
[111] Z. Chen, Y. Qin, K. Amine, Y.-K. Sun, *J. Mater. Chem.* **2010**, *20*, 7606.
[112] Y.-K. Sun, Y.-S. Lee, M. Yoshio, K. Amine, *Electrochem. Solid-State Lett.* **2002**, *5*, A99.
[113] S.-T. Myung, K. Izumi, S. Komaba, Y.-K. Sun, H. Yashiro, N. Kumagai, *Chem. Mater.* **2005**, *17*, 3695.
[114] S.-U. Woo, C. Yoon, K. Amine, I. Belharouak, Y.-K. Sun, *J. Electrochem. Soc.* **2007**, *154*, A1005.
[115] M. Dong, Z. Wang, H. Li, H. Guo, X. Li, K. Shih, J. Wang, *ACS Sustainable Chem. Eng.* **2017**, *5*, 10199.
[116] B. Han, B. Key, S. H. Lapidus, J. C. Garcia, H. Iddir, J. T. Vaughey, F. Dogan, *ACS Appl. Mater. Interfaces* **2017**, *9*, 41291.
[117] F. Dogan, J. T. Vaughey, H. Iddir, B. Key, *ACS Appl. Mater. Interfaces* **2016**, *8*, 16708.

[118] B. Han, T. Paulauskas, B. Key, C. Peebles, J. S. Park, R. F. Klie, J. T. Vaughey, F. Dogan, *ACS Appl. Mater. Interfaces* **2017**, *9*, 14769.
[119] S.-G. Woo, J.-H. Han, K. J. Kim, J.-H. Kim, J.-S. Yu, Y.-J. Kim, *Electrochim. Acta* **2015**, *153*, 115.
[120] X. Li, K. Zhang, M. Wang, Y. Liu, M. Qu, W. Zhao, J. Zheng, *Sustainable Energy Fuels* **2018**, *2*, 413.
[121] L. Liang, G. Hu, F. Jiang, Y. Cao, *J. Alloys Compd.* **2016**, *657*, 570.
[122] S. Dai, M. Yuan, L. Wang, L. Luo, Q. Chen, T. Xie, Y. Li, Y. Yang, *Ceram. Int.* **2019**, *45*, 674.
[123] S. H. Kang, Y. N. Jo, K. Prasanna, T. H. Kim, S. J. Do, P. Santhoshkumar, I. N. Sivagami, C. W. Lee, *J. Nanosci. Nanotechnol.* **2017**, *17*, 8093.
[124] J. Cho, T.-J. Kim, J. Kim, M. Noh, B. Park, *J. Electrochem. Soc.* **2004**, *151*, A1899.
[125] J. Cho, H. Kim, B. Park, *J. Electrochem. Soc.* **2004**, *151*, A1707.
[126] G.-R. Hu, X.-R. Deng, Z.-D. Peng, K. Du, *Electrochim. Acta* **2008**, *533*, 2567.
[127] X. Xiong, Z. Wang, X. Yin, H. Guo, X. Li, *Mater. Lett.* **2013**, *110*, 4.
[128] X. Xiong, Z. Wang, G. Yan, H. Guo, X. Li, *J. Power Sources* **2014**, *245*, 183.
[129] X. Xiong, Z. Wang, H. Guo, Q. Zhang, X. Li, *J. Mater. Chem. A* **2013**, *1*, 1284.
[130] Y. Xu, L. Xie, Y. Zhang, X. Cao, *Electron. Mater. Lett.* **2013**, *9*, 693.
[131] L. Q. Mai, B. Hu, W. Chen, Y. Qi, C. Lao, R. Yang, Y. Dai, Z. L. Wang, *Adv. Mater.* **2007**, *19*, 3712.
[132] F. Wu, J. Tian, Y. Su, Y. Guan, Y. Jin, Z. Wang, T. He, L. Bao, S. Chen, *J. Power Sources* **2014**, *269*, 747.
[133] H. Konishi, M. Yoshikawa, T. Hirano, *J. Power Sources* **2013**, *244*, 23.
[134] Y. Zhang, Z.-B. Wang, F.-D. Yu, L.-F. Que, M.-J. Wang, Y.-F. Xia, Y. Xue, J. Wu, *J. Power Sources* **2017**, *358*, 1.
[135] J. Huang, X. Fang, Y. Wu, L. Zhou, Y. Wang, Y. Jin, W. Dang, L. Wu, Z. Rong, X. Chen, X. Tang, *J. Electroanal. Chem.* **2018**, *823*, 359.
[136] K. Meng, Z. Wang, H. Guo, X. Li, D. Wang, *Electrochim. Acta* **2016**, *211*, 822.
[137] Z. Xiao, C. Hu, L. Song, L. Li, Z. Cao, H. Zhu, J. Liu, X. Li, F. Tang, *Ionics* **2018**, *24*, 91.
[138] W. D. Richards, L. J. Miara, Y. Wang, J. C. Kim, G. Ceder, *Chem. Mater.* **2016**, *28*, 266.
[139] H. G. Song, J. Y. Kim, K. T. Kim, Y. J. Park, *J. Power Sources* **2011**, *196*, 6847.
[140] J. Zhu, Y. Li, L. Xue, Y. Chen, T. Lei, S. Deng, G. Cao, *J. Alloys Compd.* **2019**, *773*, 112.
[141] M. Wang, R. Zhang, Y. Gong, Y. Su, D. Xiang, L. Chen, Y. Chen, M. Luo, M. Chu, *Solid State Ionics* **2017**, *312*, 53.
[142] K. Hu, X. Qi, C. Lu, K. Du, Z. Peng, Y. Cao, G. Hu, *Ceram. Int.* **2018**, *44*, 14209.
[143] Y. J. Lim, S.-M. Lee, H. Lim, B. Moon, K.-S. Han, J.-H. Kim, J.-H. Song, J.-S. Yu, W. Cho, M.-S. Park, *Electrochim. Acta* **2018**, *282*, 311.
[144] H. Liang, Z. Wang, H. Guo, J. Wang, J. Leng, *Appl. Surf. Sci.* **2017**, *423*, 1045.
[145] E. Zhao, M. Chen, Z. Hu, D. Chen, L. Yang, X. Xiao, *J. Power Sources* **2017**, *343*, 345.
[146] B. Zhang, P. Dong, H. Tong, Y. Yao, J. Zheng, W. Yu, J. Zhang, D. Chu, *J. Alloys Compd.* **2017**, *706*, 198.
[147] Y.-C. Li, W.-M. Zhao, W. Xiang, Z.-G. Wu, Z.-G. Yang, C.-L. Xu, Y.-D. Xu, E.-H. Wang, C.-J. Wu, X.-D. Guo, *J. Alloys Compd.* **2018**, *766*, 546.
[148] H. M. Xie, R. S. Wang, J. R. Ying, L. Y. Zhang, A. F. Jalbout, H. Y. Yu, G. L. Yang, X. M. Pan, Z. M. Su, *Adv. Mater.* **2006**, *18*, 2609.
[149] S. H. Ju, I.-S. Kang, Y.-S. Lee, W.-K. Shin, S. Kim, K. Shin, D.-W. Kim, *ACS Appl. Mater. Interfaces* **2014**, *6*, 2546.
[150] L.-J. Her, J.-L. Hong, C.-C. Chang, *J. Power Sources* **2006**, *157*, 457.
[151] D. Wang, X. Wang, X. Yang, R. Yu, L. Ge, H. Shu, *J. Power Sources* **2015**, *293*, 89.
[152] X. Xiong, D. Ding, Z. Wang, B. Huang, H. Guo, X. Li, *J. Solid State Electrochem.* **2014**, *18*, 2619.
[153] M. Zhao, X. Wu, C. Cai, *J. Phys. Chem. C* **2009**, *113*, 4987.
[154] K. S. Park, S. B. Schougaard, J. B. Goodenough, *Adv. Mater.* **2007**, *19*, 848.
[155] L. Song, F. Tang, Z. Xiao, Z. Cao, H. Zhu, A. Li, *J. Electron. Mater.* **2018**, *47*, 5896.
[156] Y. Cao, X. Qi, K. Hu, Y. Wang, Z. Gan, Y. Li, G. Hu, Z. Peng, K. Du, *ACS Appl. Mater. Interfaces* **2018**, *10*, 18270.
[157] S. S. Jan, S. Nurgul, X. Shi, H. Xia, H. Pang, *Electrochim. Acta* **2014**, *149*, 86.
[158] J. Kim, H. Ma, H. Cha, H. Lee, J. Sung, M. Seo, P. Oh, M. Park, J. Cho, *Energy Environ. Sci.* **2018**, *11*, 1449.
[159] Z. Tang, H. Zheng, F. Qian, Y. Ma, C. Zhao, L. Song, Y. Chen, X. Xiong, X. Zhu, C. Mi, *Ionics* **2018**, *24*, 61.
[160] J. Yang, Y. Xia, *J. Electrochem. Soc.* **2016**, *163*, A2665.
[161] B.-J. Chae, T. Yim, *Mater. Chem. Phys.* **2018**, *214*, 66.
[162] B.-J. Chae, J. H. Park, H. J. Song, S. H. Jang, K. Jung, Y. D. Park, T. Yim, *Electrochim. Acta* **2018**, *290*, 465.
[163] P. Li, S. Zhao, Y. Zhuang, J. Adkins, Q. Zhou, J. Zheng, *Appl. Surf. Sci.* **2018**, *453*, 93.
[164] Y.-K. Sun, B.-R. Lee, H.-J. Noh, H. Wu, S.-T. Myung, K. Amine, *J. Mater. Chem.* **2011**, *21*, 10108.
[165] X. Chen, X. Jia, Y. Qu, D. Li, D. Chen, Y. Chen, *New J. Chem.* **2018**, *42*, 5868.
[166] Y.-K. Sun, S.-T. Myung, M.-H. Kim, J. Prakash, K. Amine, *J. Am. Chem. Soc.* **2005**, *127*, 13411.
[167] Y.-K. Sun, S.-T. Myung, H.-S. Shin, Y. C. Bae, C. S. Yoon, *J. Phys. Chem. B* **2006**, *110*, 6810.
[168] Y.-K. Sun, S.-T. Myung, M.-H. Kim, J.-H. Kim, *Electrochem. Solid-State Lett.* **2006**, *9*, A171.
[169] Y.-K. Sun, S.-T. Myung, B.-C. Park, K. Amine, *Chem. Mater.* **2006**, *18*, 5159.
[170] H. Shi, X. Wang, P. Hou, E. Zhou, J. Guo, J. Zhang, D. Wang, F. Guo, D. Song, X. Shi, L. Zhang, *J. Alloys Compd.* **2014**, *587*, 710.
[171] Q. Li, R. Dang, M. Chen, Y. Lee, Z. Hu, X. Xiao, *ACS Appl. Mater. Interfaces* **2018**, *10*, 17850.
[172] X. Lu, X. Li, Z. Wang, H. Guo, G. Yan, X. Yin, *Appl. Surf. Sci.* **2014**, *297*, 182.
[173] J.-Y. Liao, A. Manthiram, *J. Power Sources* **2015**, *282*, 429.
[174] Y.-K. Sun, Z. Chen, H.-J. Noh, D.-J. Lee, H.-G. Jung, Y. Ren, S. Wang, C. S. Yoon, S.-T. Myung, K. Amine, *Nat. Mater.* **2012**, *11*, 942.
[175] C. Hua, K. Du, C. Tan, Z. Peng, Y. Cao, G. Hu, *J. Alloys Compd.* **2014**, *614*, 264.
[176] K.-J. Park, B.-B. Lim, M.-H. Choi, H.-G. Jung, Y.-K. Sun, M. Haro, N. Vicente, J. Bisquert, G. Garcia-Belmonte, *J. Mater. Chem. A* **2015**, *3*, 22183.
[177] B.-B. Lim, S.-T. Myung, C. S. Yoon, Y.-K. Sun, *ACS Energy Lett.* **2016**, *1*, 283.
[178] F. Kong, C. Liang, R. C. Longo, D.-H. Yeon, Y. Zheng, J.-H. Park, S.-G. Doo, K. Cho, *Chem. Mater.* **2016**, *28*, 6942.
[179] B. Zhang, L. Li, J. Zheng, *J. Alloys Compd.* **2012**, *520*, 190.
[180] C. Liang, F. Kong, R. C. Longo, C. Zhang, Y. Nie, Y. Zheng, K. Cho, *J. Mater. Chem. A* **2017**, *5*, 25303.
[181] S. W. Woo, S. T. Myung, H. Bang, D. W. Kim, Y. K. Sun, *Electrochim. Acta* **2009**, *54*, 3851.
[182] T. He, Y. Lu, Y. Su, L. Bao, J. Tan, L. Chen, Q. Zhang, W. Li, S. Chen, F. Wu, *ChemSusChem* **2018**, *11*, 1639.
[183] K. Kang, Y. S. Meng, J. Bréger, C. P. Grey, G. Ceder, *Science* **2006**, *311*, 977.
[184] D. Wang, X. Li, Z. Wang, H. Guo, Y. Xu, Y. Fan, J. Ru, *Electrochim. Acta* **2016**, *188*, 48.

[185] J. Li, Y. Li, Y. Guo, J. Lv, W. Yi, P. Ma, *J. Mater. Sci.: Mater. Electron.* **2018**, *29*, 10702.
[186] S.-U. Woo, B.-C. Park, C. Yoon, S.-T. Myung, J. Prakash, Y.-K. Sun, *J. Electrochem. Soc.* **2007**, *154*, A649.
[187] P. Yue, Z. Wang, J. Wang, H. Guo, X. Xiong, X. Li, *Powder Technol.* **2013**, *237*, 623.
[188] P. Yue, Z. Wang, H. Guo, X. Xiong, X. Li, *Electrochim. Acta* **2013**, *92*, 1.
[189] R. Du, Y. Bi, W. Yang, Z. Peng, M. Liu, Y. Liu, B. Wu, B. Yang, F. Ding, D. Wang, *Ceram. Int.* **2015**, *41*, 7133.
[190] S. Gao, X. Zhan, Y.-T. Cheng, *J. Power Sources* **2019**, *410–411*, 45.
[191] B. Han, S. Xu, S. Zhao, G. Lin, Y. Peng, L. Chen, D. G. Ivey, P. Wang, W. Wei, *ACS Appl. Mater. Interfaces* **2018**, *10*, 39599.
[192] M. Chen, E. Zhao, D. Chen, M. Wu, S. Han, Q. Huang, L. Yang, X. Xiao, Z. Hu, *Inorg. Chem.* **2017**, *56*, 8355.
[193] W. Cho, Y. J. Lim, S.-M. Lee, J. H. Kim, J. H. Song, J.-S. Yu, Y.-J. Kim, M.-S. Park, *ACS Appl. Mater. Interfaces* **2018**, *10*, 38915.
[194] Y. Jiang, Y. Bi, M. Liu, Z. Peng, L. Huai, P. Dong, J. Duan, Z. Chen, X. Li, D. Wang, Y. Zhang, *Electrochim. Acta* **2018**, *268*, 41.
[195] L.-j. Li, Z.-X. Wang, Q.-C. Liu, C. Ye, Z.-Y. Chen, L. Gong, *Electrochim. Acta* **2012**, *77*, 89.
[196] L.-j. Li, X.-h. Li, Z.-x. Wang, H.-j. Guo, P. Yue, W. Chen, L. Wu, *J. Alloys Compd.* **2010**, *507*, 172.
[197] M.-x. Dong, X.-q. Li, Z.-x. Wang, X.-h. Li, H.-j. Guo, Z.-j. Huang, *Trans. Nonferrous Met. Soc. China* **2017**, *27*, 1134.
[198] M. Zhang, H. Zhao, M. Tan, J. Liu, Y. Hu, S. Liu, X. Shu, H. Li, Q. Ran, J. Cai, X. Liu, *J. Alloys Compd.* **2019**, *774*, 82.
[199] Z. Zhang, D. Chen, C. Chang, *RSC Adv.* **2017**, *7*, 51721.
[200] P. K. Nayak, J. Grinblat, M. Levi, E. Levi, S. Kim, J. W. Choi, D. Aurbach, *Adv. Energy Mater.* **2016**, *6*, 1502398.
[201] B. Song, W. Li, S.-M. Oh, A. Manthiram, *ACS Appl. Mater. Interfaces* **2017**, *9*, 9718.
[202] J. Yang, M. Hou, S. Haller, Y. Wang, C. Wang, Y. Xia, *Electrochim. Acta* **2016**, *189*, 101.
[203] H. Zhang, J. Zhang, J. Ma, G. Xu, T. Dong, G. Cui, *Electrochem. Energy Rev.* **2019**, *2*, 128.
[204] S.-J. Tan, X.-X. Zeng, Q. Ma, X.-W. Wu, Y.-G. Guo, *Electrochem. Energy Rev.* **2018**, *1*, 113.
[205] M. Winter, *Z. Phys. Chem.* **2009**, *223*, 1395.
[206] J. Kasnatscheew, M. Evertz, R. Kloepsch, B. Streipert, R. Wagner, I. Cekic Laskovic, M. Winter, *Energy Technol.* **2017**, *5*, 1670.
[207] L. Downie, S. Hyatt, J. Dahn, *J. Electrochem. Soc.* **2016**, *163*, A35.
[208] A. M. Haregewoin, A. S. Wotango, B.-J. Hwang, *Energy Environ. Sci.* **2016**, *9*, 1955.
[209] J. Li, W. Li, Y. You, A. Manthiram, *Adv. Energy Mater.* **2018**, *8*, 1801957.
[210] S. S. Zhang, *J. Power Sources* **2006**, *162*, 1379.
[211] L. Ma, J. Self, M. Nie, S. Glazier, D. Y. Wang, Y.-S. Lin, J. Dahn, *J. Power Sources* **2015**, *299*, 130.
[212] D. Y. Wang, J. Xia, L. Ma, K. Nelson, J. Harlow, D. Xiong, L. Downie, R. Petibon, J. Burns, A. Xiao, *J. Electrochem. Soc.* **2014**, *161*, A1818.
[213] J. Li, H. Liu, J. Xia, A. R. Cameron, M. Nie, G. A. Botton, J. R. Dahn, *J. Electrochem. Soc.* **2017**, *164*, A655.
[214] K. Beltrop, S. Klein, R. Nölle, A. Wilken, J. J. Lee, T. K.-J. Köster, J. Reiter, L. Tao, C. Liang, M. Winter, *Chem. Mater.* **2018**, *30*, 2726.
[215] R. Petibon, J. Xia, L. Ma, M. K. Bauer, K. J. Nelson, J. Dahn, *J. Electrochem. Soc.* **2016**, *163*, A2571.
[216] L. Ma, S. Glazier, R. Petibon, J. Xia, J. M. Peters, Q. Liu, J. Allen, R. Doig, J. Dahn, *J. Electrochem. Soc.* **2017**, *164*, A5008.